Structured illumination microscopy: enhancement of resolution gain, reconstruction process and quantitative assessment of images

Dissertation

Zur Erlangung des Doktorgrades

der Naturwissenschaften

vorgelegt beim Fachbereich Biowissenschaften

der Johann Wolfgang Goethe-Universität

in Frankfurt am Main

von

Víctor Didier Pérez Meza

aus Mexiko

Frankfurt am Main, 2018

(D 30)

vom Fachbereich Biowissenschaften der

Johann Wolfgang Goethe-Universität als Dissertation angenommen.

Dekan: Prof. Dr. Sven Klimpel

Erster Gutachter: Prof. Dr. Ernst H. K. Stelzer

Zweiter Gutachter: Prof. Dr. Mike Heilemann

Datum der Disputation: _____

Acknowledgements

This PhD thesis is not only a culmination of 4 years of work but it also represents for me an apex in the last 13 years of my life in academy. Thus I feel the need to acknowledge the persons and institutions from which I have nourished intellectually and morally during these years. I start thanking my family, aunties, uncles and cousins for their constant support and companionship. Thanks to my parents Sandra and Armando for having entrusted me with so much freedom. Wisdom does come with age and so I thank my grandparents, Enriqueta (Boba), Faustino (Tata), Josefina (La Jechu) and Juan (Papa Juan) for sharing a wee bit of theirs with me. My most grateful acknowledgement and admiration is for Jechu and Papa Juan, who have always supported me and whose exemplary life of hard work is my source of motivation.

Thanks to my *alma mater*, la Universidad Nacional Autonoma de Mexico, for providing me with scientific knowledge and for teaching me that the recognition of one's ignorance is the first step to confront it. Thanks to Dr. Omar Saavedra for your willingness and promptness in providing support and guidance during my Bachelor thesis. Thanks to the Center of Regenerative Therapies in Dresden and Dr. Sophie Pautot for giving me the opportunity to get involved in the field of fluorescence microscopy. Thanks to the Technische Universität Dresden for being my first window to the world and serve as incubator of comradery between different cultures, thanks to this I had the chance to meet my life companion, Maryam Vahdatzadeh, who has taught me the meaning of taking things into one's own hands.

Thanks to the Goethe-Universität in Frankfurt am Main and Prof. Dr. Ernst Stelzer for hosting me during the last 4 years as a PhD student. Thanks to Prof. Dr. Stelzer for sharing his expertise and to the AK Stelzer members

for always been open to spontaneous discussions and questions. Thanks to Dr. Bo-Jui Chang for his fruitful discussions, guidance and inclusiveness, thank you Dr. Chang for introducing me to your project and gave me the freedom and support to develop it and make it mine as well.

Contents

List of figures

List of tables

Mathematical notation

$\vec{r} = (x, y, z)$	Spatial coordinates
$\overrightarrow{dr} = (dx, dy, dz)$	Differential of spatial coordinates
$\vec{k} = (k_x, k_y, k_z)$	Spatial frequencies in Fourier space
$\tilde{f}$	$\tilde{f}$ is the Fourier transform of function f
f^*	Conjugate of function f
PS(f)	Power spectrum of function f $= \|ff^*\|$
$\langle f(x,y) \rangle_r$	Circular average: Mean of function $f(x,y)$ along the perimeter with radius r; $r = \sqrt{x^2 + y^2}$
O_{mj}	Set of raw SIM images acquired with the illumination pattern at phase m and direction j
$*$	Convolution operator
T_o	Period of illumination pattern
p_o	Norm of spatial frequency of illumination pattern
p_o'	Estimate of p_o
$\vec{p}_{oj}$	Spatial frequency of illumination pattern in direction j

List of acronyms

Microscopy methods

csiLSFM: Coherent structured illumination light-sheet based fluorescence microscopy

DSLM: Digital scanned laser light-sheet microscopy

LLSFM: Lattice light-sheet fluorescence microscopy

LSFM: Light-sheet fluorescence microscopy

PALM: Photo-activated localization microscopy

SIM: Structured Illumination microscopy

STED: Stimulated emission depletion microscopy

STORM: Stochastic optical reconstruction microscopy

TIRF: Total internal reflection fluorescence microscopy

Image concepts

OF: Out-of-focus

OTF: Optical transfer function

IF: In-focus

FOV: Field of view

PSF: Point spread function

SNR: Signal-to-noise ratio

RL: Richardson-Lucy

WF: Wide field

Abstract

Structured illumination microscopy (SIM) is part of the super-resolution methods developed at the beginning of this century. To produce a super-resolution image SIM requires three things: 1) illumination of the sample with a periodic pattern, 2) acquisition of multiple images per plane under different pattern's phases and orientations and 3) the processing of these images has to be carried with a reconstruction algorithm. The result of the reconstruction is an image with a resolution gain that is proportional to the frequency of the pattern (p_o). The typical SIM set-up uses an epi-fluorescence configuration, thus the interference angle of the beams that create the pattern is restricted by the angular aperture of the objective. Under this restriction the maximum value of p_o is given by the cut-off frequency of the objective lens and sets at 2 the maximum resolution gain of SIM under linear illumination.

In the first part of this thesis we present the implementation and characterization of the 2D-SIM set-up designed by Dr. Bo-Jui Chang (B-J. Chang *et al.*, PNAS 2017), this design exploits the concept introduced by light-sheet microscopy, i.e. separation of illumination and detection paths to obtain resolution gains larger than the usual two-fold (Chapter 3). The set-up is named coherent structured illumination light-sheet based fluorescence microscopy (csiLSFM) and it consists of a triangular array of three objectives, such that two are used for illumination and one for detection. With the independent illumination arms is possible to interfere two coherent light-sheets at angles beyond the angular aperture of the detection lens, attaining the maximum interference angle of 180° when the light-sheets counter-propagate. This condition delivers a pattern with a p_o 1.4 times larger than the cut-off frequency (ω_o), hence our set-up provides generic resolution gains of 2.4.

The extraction of the high spatial frequencies that produce the resolution gain in the csiLSFM is a challenge due to a low pattern modulation. The low modulation inherently arises because the frequency associated to the pattern period lies beyond the cut-off frequency of the detection lens. To overcome this challenge we developed a filtering strategy that facilitates the withdrawal of information from a SIM data set, simultaneously the proposed filtering process optimizes the reconstruction algorithm by reducing the periodic artifacts that are recurrent in SIM images. In this same chapter we also performed an spectral analysis of the artifacts and determined that they originate from irregularities in the power spectrum that occur due to the partial or total lack of certain spatial frequencies (fig.4.2 and 4.3), our reconstruction reduces this information drops and diminishes the artifact occurrence. The relevance of our reconstruction pipeline is that it delivers a standardized process to enhance the SIM image in a current context in which the commonly used reconstruction algorithms employ empirical tuning to improve it (fig.4.13). Moreover, the pipeline is applicable to the csiLSFM data and also to images acquired with any other 2D-/3D-SIM set-up (fig.4.10 and 4.11).

The processing of various image data sets acquired with the csiLSFM exposed us to the question of how low the modulation of the illumination pattern can be before no super-resolution frequencies can be extracted. Answering this question is important to guarantee that the SIM data contains enough spatial frequencies to provide significant resolution gains. Thus in chapter 5 we developed a quantitative metric to indirectly determine the pattern modulation from the SIM data and find its critical value to use it as evaluation criterion. We called this metric the quality factor (Q-factor) and it represents the normalized strength (amplitude) of the extracted frequencies respect to the Gaussian noise contained in the images. Through simulations we estimated that $Q=0.11$ is a critical value and a SIM data set requires this as minimum value is to deliver a

significant resolution gain. Q works then as an assessment tool for classifying SIM data as optimal or sub-optimal, i.e. $Q{\geq}0.11$ or $Q{<}0.11$. We demonstrated such application with data acquired in various SIM commercial set-ups to prove its feasibility in the field (fig.5.6-5.11)

As mentioned at the beginning of this abstract SIM requires a specialized set-up and a processing algorithm to produce super-resolution images. This thesis contributes to these two areas in the following aspects: first, in its linear version a structured illumination microscope is highly associated to a 2-fold resolution gain. Here we demonstrated the possibility of extending this gain to 2.4 using our custom set-up the csiLSFM. Second, a reconstructed SIM image is prone to artifacts due to the mathematical process it undergoes, here we analyzed the artifact sources and identified them with drops of spatial information in the reconstructed spectrum, based on these conclusions we designed a processing pipeline to facilitate the extraction of spatial frequencies and directly reduce artifacts. A third and final outcome of this thesis is the development and practical implementation of a quantitative index to evaluate the quality of SIM data in terms of its relevant information content (Q-factor). Accordingly, the overall contributions of this work were done in the areas of SIM set-up, SIM reconstruction procedure and SIM data evaluation.

Zusammenfassung

Structured illumination microscopy (SIM) gehört zu den Höchauflösungs Fluoreszenzmikroskopie Methoden, welche Anfang dieses Jahrhunderts entwickelt wurden. Um ein hochaufgelöstes Bild mittels SIM zu erzeugen, sind folgende Punkte zu beachten: 1) die Beleuchtung der Probe erfolgt über ein periodisches Muster, 2) Pro Ebene werden jeweils mehrere Bilder entsprechend unterschiedlicher Phasen und Richtungen des Musters aufgenommen, 3) die Verarbeitung dieser Bilder erfolgt mit einem Rekonstruktionsalgorithmus. Das Resultat der Rekonstruktion ist ein Bild mit einem Auflösungsgewinn die proportional zur Frequenz des Musters (p_o) ist. SIM Geräte verwenden typischerweise eine Epifluoreszenzkonfiguration, so dass entsprechende Beleuchtungs- und Detektionspfade gekoppelt sind. Zudem werden Interferenzwinkel der Lichtstrahlen, die das Muster erzeugen, durch die Winkelöffnung des Objektivs begrenzt. Unter dieser Begrenzung liegt der Maximalwert von p_o in der Nähe der Grenzfrequenz des Objektivs. Aus diesem Grund liegt die Einstellung des maximalen Auflösungsgewinns von SIM auf 2 bei linearer Beleuchtung.

Im ersten Teil dieser Arbeit präsentieren wir die Umsetzung und Charakterisierung der 2D-SIM Konfiguration von Dr. Bo-Jui Chang (B-J. Chang et al., PNAS 2017). Dieses Design basiert auf dem Konzept der Lichtscheibenmikroskopie, d.h. der Trennung von Beleuchtungs- und Detektionspfaden, um einen Auflösungsgewinn größer als den üblichen, zweifachen Wert zu erhalten. Diese Konfiguration bezeichnen wir als coherent structured illumination lightsheet based fluorescence microscopy (csiLSFM). csiLSFM besteht aus einer dreieckigen Anordnung von drei ähnlichen Objektiven, von denen zwei für die Beleuchtung und eines für die Detektion verwendet werden. Um einen Auflösungsgewinn größer als

2 zu erzielen mischen sich jeweils zwei kohärenten Lichtscheiben ein, in Interferenzwinkeln jenseits der Winkelöffnung des Detektionsobjektivs. Der maximale Interferenzwinkel von 180° ist erreicht, wenn sich die Lichtscheiben gegenläufig ausbreiten. Diese Voraussetzung liefert ein Muster mit entsprechender Frequenz p_o, die 1,4 mal größer ist als die Grenzfrequenz (ω_o). Deshalb bietet der csiLSFM einen generischen Auflösungsgewinn von 2,4 (Gl.35). Kapitel 3 stellt den optischen Pfad des csiLSFM, die Aufbaukomponenten, die Ausrichtung und die theoretischen Berechnungen der zu erwartenden Auflösung und den maximalen Auflösungsgewinn vor. Das System kann auch folgendermaßencharakterisiert werden: Zunächst wurden Kalibrierkurven extrahiert, um die Bewegungsparameter der motorisierten Komponenten im Aufbau mit den Phasen und Perioden des Beleuchtungsmusters in Beziehung zu setzen (Abb.3.4 und 3.5). Zweitens wurde die experimentelle dreidimensionale Punktspreizfunktion (*PSF*) des Mikroskops sowohl für Weitfeld- als auch für SIM-Bilder erfasst. Die berechnete theoretische Auflösung wurde durch Vergleich mit den Abmessungen des *PSF*s validiert. Die beste laterale Auflösung des csiLSFM betrug 91 nm und wurde mit einem Objektiv mit einer Weitfeldauflösung von 301 nm erzielt (Tabelle 3.2). Die Möglichkeit, einen Auflösungsgewinn größer als zwei in biologischen Proben zu erhalten, wurde zudem an einigen biologischen Proben demonstriert (Abb.3.7 und 3.8).

Aufgrund der geringen Mustermodulation ist die Extraktion der hohen Ortsfrequenzen, welche den Auflösungsgewinn im csiLSFM erzeugen, herausfordernd. Eine geringe Modulation entsteht dadurch, dass die der Musterperiode zugeordnete Frequenz außerhalb der Grenzfrequenz der Detektionslinse liegt. Um diese Herausforderung zu bewältigen, haben wir eine Filterstrategie entwickelt, welche die Entnahme von Informationen aus einem SIM-Datensatz erleichtert. Gleichzeitig optimiert der

Zusammenfassung

vorgeschlagene Filterprozess den Rekonstruktionsalgorithmus durch Reduzierung periodischer Artefakte, die in SIM-Bildern wiederkehrend sind. In Kapitel 4 beschreiben wir den Arbeitsablauf der vorgeschlagenen Rekonstruktionspipeline und demonstrieren deren Umsetzung in Datensätzen, die mit dem csiLSFM und anderen kommerziellen Mikroskopen erfasst wurden (Abb.4.4-4.12). Kern unserer Rekonstruktionsmethode ist die Entfaltung der Rohbilder mittelss Richardson-Lucy-Algorithmus vor jedem Rekonstruktionsversuch. Diese Strategie liefert höhere-räumliche Informationen mit größeren Amplituden, so dass sie in Bezug auf das Hintergrundrauschen relevanter werden. Im gleichen Kapitel haben wir auch eine Spektralanalyse der periodischen SIM-Artefakte durchgeführt und festgestellt, dass sie von Unregelmäßigkeiten im Leistungsspektrum stammen, die aufgrund des teilweisen oder vollständigen Fehlens bestimmter räumlicher Frequenzen auftreten (Abb.4.2 und 4.3). Unsere Strategie der Dekonvolution vor der Rekonstruktion reduziert den Informationsrückgang und glättet das Spektrumsprofil, um das Auftreten von Artefakten zu verringern und zudem ein standardisiertes Rekonstruktionsverfahren zu liefern. Die Relevanz unseres Rekonstruktionsverfahrens liegt darin, dass es eine standardisierte Prozessierung zur Bildverbesserung bietet. Dies wird ermöglicht in dem die gängigen Rekonstruktionsalgorithmen eine empirische Abstimmung zur Verbesserung des Bildes verwenden (Abb.4.13). Unsere Methode erfordert keine Abstimmung an das letztlich hochaufgelöste Bild und kann direkt auf 2D- und 3D-SIM Datensätze angewendet werden, wir konnten zeigen, dass unsere Rekonstruktion eine ähnliche bis bessere Bildqualität erreicht hat, als vergleichbar Methoden, die in kommerziellen Mikroskope implementiert sind (Abb.4.10 und 4.11).

Die Verarbeitung verschiedener Datensätze, die mit dem csiLSFM aufgenommen wurden, führte uns zu der Frage, wie niedrig die Modulation (M) des Beleuchtungsmusters sein darf, bis keine hochauflösenden

Frequenzen mehr extrahiert werden können. Die Beantwortung dieser Frage ist wichtig, um sicherzustellen, dass die SIM-Daten genügend Ortsfrequenzen enthalten, um einen signifikanten Auflösungsgewinn zu erzielen. Gleichzeitig kann die Erkenntnis über einen optimalen Modulationswert als Parameter zur Beurteilung der Datenqualität dienen. Somit ist die Beantwortung dieser Frage nicht nur für csiLSFM-Bilder grundlegend, sondern auch für jeden Bildsatz, der mit einem SIM-Setup aufgenommen wird. In Kapitel 5 adressierten wir dieses Problem, indem wir die Mustermodulation (M) mit der in der Rekonstruktion angezeigten Auflösung mittels des Rayleigh-Kriteriums verknüpft haben. Dann haben wir durch eine simulierte 2D-SIM-Erfassung an einem virtuellen Sample gezeigt, dass ein minimaler Modulationswert von M=0,5 tatsächlich erforderlich ist, um einen vollen Auflösungsgewinn zu erreichen (Abb.5.1). Die Berechnung der Mustermodulation in realen Datensätzen ist nicht einfach, daher haben wir eine Metrik zur indirekten Schätzung der effektiven Modulation in einem SIM-Datensatz definiert. Wir nannten diese Metrik den Qualitätsfaktor (Q-Faktor) und sie repräsentiert die normierte Stärke der extrahierten Ortsfrequenzen bezüglich des Gaußschen Rauschens in den Bildern. Unsere Berechnungen und Simulationen führen zu zwei wichtigen Ergebnissen: a) Der Rekonstruktionsprozess verstärkt das Gaußsche Rauschen, genauer gesagt, die Rauschvarianz in den hochauflösenden Frequenzen ist viermal so hoch wie die der Standardfrequenzen (Weitfeld) (§5.1.2). b) Bei einer SIM-Erfassung, die auf einen maximalen Auflösungsgewinn von 2 ausgelegt ist, wird ein Wert von Q=0,33 aus dem SIM-Datensatz benötigt, um diesen Gewinn zu erreichen. Wenn wir dagegen einen Auflösungsgewinn von 1,5 als Maßstab für einen signifikanten Gewinn festlegen, ist ein Mindestwert von Q=0,11 erforderlich (Abb.5.3 und 5.4). Ergebnis (a) unterstreicht die Bedeutung der Aufnahme von SIM-Datensätzen mit einem hohen Signal-Rausch-Verhältnis (SNR), andernfalls wird letztlich die Rauschverstärkung in niedrigen SNR-Daten den Auflösungsgewinn und Qualität des

Zusammenfassung

rekonstruierten Bildes beeinträchtigen (Abb.5.5a und 5.8). Ergebnis (b) bot eine praktische Umsetzung, nämlich den Wert Q=0.11 als Schwellenwert für die Klassifizierung von SIM-Daten als optimal oder suboptimal, d.h. Daten mit Q≥.11 enthalten Frequenzen, die stark genug sind, um einen signifikanten Auflösungsgewinn zu liefern, während Daten mit Q<0.11 dies nicht tun. Experimentelle Bedingungen wie Laserleistung, Belichtungszeit und Musterperiode beeinflussen den Wert von Q, daher haben wir Q=0,11 als Richtlinie verwendet, um diese experimentellen Parameter einzustellen und optimale Qualitätsdaten zu erhalten. Diese Anwendung wird anhand von Daten demonstriert, die in verschiedenen kommerziellen SIM-Setups gesammelt wurden, um ihre Machbarkeit im Feld zu beweisen (Abb.5.6-5.11). Daher ist das Hauptergebnis von Kapitel 5 die Einführung von Q als quantitative Bewertungsmetrik, die eine Datenmanagement-Entscheidung in SIM unterstützt, wie z.B. eine Rekonstruktion weiter zu führen, eine Neuerfassung zu versuchen oder einfach die Speicherung/Löschung der Daten entsprechend ihrer Klassifizierung (optimal/suboptimal).

Wie bereits zu Beginn erwähnt, erfordert SIM spezielle Einstellungen und einen Verarbeitungsalgorithmus, um Bilder mit hoher Auflösung zu erzeugen. Diese Doktorarbeit trägt zu diesen beiden Voraussetzungen mit folgenden Aspekten bei: 1) In seiner linearen Version besitzt ein strukturiertes Beleuchtungsmikroskop einen 2-fache Auflösungsgewinn. Hier haben wir mit Hilfe unseres kundenspezifischen Mikroskops die Möglichkeit demonstriert, besagten Gewinn auf 2,4 zu erweitern was durch die Trennung der Beleuchtungs- und Detektionspfade erreicht wurde. 2) Ein rekonstruiertes SIM-Bild ist aufgrund des mathematischen Prozesses, den es durchläuft, anfällig für Artefakte. Hier analysierten wir die Ursachen der Artefakte und identifizierten sie als Rückgang räumlicher Informationen im rekonstruierten Spektrum. Basierend auf diesen Schlussfolgerungen etablierten wir eine Abfolge zur Bildverarbeitung , um

Artefakt-reduzierte Bilder liefern zu können. 3) Die Entwicklung und praktische Umsetzung eines quantitativen Index zur Bewertung der Qualität von SIM-Daten in Hinblick auf ihren relevanten Informationsgehalt (Q-factor) markiert den letzten Beitrag der Thesis. Die Gesamtbeiträge dieser Arbeit sind in den Bereichen SIM-Setup, SIM-Bildrekonstruktion und SIM-Datenauswertung angegliedert.

1 Introduction

1.1 Historical outline

Optical microscopy has reached an apex of development built largely on the advancements made during the second half of the 19th century and along the entire 20th century[1–13]. Building a custom microscope that can be adapted to the experimental needs and produce high quality images is possible thanks to the manufacturing of quasi aberration-free optics, production of faster and more sensitive photon detection devices and the ease of use delivered by the digital control of various microscope components. The current diversity of lenses, filters, light sources, fluorescent tags, cameras, motorized elements and sample mounting methods allow the flexible design of a microscope around a particular sample and experiment of interest rather than adapting a sample to the constraints of a rigid system.

The first microscopes built in the late 1600s by Robert Hooke and Antoni van Leeuwenhoek used candles and oil lamps to illuminate the sample[14,15], the light transmitted through the sample would then generate the contrast that formed the image of the magnified object. Although transmittance microscopy still works very well for observing heterogeneous or semi-transparent samples like tissues, it hardly generates sufficient detail to distinguish specific proteins or organelles in cells. The progress on the understanding of light-matter interactions, the invention of the laser and the discovery of fluorescent proteins and dyes lead to the development of new contrast mechanisms which involve linear and non-linear interactions between the illumination light and the sample. As response to the interaction the sample emits light, whose detection provides the contrast to form the image. Depending on the physical phenomena involved in the

interaction, the emitted light also provides structural and spatial information about the sample, for instance: fluorescence microscopy combined with fluorescent tagging facilitates the localization of very specific proteins and biomolecules within the cells[16], second harmonic generation provides information on the orientation of spatially ordered biomolecules like collagen fibers[17,18], Förster resonance energy transfer microscopy serves to infer (un)folding of proteins and fluorescence-lifetime microscopy can determine interactions between molecules[19,20]. These examples are part of the long list of microscopy methods at the current disposal of researchers but along with these a variety of illumination and detection modalities are also available. Their purpose is to improve image quality by reducing unwanted signals, such as background or out-of-focus light. The standard modality, the wide field, illuminates the whole sample volume and detects the light emitted within and out of the focal volume of the detection lens, therefore producing images with a notable blur. The reduction of out-of-focus light is done by modifications in either the illumination or detection paths as achieved by the total internal reflection[21], confocal[22] and light-sheet modalities[23–25], the three of them representing an improvement over the wide field mode in terms of image contrast and axial resolution.

When designing an imaging experiment with optical microscopy it is important to consider the compromise of three parameters: spatial resolution, temporal resolution (acquisition speed) and the photodamage that can be caused to the sample. Any microscopy method that dramatically improves one of these parameters without considerably worsening the other two is usually considered a step forward since a better compromise has been achieved. A large part of the research efforts in the last 20 years were focused on increasing the spatial resolution, to realize this it was necessary to develop methods that could circumvent the resolution limit established by Abbe in 1873[3]. The limit is inherent to the

wave nature of light and it establishes that the best achievable resolution for an optical microscope is about 200 nm. Around the beginning of the 21st century three main methods were developed to circumvent this limit and bring resolutions down to 20-100 nm, the family of methods is referred as super-resolution microscopy and is comprised by: stimulated emission depletion (STED)[26,27], structured illumination microscopy[28,29] (SIM) and stochastic optical reconstruction/photoactivated localization microscopy (STORM/PALM)[30–34]. The way these methods extract spatial information beyond the classical resolution limit is by modulating the intensity of the fluorescence emission across the field of view in either a controlled manner, like in STED and SIM, or stochastically, like in STORM/PALM. From a unifying standpoint the three methods represent different implementations of the same intensity modulation principle.

In this thesis we focus on SIM microscopy, a method that requires acquisition of multiple images per plane and a reconstruction algorithm to fuse them into a single image with a resolution gain of two[29,35]. We aimed at improving three aspects of the technique: extend its resolution gain, reduce artifact occurrence in the reconstructed images and develop a quantitative criterion to evaluate the quality of SIM images.

1.2   Scope and structure of this dissertation

This script reports the results of four research projects: 1) Coherent structured illumination light-sheet based fluorescence microscopy[36] (csiLSFM), 2) optimization of SIM reconstruction algorithm for periodic artifact reduction[37], 3) quantitative criteria for raw image quality in SIM (Q-factor) and lastly 4) the implementation of an autofocusing mode in a digital scanned laser light-sheet fluorescence microscope (DSLM). The first three projects are linked to each other and comprise the core of this thesis, their results are presented in chapters 3, 4 and 5 respectively. Previous work on the field of SIM and the theoretical background relevant

to this dissertation is presented in chapter 2. The discussion of the results is carried out in chapter 6. The results of the fourth project have been relegated to the appendix as they do not relate to the SIM topic.

The graphical summary of the thesis can be found in fig.1.1; to get acquainted with the four projects we shortly describe them in the following paragraphs:

1) Coherent structured illumination light sheet based fluorescence microscopy (csiLSFM): The resolution gain in a SIM set-up is inversely proportional to the period of the illumination pattern. The traditional implementation of SIM uses the epi-fluorescence configuration which couples the illumination and detection paths into a single objective, hence the smallest attainable pattern period is restricted by the numerical aperture of the objective. This restriction translates into a maximum resolution gain of 2[35]. In this project we assemble a microscope to produce lateral resolution gains larger than usual two-fold. Our microscope is assembled in a light sheet fashion, i.e. with independent illumination and detection paths. Two light sheets interfere to illuminate the sample with a 2D sinusoidal pattern. The interference angle, which determines the pattern period, is tunable and allows resolution gains from 2 to 2.4[36].

2) Optimized SIM algorithm to reduce artifacts: The general workflow of SIM is the acquisition of multiple raw images per plane followed by a reconstruction algorithm that fuses the spatial information of all the images into a single super-resolved image, the latter is prone to artifacts due to the mathematical processing it underwent. The standard way to reduce the artifacts is to dim them by empirically tuning the spectrum of the reconstructed image with an apodization function[29,38]. Opposite to this approach, we determined the sources of

the artifacts and filter them out by deconvolving the raw images. This strategy directly decreases artifact occurrence in the super-resolution image and provides a more standardized reconstruction procedure[37].

3) *Q*-factor: Every microscopy method has its limitations, SIM can occasionally underperform and deliver no resolution gain due to a low modulation of the illumination pattern[39]. The effective modulation is affected by the SNR, sample structure and pattern period. We defined a parameter to calculate the effective modulation and also estimated its range of values at which optimal raw image quality is achieved. Hence this parameter, referred as *Q*-factor, delivers a quantitative guideline to tune experimental parameters in order to achieve optimal image quality.

4) Autofocusing in the DSLM for multi-layer sample mounting: Mounting optically cleared samples for fluorescence imaging involves multiple layers of materials with different refractive indices[40,41]. This causes a defocusing aberration that grows as deeper planes of the sample are imaged because the focal plane of the detection lens shifts as function of the imaging depth. If the step-size of the focus shift is known it is possible to move the detection lens to compensate the aberration and directly re-focus at each plane of a 3D stack. We calculated this step as function of the experimental conditions, i.e. materials' refractive indices and numerical aperture of the lens, and used it to implement an auto-focusing modality in the DSLM system to obtain 3D images of cleared spheroids.
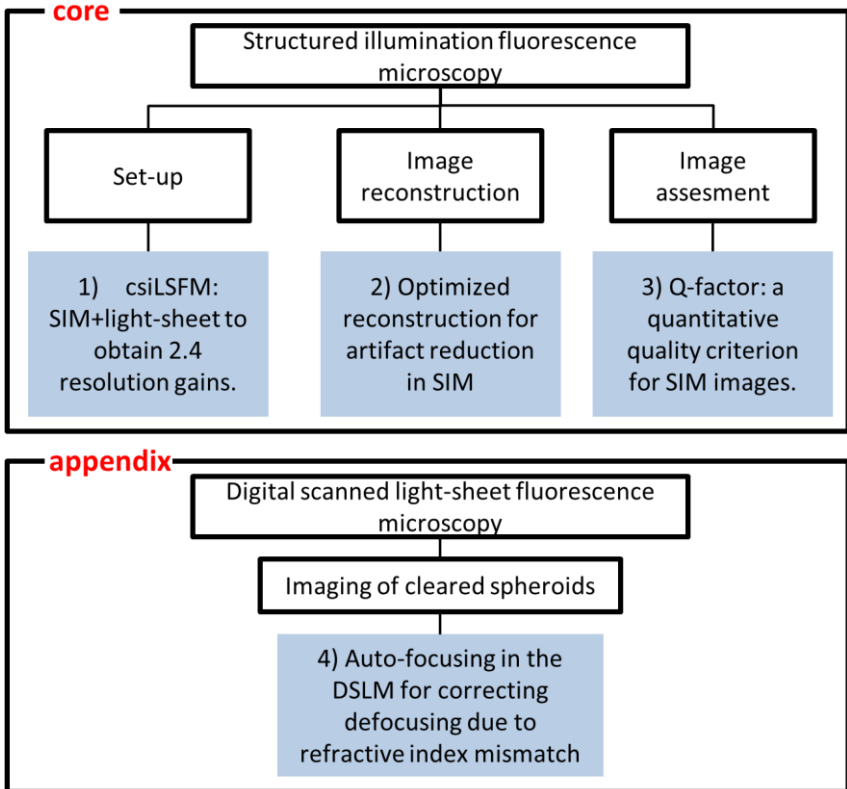
Fig.1.1 Graphic summary of the thesis. The main scope of the thesis is structured illumination microscopy. The method is built upon a set-up, a reconstruction algorithm and image quality assessment (white squares). The results presented in this thesis contribute in each of these research lines with three projects (blue squares): **1)** a new set-up configuration, **2)** a standardized image processing for artifact reduction and **3)** a quantitative image quality criterion. These three projects form the core of the script. **4)** The appendix presents a side project concerning the implementation of an auto-focusing mode for adequate imaging of cleared spheroids in the digital scanned laser light-sheet microscope (DSLM).

2 Background

2.1 Image formation in real space

The image in a microscope is formed when the light emitted by the sample propagates through the detection lens and reaches a photon detection device like a camera or a photomultiplier tube. As the light propagates from the sample its wavefront undergoes a spreading process formally known as diffraction. This phenomenon is the reason why a light emitting point will not be detected as such but rather as a blob. The blob is the correspondent image of a point and its intensity profile is called the point spread function (*PSF*). Mathematically a microscope is a device that maps, with its associated *PSF*, the object space (sample) into the image space (fig.2.1a); specifically, the image *O(x,y,z)* of a sample is formed by the convolution of the *PSF* with the spatial distribution of light emitters in the sample, *S(x',y',z')*, (eq.1).

$$O(x, y, z) = \int S(x', y', z') PSF(x' - x, y' - y, z' - z) \, dx' dy' dz' \tag{1}$$

If the integral notation is substituted by the convolution operator $*$, eq.1 is written as:

$$O(x, y, z) = S * PSF. \tag{2}$$

Due to the convolution operation, the image formation process in real space is interpreted as the blurring of the sample structures by the *PSF* (fig.2.1b/c/d).

2.2 The point spread function and spatial resolution

The dimensions of the *PSF* serve as estimation of the spatial resolution that a microscope can achieve. The *PSF* of each microscope has to be calculated by applying Maxwell's equations to the emitted light while considering all the optical elements that it encounters along its path. The simplest model, known as the Born & Wolf model[42], considers three elements: 1) a detection objective of numerical aperture NA and magnification *M*, 2) a sample emitting light of wavelength λ_{em} and 3) a medium of refractive index *n* between the sample and the front surface of the detection lens (fig.2.1a). Under these conditions and considering a paraxial approximation the intensity profile of the point spread function in the image plane (*z*=0) is equal to[43]:

$$PSF(x, y, 0) = \|E(x, y, 0)\|^2 \propto \left(\frac{J_1\left(\frac{2\pi NA}{M\lambda_{em}} \rho \right)}{\rho} \right)^2, \tag{3}$$

with $\rho = \sqrt{x^2 + y^2}$. The expression in eq.3 is known as Airy function, it consists of a central bright disk surrounded by multiple intensity-decaying rings (fig.2.1c). The integral under the disk accounts for 84% of the power[42], hence the disk dimensions represent an approximation of the *PSF* own lateral dimensions. The disk's radius ρ_o is used as criterion of the lateral spatial resolution (d_{xy}) and it is given by the argument of the first minimum of eq.3, thus[43]:

$$\rho_o = 0.61 \frac{\lambda_{em} M}{NA}. \tag{4}$$

The magnification factor M vanishes in the object space (fig.2.1c), therefore the actual lateral resolution of the microscope will be:

$$d_{xy} = 0.61 \frac{\lambda_{em}}{NA}.$$

(5)

The axial component of the PSF is[43]:

$$PSF(0,0,z) \propto \left(\frac{sin\left(\frac{\pi NA^2}{2nM^2\lambda_{em}} z \right)}{z} \right)^2 .$$

(6)

Using the same resolution criterion as done with the lateral component, the axial resolution of the microscope turns out to be:

$$d_z = 2 \frac{n\lambda_{em}}{NA^2}.$$

(7)

The functions in eq.3 and 6 are obtained by calculating the intensity of the emission's electromagnetic field, this is given in an integral expression in the Born & Wolf model[42]. To save time in the calculation of the integral and simplify the handling of the PSF, this is often approximated by a 3D Gaussian function[44] with its full width half maxima (FWHM) having the values of the lateral and axial resolutions (eq.8).

$$PSF(x,y,z) \propto= exp\left[-2.77\left(\frac{x^2}{d_{xy}^2} + \frac{x^2}{d_{xy}^2} + \frac{z^2}{d_z^2} \right) \right]$$

(8)
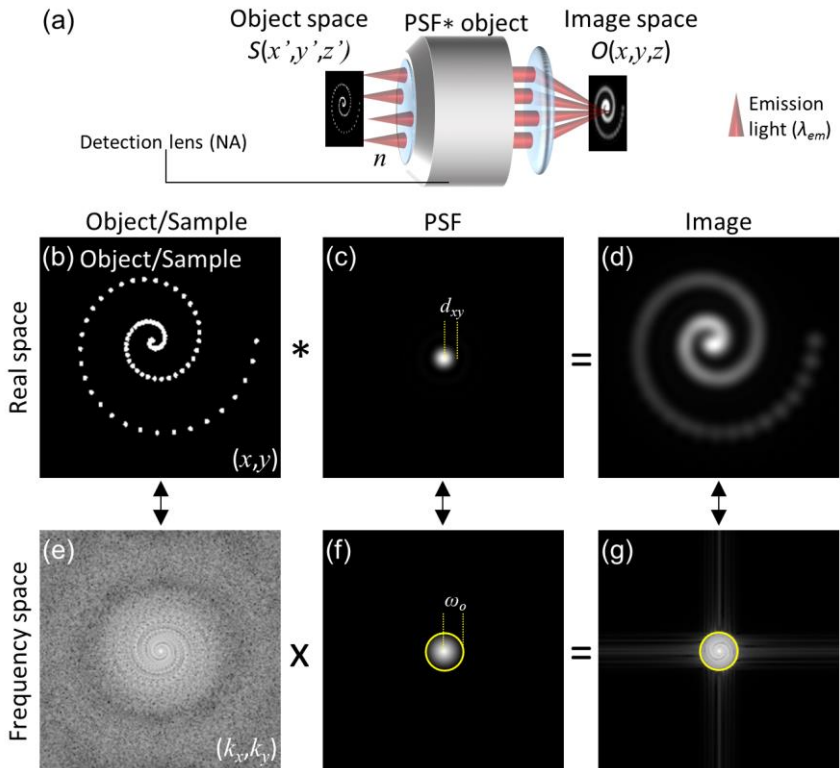
Fig.2.1 Image formation in real and frequency space. **(a)** Scheme of the elements involved in the imaging process. Sample, detection lens, emission light and immersion medium of refractive index n. The sample S lies in the object space (x', y', z') and the image O in the image space (x, y, z). **(b)** A dotted spiral used as sample to illustrate the image formation process. **(c)** Two dimensional *PSF* calculated from eq.3, using NA=1 and an emission wavelength of 600 nm. **(d)** The image of the spiral is formed by the convolution of the sample with the *PSF*. **(e)** The Fourier transform of the sample encodes it into spatial frequencies (k_x, k_y). **(f)** *OTF* with a cut-off frequency ω_o. **(g)** The Fourier transform of the image is the result of multiplying the Fourier transform of the object and the *OTF*.

2.3 Image formation in frequency space: optical transfer function

When applying the Fourier transform to eq.2 the convolution operation is transformed into a multiplication of the Fourier transforms of the object ($\tilde{S}$) and the *PSF* ($\widetilde{PSF}$):

$$\tilde{O}(k_x, k_y, k_z) = \tilde{S}(\vec{k})\widetilde{PSF}(\vec{k}) = \tilde{S}(\vec{k})OTF(\vec{k}) \tag{9}$$

The transform of the *PSF* is called the optical transfer function (*OTF*) and it provides a basis for another perspective of image formation, which we will illustrate in 2D with the lateral *PSF* given in eq. 3. The *OTF* of this function is a window that only permits the pass of certain frequency extent (fig.2.1f); since the sample structure is coded as frequencies in $\tilde{S}$ (fig.2e) an image is a frequency limited version ($\tilde{O}$) of the original object structure (fig.2.1g). The largest spatial frequency that the *OTF* is capable of transmitting is called the cut-off frequency (ω_o), its value holds a reciprocal relation with the spatial resolutions d_{xy} and d_z, thus in the case of the lateral resolution:

$$\omega_o = \frac{NA}{0.61\lambda_{em}}. \tag{10}$$

The cut-off frequency is directly proportional to the NA of the detection objective, under the *OTF* interpretation the higher the NA the more frequencies are captured and so a more detailed image of the sample is possible. An image is a limited resolution version of object; the limit is imposed by the light diffraction which is mathematically reflected in the finite size of the *PSF* (eq.5) or equivalently by the cut-off value ω_o in the frequency space. Understanding the image formation process in terms of

the *OTF* comes at hand in section 2.5 where the reconstruction algorithm of SIM is treated.

2.4   SIM overview and set-up configurations

SIM is a fluorescence microscopy super-resolution method developed by M. Gustafsson to obtain two-fold resolution gains respect to Abbe's limit[28,29]. The method illuminates the sample with a sinusoidal pattern created by the interference of two or three beams. The former implementation is referred as 2D-SIM and only provides lateral resolution gains, the latter is called 3D-SIM and it delivers both lateral and axial gains. The method introduced by Gustafsson was implemented in an epi-fluorescence configuration but it can be combined with other fluorescence microscopy techniques, such as TIRF or light-sheet, to add up benefits to the acquisition (fig.2.2).

Figs.2.2a/c show the standard set-up of 2D-and 3D-SIM respectively. In 2D-SIM two Gaussian beams (green) are focused on the back focal plane of the detection objective and interfere at the focal plane to create an intensity profile that presents a periodicity only on the *xy* plane (fig.2.2a top right). In 3D-SIM a third beam is occupied to introduce periodicity along the *z* direction (fig.2.2c plane *zy*). A rule of thumb in SIM is to expect resolution gains along the directions where the pattern presents periodicity, hence if isotropic lateral resolution gains are sought the pattern must be rotated around the *z*-axis during acquisition (fig.2.3a/b/c).

Figure 2.2b shows the combination of 2D-SIM with a total internal reflection fluorescence microscope (TIRF)[45], this set-up of course carries the advantages and drawbacks of both methods, such as images with lateral resolution gain and very high contrast but imaging depths limited to about 200 nm above the coverslip. Another very recent development, called lattice light-sheet fluorescence microscopy (LLSFM), implements 3D-SIM

in a light-sheet configuration (fig.2.2d). This is achieved by the interference of multiple Bessel beams that create a three dimensional pattern confined in a light-sheet of about 1 μm thick[46]. The light-sheet illumination dramatically reduces the photodamage[47] while the structured illumination provides the resolution gain. Though the gain is not isotropic because unlike epi-fluorescence SIM, pattern rotation is not possible in the LLSFM set-up, consequently the lateral resolution gain is obtained only along one direction (x-axis fig.2.2d).

The final resolution obtained with SIM depends on the NA of the detection objective therefore it is important to know that the choices for TIRF and LLSFM are constrained but not for the epi-fluorescence configuration. In TIRF high NAs are required for the total internal reflection to occur; hence NA $\geq$ 1.45 must be used[48]. In LLSFM the spatial constraints imposed by having two perpendicular objectives makes it only possible to have a NA=0.65 for illumination and NA=1.1 for detection. Typical attainable SIM resolutions for the different set-ups are summarized in table 2.1.

Resolution (nm)	2D-SIM		3D-SIM	
	Epi-fluorescence[28]	TIRF[45]	Epi-fluorescence[29]	LLSFM[46]
d_x	120	90	100	150
d_y	120	90	100	230
d_z	standard	~200	300	280

Table 2.1 Typical resolution measurements (nm) reported in different SIM set-ups.
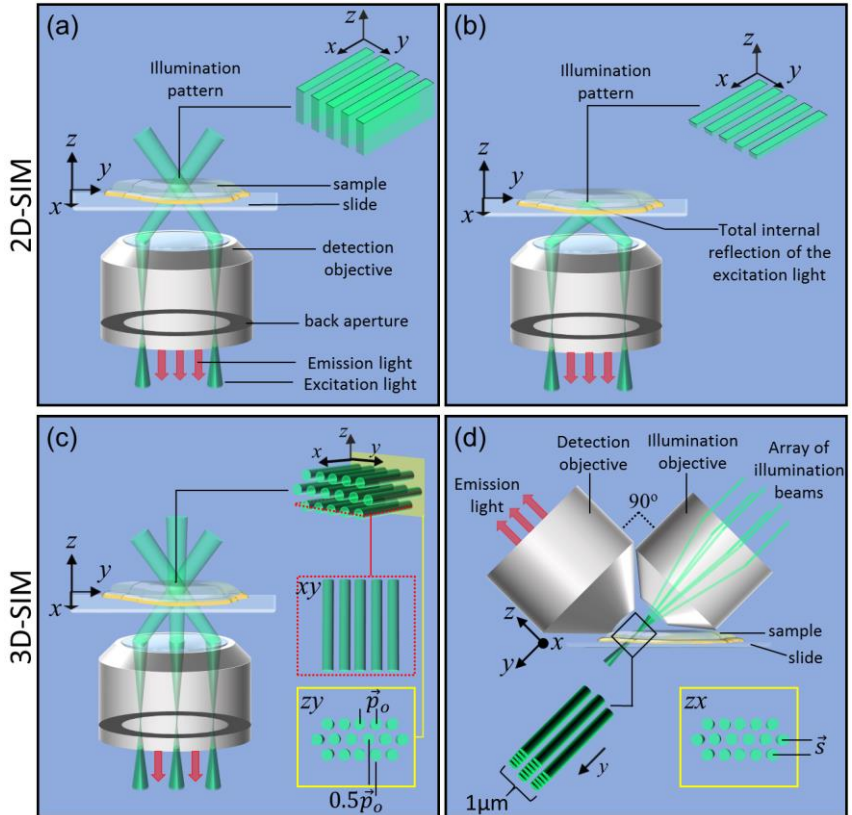
Fig.2.2 Set-up configurations for 2D- and 3D-SIM. **(a)** Epi-fluorescence and **(b)** total internal reflection fluorescence microscopy configurations for 2D-SIM. **(c)** Epi-fluorescence and **(d)** lattice light-sheet microscope for 3D-SIM. The latter configuration requires Bessel beams while the other three are implemented using Gaussian beams.

2.5   Extraction of frequencies beyond the resolution limit

SIM gains spatial resolution by extracting information beyond the cut-off frequency of the detection lens. To do so, it illuminates the sample with a periodic pattern casted by the interference of two or more beams. Let $I(\vec{r}')$ be the intensity profile of the illumination pattern in real space, according with eq.2 the image is:

$$O(\vec{r}) = (S(\vec{r}')I(\vec{r}')) * PSF(\vec{r}' - \vec{r}), \tag{11}$$

transforming this equation into the frequency space and applying the convolution theorem it becomes:

$$\tilde{O}(\vec{k}) = \left(\tilde{S}(\vec{k}) * \tilde{I}(\vec{k})\right) OTF(\vec{k}). \tag{12}$$

Since the illumination pattern is periodic $\tilde{I}$ is comprised by N discrete frequencies $\vec{p}_u$ that can be expressed as a linear combination of N delta functions. An image $\tilde{O}_m$ acquired with the pattern phase φ_m is:

$$\tilde{O}_m(\vec{k}) = \left(\tilde{S}(\vec{k}) * \sum_u^N c_u \exp(i\varphi_m)\,\delta(\vec{k} - \vec{p}_u)\right) OTF(\vec{k}), \tag{13}$$

with c_u denoting the multiplying constants and $u=1,2,...N$. Convolving the Dirac delta δ with the spectrum $\tilde{S}$ simply passes the argument of the former to the latter, consequently:

$$\tilde{O}_m(\vec{k}) = \left(\sum_u^N c_u e^{i\varphi_m}\tilde{S}(\vec{k} - \vec{p}_u)\right) OTF(\vec{k}). \tag{14}$$

The argument of $\tilde{\boldsymbol{S}}$ in the last equation is what accounts for the resolution gain in SIM. The sample spectrum has been shifted by the pattern frequencies $\vec{p}_u$, allowing high frequencies that were not available before to be carried into the extent of the *OTF*, thus providing information beyond the cut-off ω_o. The extraction of the high spatial frequencies requires acquisition of multiple images $\tilde{\boldsymbol{O}}_m$ at different φ_m phases, a single image does not provide enough information because the low and high frequencies are entangled in a single spectrum; this is readily seen in eq.15 where eq.14 has been expressed in matrix notation. The linear system in eq.15 has infinite solutions and so the spectra $\tilde{\boldsymbol{S}}(\vec{k} - \vec{p}_u)$ cannot be determined.

$$\tilde{\boldsymbol{O}}_m(\vec{k}) = (c_1 exp(i\varphi_m) \quad c_2 exp(i\varphi_m) \dots \quad c_N exp(i\varphi_m)) \begin{pmatrix} \tilde{\boldsymbol{S}}(\vec{k} - \vec{p}_1)OTF(\vec{k}) \\ \tilde{\boldsymbol{S}}(\vec{k} - \vec{p}_2)OTF(\vec{k}) \\ \vdots \\ \tilde{\boldsymbol{S}}(\vec{k} - \vec{p}_N)OTF(\vec{k}) \end{pmatrix} \quad (15)$$

To generate a *NxN* linear system that provides a unique solution it is standard procedure in SIM to acquire images with many phases φ_m as frequencies $\vec{p}_u$ of the illumination pattern. The *N* phases are chosen in regular steps taking as reference an initial phase φ_o:

$$\varphi_m = \varphi_o + \frac{2\pi m}{N}; \; m = 0,1,2, \dots (N-1). \quad (16)$$

We calculate now the system of eq.15 for the particular case of 2D-SIM (fig.2.3a). Two beams interfere with a half angle θ to create a 2D sinusoidal pattern that yields three frequencies:

$$\vec{p}_{u=1,2,3} = -\vec{p}_o, 0, \vec{p}_o. \quad (17)$$

$\vec{p}_o$ lies on the k_x-k_y plane hence it shifts the spectrum $\tilde{S}$ laterally. The norm of the vector $\vec{p}_o$ is the reciprocal of the pattern period T_o (fig.2.3c):

$$\|\vec{p}_o\| = p_o = \frac{1}{T_o} = \frac{2n\sin(\theta)}{\lambda_{ill}} \tag{18}$$

with λ_{ill} being the wavelength of the illumination beams. The multiplicative constants c_u are:

$$c_{u=1,2,3} = 0.5, 1, 0.5, \tag{19}$$

the 3x3 linear system of 2D-SIM is then:

$$\begin{pmatrix} \tilde{O}_o \\ \tilde{O}_1 \\ \tilde{O}_2 \end{pmatrix} = \begin{pmatrix} 0.5e^{i\varphi_o} & 1 & 0.5e^{-\varphi_o i} \\ 0.5e^{(\varphi_o + \frac{2}{3}\pi)i} & 1 & 0.5e^{-(\varphi_o + \frac{2}{3}\pi)i} \\ 0.5e^{i(\varphi_o + \frac{4}{3}\pi)} & 1 & 0.5e^{-i(\varphi_o + \frac{4}{3}\pi)} \end{pmatrix} \begin{pmatrix} \tilde{S}(\vec{k} - \vec{p}_o)OTF(\vec{k}) \\ \tilde{S}(\vec{k})OTF(\vec{k}) \\ \tilde{S}(\vec{k} + \vec{p}_o)OTF(\vec{k}) \end{pmatrix}. \tag{20}$$

The system's solutions provide three frequency domains $\tilde{S}(\vec{k})$, $\tilde{S}(\vec{k} - \vec{p}_o)$ and $\tilde{S}(\vec{k} + \vec{p}_o)$. The central domain $\tilde{S}(\vec{k})OTF(\vec{k})$ contains the standard resolution frequencies from which the limited resolution image can be extracted (fig.2.3f). The domains $\tilde{S}(\vec{k} - \vec{p}_o)OTF(\vec{k})$ and $\tilde{S}(\vec{k} + \vec{p}_o)OTF(\vec{k})$ contain the high spatial frequencies that convey the lateral resolution gain (fig.2.3d/e/g). In 3D-SIM three beams are interfered (fig.2.2c) and five frequencies are produced:

$$\vec{p}_{u=1,2,3,4,5} = -\vec{p}_o, -0.5\vec{p}_o, 0, 0.5\vec{p}_o, \vec{p}_o. \tag{21}$$

Thus, five pattern phases are required and the 5x5 linear system to solve is:

$$
\begin{pmatrix} \tilde{O}_o \\ \tilde{O}_1 \\ \tilde{O}_2 \\ \tilde{O}_3 \\ \tilde{O}_4 \end{pmatrix} = \begin{pmatrix} e^{2\varphi_o i} & e^{\varphi_o i} & 3 & e^{-\varphi_o i} & e^{-2\varphi_o i} \\ e^{(2\varphi_o + \frac{4\pi}{5})i} & e^{(\varphi_o + \frac{2\pi}{5})i} & 3 & e^{-(\varphi_o + \frac{2\pi}{5})i} & e^{-(2\varphi_o + \frac{4\pi}{5})i} \\ e^{(2\varphi_o + \frac{8}{5}\pi)i} & e^{(\varphi_o + \frac{4\pi}{5})i} & 3 & e^{-(\varphi_o + \frac{4\pi}{5})i} & e^{-(2\varphi_o + \frac{8}{5}\pi)i} \\ e^{(2\varphi_o + \frac{12}{5}\pi)i} & e^{(\varphi_o + \frac{6\pi}{5})i} & 3 & e^{-(\varphi_o + \frac{6\pi}{5})i} & e^{-(2\varphi_o + \frac{12}{5}\pi)i} \\ e^{(2\varphi_o + \frac{16}{5}\pi)i} & e^{(\varphi_o + \frac{8\pi}{5})i} & 3 & e^{-(\varphi_o + \frac{8\pi}{5})i} & e^{-(2\varphi_o + \frac{16}{5}\pi)i} \end{pmatrix} \dots
$$

$$
\dots \begin{pmatrix} \tilde{S}(\vec{k} - \vec{p}_o)OTF(\vec{k}) \\ \tilde{S}(\vec{k} - 0.5\vec{p}_o)[OTF(\vec{k} + \vec{s}) + OTF(\vec{k} - \vec{s})] \\ \tilde{S}(\vec{k})OTF(\vec{k}) \\ \tilde{S}(\vec{k} + 0.5\vec{p}_o)[OTF(\vec{k} + \vec{s}) + OTF(\vec{k} - \vec{s})] \\ \tilde{S}(\vec{k} + \vec{p}_o)OTF(\vec{k}) \end{pmatrix} \tag{22}
$$

The solution of this system provides a lateral and an axial resolution gain. The former is achieved through the lateral shift of $\tilde{S}$ carried by the vector $\vec{p}_o$. The latter is achieved by extending the axial extent of the *OTF* with the axial shift carried by the vector $\vec{s}$(fig.2.2c/d *zy* and *zx* views):

$$
\vec{s} = \frac{n}{\lambda_{ill}}(cos(\theta) - 1)\hat{z}. \tag{23}
$$

Once the different domains $\tilde{S}(\vec{k} - \vec{p}_u)$ have been extracted from eq.20 or eq.22 the information in them has to be properly fused to produce the super-resolution image. This fusing process is what is known as the reconstruction algorithm.
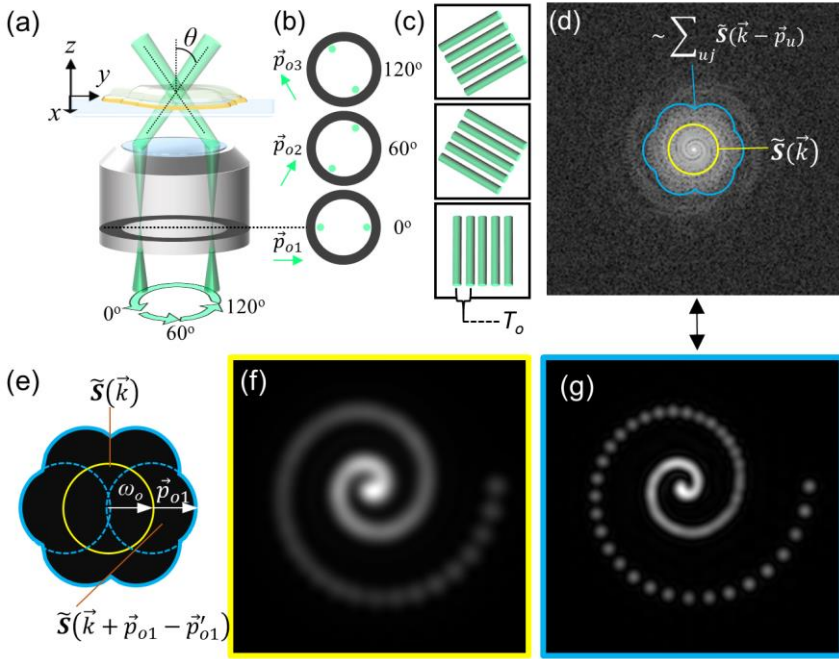
Fig.2.3 2D-SIM image acquisition and image formation. (a) Basic 2D-SIM set-up. Two beams interfere with a half angle θ and form a 2D sinusoidal pattern at the focal plane of the detection objective. The beams are rotated to acquire images in three different orientations 0°, 60° and 120°. (b) Transversal view of the beams focused on the back aperture of the detection objective. (c) xy projection of the interference pattern. The pattern has a period T_o. (d) Reconstructed spectrum obtained from simulating a 2D-SIM acquisition on the spiral from fig.2.1b. (e) The blue boundaries outline the domains $\tilde{\boldsymbol{S}}(\vec{k} - \vec{p}_{uj})OTF(\vec{k})$. The yellow one outlines the central domain $\tilde{\boldsymbol{S}}(\vec{k})OTF$ containing the limited resolution information from which the (f) wide field image can be extracted. The inverse Fourier transform of the reconstructed spectrum yields (g) the SIM super-resolution image.

2.6 Reconstruction of super-resolution images with SIM

The reconstruction algorithm of SIM is carried out by "stitching" all the domains $\tilde{\boldsymbol{S}}(\vec{k} - \vec{p}_u)OTF(\vec{k})$ into a single spectrum (fig.2.3d). The basic reconstruction steps are: 1) Shift back each domains to its native position, 2) sum all the domains and 3) apply the inverse Fourier transform to the sum to obtain the super-resolved image in real space $O_{SIM}(x,y,z)$. These three steps are summarized in one equation:

$$O_{SIM}(x, y, z) = \left\| \sum_u^N \exp(\vec{r} \cdot \vec{p}_u') \, FT^{-1} \{ \tilde{\boldsymbol{S}}(\vec{k} - \vec{p}_u)OTF(\vec{k}) \} \right\|, \tag{24}$$

each domain is transformed to real space by means of the inverse Fourier transform (FT^{-1}). The exponential factor shifts the domains back in the same direction and amount indicated by $\vec{p}_u'$, which is an experimental estimation of the actual frequency $\vec{p}_u$. This estimation is carried out by correlating the overlapping areas of the central domain and the extended ones (fig.2.3e)[29,37,38]. Although the exponential factor is applied in real space the shift does occur in Fourier space thanks to the frequency shift property of the Fourier transform. Finally, the sum along u fuses all the spatial information and its norm results in the super-resolution image.

In order to achieve isotropic resolution gain, SIM images have to be acquired with three pattern orientations, 0°, 60° and 120° (fig.2.3a/b/c), thus the linear systems in eqs.20 and 22 have to be solved for each of these orientations. To take the pattern orientation into account we additionally index the images $\tilde{\boldsymbol{O}}_m$ (eq.13) with j to indicate the orientation at which they were acquired($\tilde{\boldsymbol{O}}_{mj}$), this also has to be extended to the pattern's spatial frequencies, hence $\vec{p}_{uj}$. The domains $\tilde{\boldsymbol{S}}(\vec{k} - \vec{p}_{uj})OTF(\vec{k})$ from all

orientations have now to be summed to reconstruct $O_{SIM}(x,y,z)$, consequently eq.24 becomes:

$$O_{SIM}(x, y, z) = \left\| \sum_{j=1}^{3} \sum_{u=1}^{N} exp(\vec{r} \cdot \vec{p}'_{uj}) \, FT^{-1}\{\tilde{\boldsymbol{S}}(\vec{k} - \vec{p}_{uj})OTF(\vec{k})\} \right\|. \qquad (25)$$

Eq. 25 represents the basic reconstruction algorithm of SIM images, further processing steps can be added to denoise the image, emphasize high spatial frequencies and to remove artifacts. M. Gustafsson *et al*. introduced the first SIM reconstruction algorithm with an image enhancement processing, see eq.26. To emphasize high spatial frequencies each domain is deconvolved with a multi-image Wiener filter[29,49], an apodization mask $A(\vec{k})$ must be also used to smooth the domain's edges and avoid ringing artifacts. In this algorithms each domain is independently filtered, apodized, converted to real space, shifted back and then summed with the others.

$$O_{SIM}(x, y, z) = \left\| \sum_{j=1}^{3} \sum_{u=1}^{N} exp(\vec{r} \cdot \vec{p}'_{uj}) \, FT^{-1}\left\{ \frac{\tilde{\boldsymbol{S}}(\vec{k} - \vec{p}_{uj})OTF(\vec{k})}{\sum_{ju}\|OTF(\vec{k})\|^2 + w^2} A(\vec{k}) \right\} \right\|, \qquad (26)$$

A second method, shown in eq.27, was introduced by K. Wicker *et al*[38,50]; in it all the domains are processed together, i.e. all domains are first shifted back directly in Fourier space then summed and finally jointly processed with a Wiener filter and an apodization function. An extended point spread function is created by the OTFs. The method is designed to reconstruct 2D- or 3D-SIM stacks in a slice-by-slice manner, therefore an attenuation function g has to be introduced to lessen the out-of-focus signals, thus g is shaped as an inverted Gaussian function with full width half maximum d and attenuation power a, such that $a<1$ (eq.28).

$$O_{SIM}(x,y,z) = \left\| FT^{-1} \left\{ \frac{\sum_{j,u} \tilde{\mathbf{S}}(\vec{k} - \vec{p}_{uj} + \vec{p}'_{uj}) g(\vec{k} + \vec{p}'_{uj}) OTF(\vec{k} + \vec{p}'_{uj})}{\sum_{j,u} \left(g(\vec{k} + \vec{p}'_{uj}) \| OTF(\vec{k} + \vec{p}'_{uj}) \|^2 \right) + w^2} A(\vec{k}) \right\} \right\| \qquad (27)$$

$$g(k_r) = 1 - a \, exp\left(-2.77 \frac{k_r^2}{d^2} \right); k_r^2 = k_x^2 + k_y^2 \qquad (28)$$

The strategy to improve the reconstruction O_{SIM} with either eq.26 or 27, is the empirical tuning of the apodization function shape and the parameters w, a, d. Artifacts, which are a common issue in SIM images, are also reduced with this parameter tuning strategy.

2.7   Resolution gain in SIM

The theoretical resolution gain (rg) is calculated by the ratio between the highest frequency available in the spectrum of the SIM reconstruction (O_{SIM}), being that ($\omega_o + p_o$), and the cut-off frequency of the OTF (ω_o) (fig.2.3e):

$$rg = \frac{\omega_o^{final} + p_o}{\omega_o^{reference}}, \qquad (29)$$

Using eq.18:

$$rg = \frac{\omega_o^{reference}}{\omega_o^{final}} + \frac{\lambda_{em}}{\lambda_{ill}} \frac{\omega_o^{reference}(2nsin(\theta))}{NA} \qquad (30)$$

The cut-off frequency ω_o has been indexed with *final* and *reference* to emphasize that the resolution gain depends on the initial image that is take as reference and on the final processing that has been done to the image,

for instance a deconvolution. There are three possible ways to estimate ω_o, we introduced the first one in eq. 5 and 10, this is called the Rayleigh resolution criterion. There is also Abbe's criterion to estimate resolution of the wide field image (eq.31) and we can use the resolution of a confocal microscope to estimate the resolution attained after deconvolution (eq.32)[3,51].

$$d_{xy} = 0.5 \frac{\lambda_{em}}{NA} \rightarrow \omega_o = \frac{NA}{0.5\lambda_{em}} \tag{31}$$

$$d_{xy} = 0.4 \frac{\lambda_{em}}{NA} \rightarrow \omega_o = \frac{NA}{0.4\lambda_{em}}. \tag{32}$$

The generic way to state the theoretical resolution gain in a SIM set-up is by using Abbe's criterion in both numerator and denominator of eq.29. To maximize the resolution gain the half interference angle θ is equal to the angular aperture of the detection objective, i.e. $\theta=\sin^{-1}(NA/n)$. If we consider an average Stokes shift of 6% between the illumination and detection wavelengths[52] the resolution gain is:

$$rg = 1 + \frac{\lambda_{em}}{\lambda_{ill}} \frac{0.5(2n\sin(\theta))}{NA} = 1 + 1.06 \sim 2. \tag{33}$$

Eq.33 is why the standard resolution gain in SIM is considered as two-fold, but to correctly estimate the effective resolution gain is necessary to use eq.30 with the adequate cut-off frequencies. For example, it is worth mentioning that Rayleigh's criterion is more in accordance than Abbe's with the achievable resolution of a wide field microscope; if the former criterion is used as reference and a deconvolution has been used during the

reconstruction process, like in eqs.26 or 27, it would be more adequate to state that:

$$rg = \frac{0.61}{0.4} + \frac{\lambda_{em}}{\lambda_{ill}} \frac{0.61(2nsin(\theta))}{NA} \sim 2.8. \tag{34}$$

The resolution gain in SIM is a relative measurement that as established in eq.33 is used as a general approximation, yet if the actual resolution gain is to be accurately estimated then eq.30 should be used.

2.8   Image artifacts

SIM images are prone to artifacts due to its mathematical reconstruction, these artifacts are recurrent in both commercial and custom set-ups and it is not uncommon for scientist working with SIM to encounter them (fig.2.4). Despite this, the literature that only focuses on the origins of SIM artifacts is very recent and limited[37,39,53]. The handling of artifacts was always approached as the reconstruction algorithm being a black box in which the common strategy to improve image quality and artifact reduction was through the empirical tuning of the parameters in eq.26 and 27. Until very recently the role of experimental conditions such as microscope calibration, dye brightness, spherical aberrations, intensity drops and pattern modulation were studied as source of artifacts and underperformance of SIM systems. Practical guidelines have been designed to identify flaws in these conditions and allow correction strategies to improve the reconstruction[39]. Although useful, these guidelines have no quantitative quality criterion that would allow a more objective and immediate decision on how to proceed with raw data. The projects presented in chapter 4 and 5 contribute to the recent studies of SIM image evaluation by: 1) adding understanding of artifact sources[37] and 2) developing a quantitative quality criterion to identify sub-optimal raw data quality. For now, the goal of this section is to make the reader aware

of the existence of artifacts in SIM, though no standard classification is available, the appearance of them is usually described as periodic , side-lobes, honeycomb or hammer-stroke patterns. Figure 2.4 shows extracts from published literature in which these artifacts have been documented.
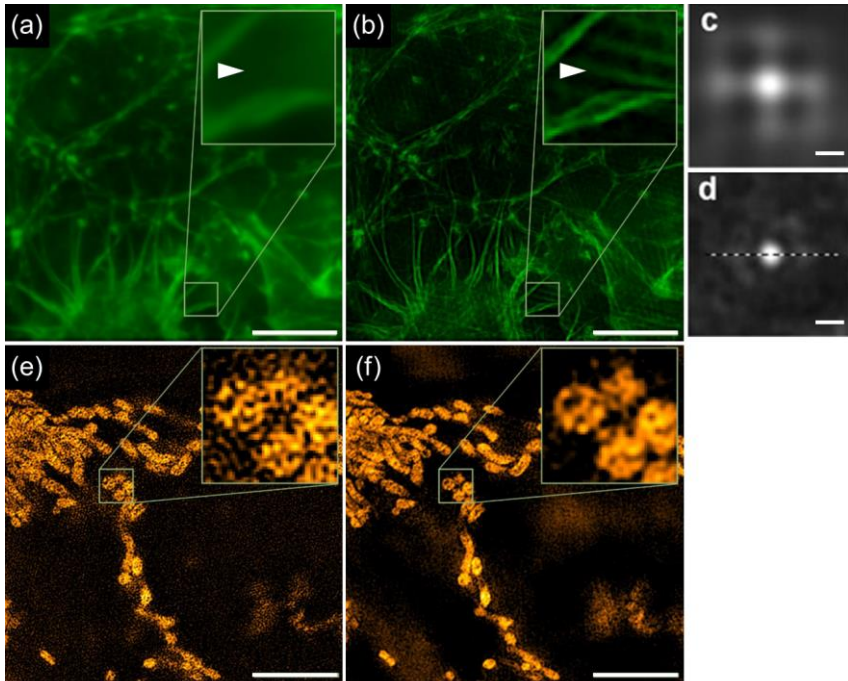
Fig.2.4 Types of artifacts in SIM reconstructions. (**a**) Wide field and (**b**) SIM reconstruction of actin filaments[50]. The reconstruction contains periodic artifacts arising from background fluorescence (white arrows). (**c**) Non-optimized SIM reconstruction of a 50 nm diameter bead presenting lobe-like artifacts. (**d**) Optimized reconstruction of the same bead[45]. (**e**) Non-optimized SIM reconstruction of mitochondria presenting grainy artifacts arising from raw data with low SNR. (**f**) Optimized reconstruction of the same sample[50]. Scale bar: 5 μm. (c-d) 100 nm.

3 Coherent structured illumination light-sheet based fluorescence microscopy (csiLSFM). Lateral resolution gains larger than two in linear SIM.

3.1 Theory

3.1.1 Three objectives configuration in SIM for large resolution gains

Two-fold is the standard resolution gain in linear SIM (eq.33). The limit for larger resolution gains comes in principle from the restricted interference angle of the epi-fluorescence configuration (fig.2.3). If this restriction is overcome larger interference angles would be possible and thus smaller illumination pattern periods would be achieved. Smaller periods mean larger gains since the shift of the image spectrum is also larger (eq.29). To extend the angle θ beyond the angular aperture of the detection objective it is necessary to separate the illumination and detection paths, to do so we proposed a set-up in which two objectives are used for illumination and one for detection (fig.3.1). The output of the illumination objectives is two interfering coherent light-sheets, whose angle of interference can be controlled by moving the position at which each of them enters the back aperture of its corresponding illumination objective (fig.3.1c planes x_1y_1 and x_2y_2). By separating the illumination and detection paths the angle θ can be tuned to be larger than the angular aperture of the detection objective, i.e. $\theta \geq \sin^{-1}(\mathrm{NA}/n)$.

The proposed configuration requires that the focus of the three objectives are co-localized so the light-sheets always pass through the focus of the detection objective independently of their interference angle (2θ). This imposes spatial constraints and reduces the microscope implementation to a certain set of objectives. Such set must have the right dimensions to fit in an arrangement with their foci co-localized and still have a high NA to provide a large range of angular motion to the light-sheets. The set of objectives that fulfill these conditions is a configuration of three Plan-Apochromat water immersion objectives (63X/NA=1.0 Zeiss) with a separation of 130° between the illumination objectives and 115° between each illumination and the detection objective[36](fig.3.1a). We called this set-up the coherent structured illumination light-sheet-based fluorescence microscope (csiLSFM).
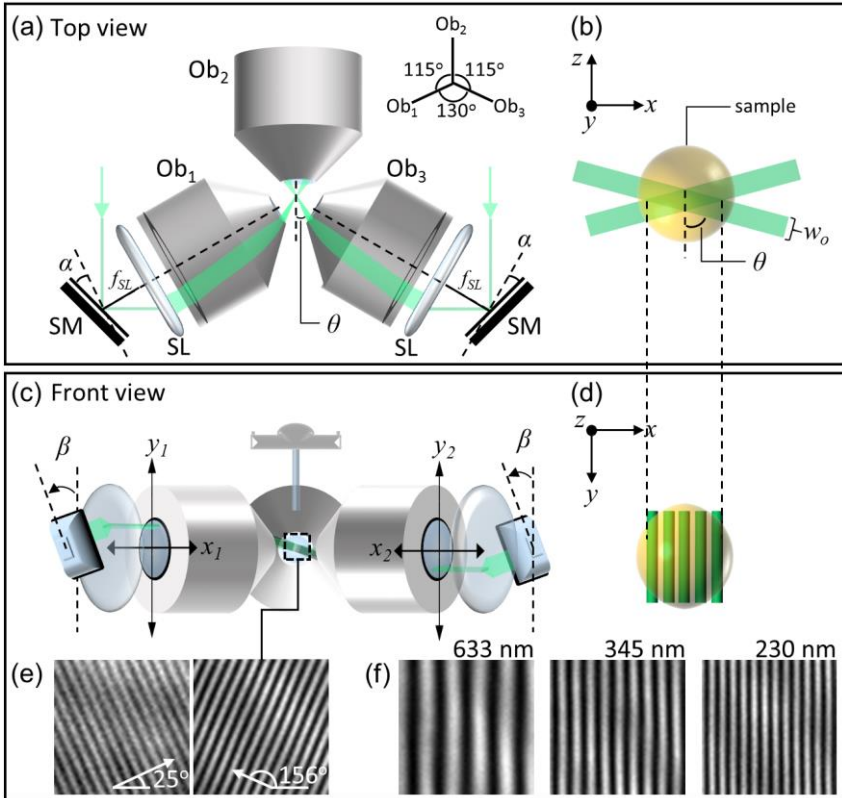
Fig.3.1 Light-sheet+SIM with a three objective configuration. (a) Top view of the csiLSFM. The core of the set-up consists of one illumination objective (Ob$_2$) and two illumination objectives (Ob$_1$, Ob$_3$) used to interfere two light-sheets at an angle 2θ. The angle α of the scanning mirrors (SM) determines this interference angle. (b) Top view of the sample being illuminated by the two light-sheets of thickness w_o. (c) Front view of the csiLSFM, the angle β of the scanning mirrors determines the rotation angle of the light-sheets, hence determining the orientation of the illumination pattern. The angles α and β control the entry points ($x_{1,2}, y_{1,2}$) at the back aperture of Ob$_1$ and Ob$_3$. (d) xy projection of the pattern illuminating the sample. (e) 25° and 156° orientations of the illumination pattern. (f) Three different pattern periods: 633 , 345 and 230 nm.

3.1.2 Generic and effective resolution gains in the csiLSFM

The maximum resolution gain that the csiLFM could achieve occurs when $\theta=90°$, i.e. when the illumination light-sheets counter-propagate. The generic lateral resolution gain under the proposed experimental conditions is 2.4 according to eq.33:

$$rg = 1 + \frac{\lambda_{em}}{\lambda_{ill}}\frac{n}{NA} = 1 + (1.06)\frac{1.333}{1} \sim 2.4. \tag{35}$$

The effective resolution gain should be according to eq.34:

$$rg = \frac{0.61}{0.4} + \frac{\lambda_{em}}{\lambda_{ill}}\frac{0.61(2n)}{NA} = 1.38 + 1.06\frac{1.6}{1} \sim 3.2. \tag{36}$$

Now, let us calculate the maximum lateral resolution in the csiLSFM considering an excitation wavelength of 488 nm and emission of 520 nm. The interference pattern of the counter-propagating light-sheets has a period of T_o=183 nm (eq.18); the radius of the *OTF*, accounting for a deconvolution, is ω_o=0.0049 nm^{-1} (eq.32). Hence, the maximum expected resolution of the system should be:

$$d_{xy} = \frac{1}{\omega_o + \frac{1}{T_o}} = \frac{1}{0.0049 + \frac{1}{183}}nm = 97 \text{ nm} \tag{37}$$

3.2 Control of the pattern's period, phases and orientation in the csiLSFM

The control of the pattern's period and orientation is carried out by the two-axis scanning mirrors set before the illumination objectives. The mirrors provide tilting angles about two perpendicular axis parallel to the back aperture planes x_1y_1 and x_2y_2 (fig.3.1c). The angle α refers to a tilt

respect to the $x_{1,2}$ and β respect to $y_{1,2}$ (fig.3.1a/b). The neutral position of the mirrors, i.e. α=0 and β=0 , is when their surfaces are parallel to the $x_{1,2}y_{1,2}$ planes.

The pattern's phases are controlled by the precise motion of a single-axis mount that moves the wavefront of one of the light-sheets along its propagation direction (fig.3.2).

3.2.1   Control of the pattern period
The period of the illumination pattern is determined by the interference angle 2θ of the light-sheets. This angle is controlled solely by the angle α, which along with the scanning mirror define the $x_{1,2}$ coordinate at which the light-sheets enter the back aperture. The angular aperture (AA) of the objective is $\sin^{-1}(1/1.333)$=48.6°, hence the range of interference angles available is $33°\geq2\theta\leq180°$, which correspond to periods of 645 and 183 nm respectively. When α=0 the intersection angle is 130° as this is the angle between the two illumination objectives. Fig. 3.1f illustrates the tunability of the pattern period in our microscope.

3.2.2   Control of the pattern orientation
The pattern orientation is solely controlled by the angle β (fig.3.1c), which along with the scanning mirror define the $y_{1,2}$ coordinate at which the light-sheets enter the back aperture, notice that to keep the pattern period constant in each orientation is necessary that $y_1=-y_2$.

A value of β=0 defines the 0° orientation of the pattern (fig.3.1f), orientations of 60° and 120° are not possible in the csiLSFM because the maximum β is defined by the AA of the objective. Hence the other two orientations are 48.6° and 130°. These orientations are maxima and decrease as the angle α moves away from its 0 position because the light-sheet is carried closer to the rim of the back aperture, for instance

when the light-sheets are counter-propagating, the pattern orientations are approximately 35° and 145°[36].

3.2.3   Control of the pattern phase

Fig.3.2a shows an optical fiber collimator mounted on a piezo nano-positioner (NP).   The NP realizes the linear translation of the collimator to shift the wavefront of one of the light-sheets to create a phase difference respect to the other one. To achieve the $2\pi/3$ phase steps of the illumination pattern (eq.16) the NP translates the collimator in steps of one third of the illumination wavelength ($\lambda_{ill}/3$).

3.3   Set-up

3.3.1   Mounting of illumination and detection objectives

A sketch of the set-up components and the actual set-up can be found in fig.3.2a and fig.3.2c respectively.   Fig.3.2b contains a list with the components' acronyms. The central piece of the set-up, i.e. the three objective configuration, can be seen in fig.3.2d, the objectives are partially inserted into a chamber containing the immersion medium[36].   All objectives share the same specifications: water immersion W Plan-Apochromat, working distance of 2.1 mm and 63X/NA1.0 (421480-9900-000, Zeiss).   To allow controlled positioning of the objectives, each of them is mounted on an *xy* translation mount that is attached to an optical ray that permits sliding the objective back and forth along its long axis, hence providing three degrees of freedom to each objective.

3.3.2   Illumination path

The illumination path consists of two arms comprised of the same components.   The path starts with the a laser source of 488 nm wavelengths (35 LTL 835, Melles Grio) and terminates in the illumination objectives (O_1,O_3) (fig.3a).   A beam splitter (BS) divides the wavefront

into two coherent beams. Each beam is coupled into a polarization-preserving single-mode optical fiber (OF, kineFLEX, Qioptiq). The collimators (FC, F220FC-543,Thorlabs) at the end of the fibers deliver the collimated beams which are then shaped into a light-sheet by a cylindrical lens (CL, f=75 mm, F69-699, Edmund Optics). The achromatic lens (L, f=200 mm, G322327322, Qioptiq) and the f-theta scanning lens (f=60.5 mm, S4LFT0061, Sill optics) form a 4f-telecentric system that projects the light-sheet into the back focal plane of the illumination objective. With this set of lenses the width (w_o) of the light-sheet was ~3µm (fig.3.1b/fig.3.3a).

Control of the light-sheet pattern period and rotation is done with the angular displacement α and β of the scanning mirrors (SM, S-334.2SL, Physik Instrumente) (fig.3.1a/c). The SM are mounted on a single axis motorized stage (M-232.17 Physik Instrumente) that provides a more flexible alignment of the light-sheets if needed. The pattern phase is controlled with the linear displacement of the fiber collimator carried out by the piezo nano-positioner (NP, P-725.4CD, Physik Instrumente).

3.3.3 Detection path

The detection path begins with the detection objective O_2, since we mostly used the 488 nm laser to excite our samples we set an emission filter for green dyes (EF, FF02-525/50-25, Semrock) after the objective. A 1X tube lens (TL, 452960, Zeiss) focuses the emission light into the camera to form the image. We used a CMOS camera with a pixel array of 1920x1440 and a pixel pitch of 3.63 µm (CC, C11440, ORCA-Flash 2.8, Hamamatsu).

3.3.4 Sample mounting

The three objectives are partially inserted into a customized sealed polyoxymethylene chamber with an open top for the sample entry (fig.3.2d), the chamber is filled with an appropriate medium, e.g. phosphate buffered saline (PBS), for biological specimens.

The sample is mounted in a 3D environment by embedding it inside a column of 1.5% phytagel or low-melt agarose (fig.3.2f green arrow) protruding from the glass capillary (fig.3.2f blue arrow). The capillary is fixed into a metallic holder (fig.3.2f/e yellow arrow) that is then attached to the 4-axis motorized stage (custom-designed, SmarAct) (fig.3.2e). The stage provides *xyz* translation of the sample and its rotation around the holder long axis. Alternatively to the 3D embedding a classic 2D coverslip culture can be mounted for imaging. This is achieved by gluing the coverslip onto a rod-like attachment of the metallic holder (fig.3.2g white arrow).

Embedding a sample into the agarose/phytagel column requires an aliquot of gel to be melted and then kept in a shaker at a constant temperature of about 37°, the gel and the sample are mixed for 5 minutes. After mixing, some gel is sucked into the glass capillary with a plunger (fig.3.2f red arrow). The capillary is kept in the fridge for some seconds so the gel becomes stiffer. Finally the plunger is pushed a few millimeters to partially expose the gel column to the immersion medium. In the case of 2D cultures we firstly cut the coverslip into small rectangular pieces and then apply the standard cell culture protocols using those pieces. After fixation and immunostaining of the cells a coverslip piece can be selected and glued with nail polisher as shown in fig.3.2g.
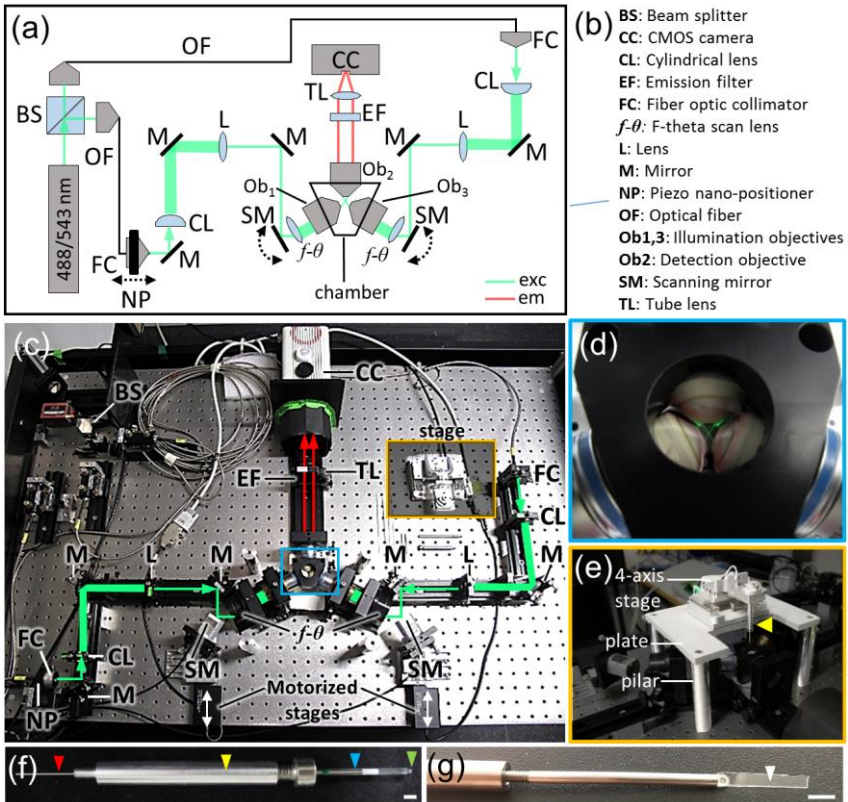
Fig.3.2 csiLSFM set-up. **(a)** Arrangement of the optical elements in the csiLSFM. **(b)** List of the csiLSFM components. **(c)** Actual set-up assembled on the optical breadboard. The sample stage and the chamber containing the three objectives are outlined by the orange and blue squares respectively. (d) Magnification of the three objectives inside the chamber. **(e)** Mounted stage, its 4-axis allow three dimensional motion and rotation of the sample. The yellow arrow indicates the sample holder; a magnification of this element is shown in **(f).** For a 3D sample mounting, the metallic holder contains a cylindrical glass capillary (blue arrow) filled with an agarose column (green arrow) in which the sample has been embedded. The agarose column is sucked by the capillary plunger (red arrow). **(g)** For 2D mounting a coverslip (white arrow) is glued to a rod-like adapter fixed to the main holder (yellow arrow). Scale bar: 4 mm.

3.4 Alignment and calibration of the csiLSFM

3.4.1 Light-sheets alignment

The csiLSFM is aligned when the foci of the three objectives are co-localized. When this occurs, the light-sheets pass through the focus of the detection objective for any angle α and β of the scanning mirrors. Accordingly, we implemented this principle as guideline to align the light-sheets. Any pattern with $\theta < 48.6$ can be visualized by the camera, and used as reference for alignment. We visualized the pattern with the 488 nm laser by substituting the emission filter (EF,fig3.2a) with a longpass colored glass filter (Schott glass GG495). Fig.3.3a shows the light-sheets of each illumination arm and its interference.

To commence with the alignment the rotation angle β is set to $0°$, then the illumination objective of arm 1 (O_1) is moved back/forth to set the light-sheet in the center of the field of view (FOV), bordered by the yellow lines in fig3.3. β is changed to apply a rotation, if the light-sheet passes through the focus of the detection objective (O_2) it should remain roughly within the FOV center, if not, it shifts its position and O_2 should be moved back/forth to re-center the light-sheet, once this is done β is set back to $0°$. This process is iteratively carried out until the light-sheet remains centered for the $0°$ and the other orientations (fig.3.3a arm 1). Fine tune can be done by moving O_1 in directions $x_1 y_1$ with help of the translational mount. After alignment the positions of O_1 and O_2 are fixed. To align the second arm the only degrees of freedom left are those of the second illumination objective (O_3). This element should be translated parallel to the $x_2 y_2$ plane and back/forth in an iterative manner to maintain the second light-sheet centered at any orientation (fig.3.3a arm 2).
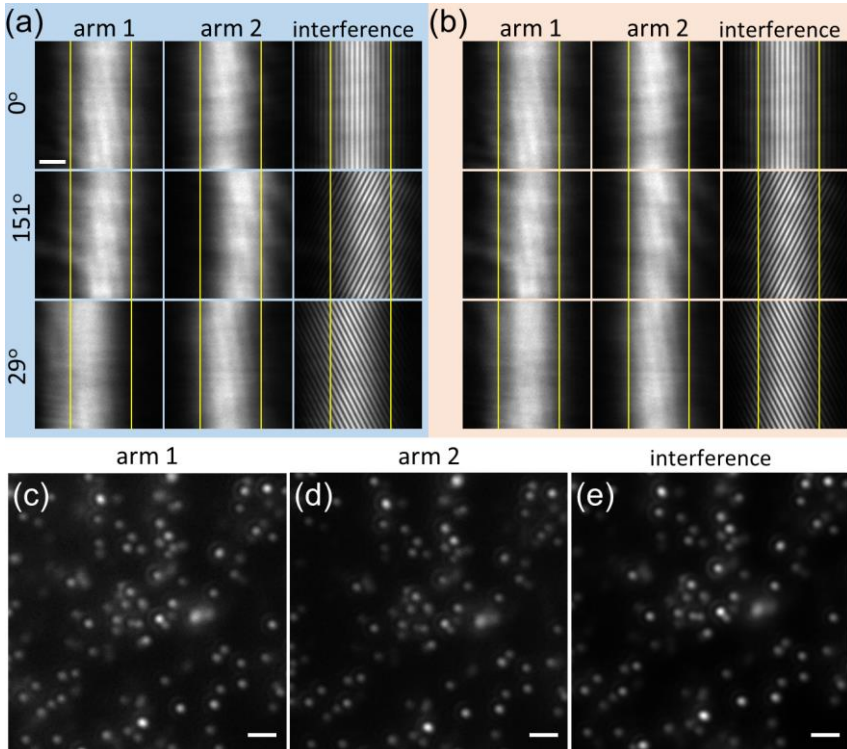
Fig.3.3 Light-sheets alignment. **(a)** Light-sheets of each illumination arm and their interference at three different orientations/rotations. The light-sheets are aligned when they remain centered, i.e. within the yellow borders, at any rotation angle. The light-sheets in arm 1 at orientation 29° and in arm2 at orientation 151° shift slightly from the center , which indicates that the alignment is not perfect. The motorized stages of scanning mirrors (fig.3.2c) allow alignment corrections to attain fully centered light-sheets and pattern as shown in **(b)**. Beads illuminated with counter-propagating light-sheets, **(c)** light-sheet from objective Ob_1 and **(d)** light-sheet from objective Ob_3. **(e)** Interference of both light-sheets. The similarity in the images from both illumination arms indicates a good alignment of the system.

Perfect manual alignment of both arms is hard to achieve, this can be seen in the slight misalignment of each of the light-sheets at one orientation, in the case of arm 1 the light-sheet shifts to the left at 117° and for the arm 2 a shift to the right occurs at 62°, these shifts are also translated to the interference pattern (fig.3.3a). To correct for this shifts and achieve even finer alignments we used the one-axis motorized stage in which the scanning lenses are mounted (fig3.2c), the final alignment can be seen in fig.3.3b, notice that the light-sheets remain centered at any orientation and so does the pattern. Under such alignment conditions the light-sheets will always travel through the focus of O_2 independently of the selected interference angle. Thus, an indication of good alignment is that when the counter-propagating light-sheets are used to illuminate a sample, the images acquired from any of the arms should completely overlap, as we demonstrate in fig.3.3c/d/e with fluorescent beads.

3.4.2   Calibration of pattern phase

The $2\pi/3$ phase steps of the illumination pattern are carried out by moving the nano-positioner (NP) in steps of 1/3 of the illumination wavelength. The value of these steps is independent of the interference angle of the light-sheets because the shift is carried out relative to the light-sheets wavefront. In case of a λ_{ill}=488 nm wavelength the NP must be moved in steps of ~163 nm, fig.3.4 illustrates the application of this step to a pattern of 301 nm. The $2\pi/3$ steps should translate in this case in pattern displacements of about 310 nm/3=103.3 nm. The profile of each pattern is plotted in fig.3.4b, taking the first phase φ_o as reference we measure the pattern displacement corresponding to the other two phases, φ_o+120° and φ_o+240° , and get a result of 103 nm, very close to the expected 103.3 nm.
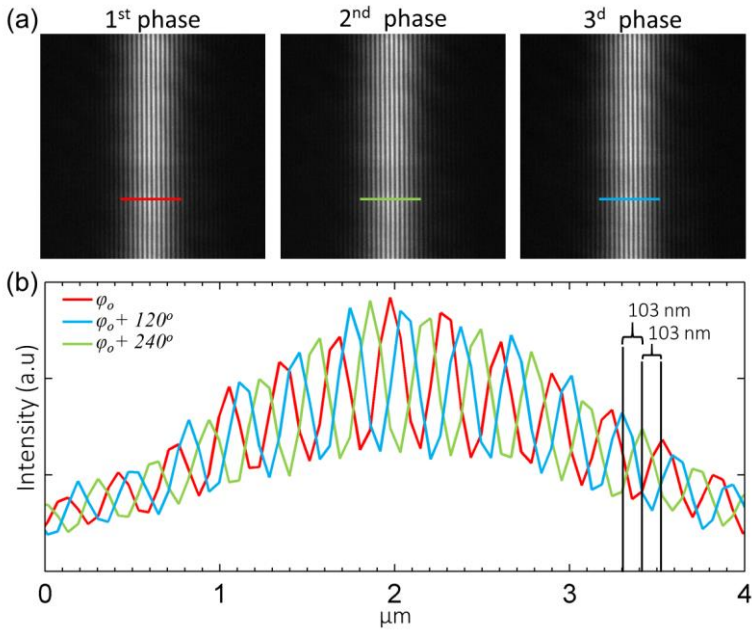
Fig.3.4 Control of the pattern phases in the csiLSFM. **(a)** Illumination pattern of 310 nm period at three different phases φ_o, φ_o +120°, φ_o+240°. The 120° phase steps are attained by shifting the illumination wavefront in steps of $\lambda_{ill}/3$. **(b)** Intensity profile of the illumination pattern. The 120° phase shifts correspond to a pattern displacement of 103 nm.
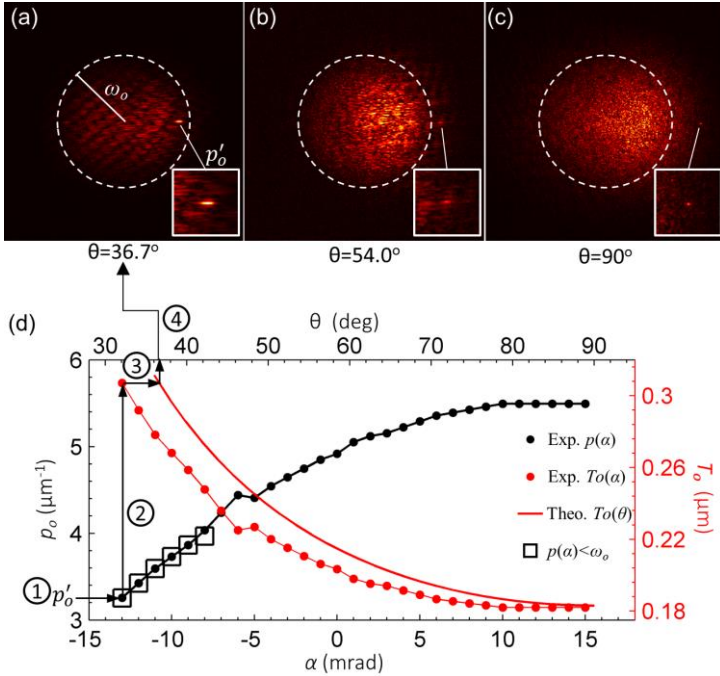
Fig.3.5 Angular displacement α vs interference angle 2θ. **(a)** Cross-correlations of central $(\tilde{S}(\vec{k})OTF)$ and extended domain $(\tilde{S}(\vec{k}-p_o)OTF)$ for three different interference angle 2θ: **(a)** $\theta=36.7°$ **(b)** $\theta=54°$ *and* **(c)** $\theta=90°$. The position of the sharp peak in the correlations gives an estimate of the pattern spatial frequency p_o (left corner bottom inset). The precise values of θ are obtained from the calibration curve in figure **(d).** To create this curve the scanning mirrors are set to certain angle α (horizontal axis bottom) and plot it against its correspondent estimation of ①p_o' (vertical axis left). ② The reciprocal of p_o' yields the experimental estimation of the pattern period T_o (vertical axis right). ③ This period is matched with the same value of the theoretical curve $T_o(\theta)$ (red solid line, eq.18) to finally ④ extract the angle θ (horizontal axis top). The black squares in the curve correspond to the p_o' that could be visually estimated since they are smaller than ω_o.

3.4.3 Calibration curve: scanning lenses angular displacement α vs interference angle 2θ

A curve that characterizes the pattern period T_o as function of the angle displacement α can be produced by extracting the period from the image and plotting it against the α. Extracting the period for optically detectable frequencies, i.e. $p_o < \omega_o$, is a direct task since the period can be measured from the image of the pattern. Nevertheless measuring the period of the patterns with a spatial frequency larger than the cut-off frequency, $p_o > \omega_o$, requires the calculation of the correlation between the central and extended domains of a SIM acquisition(eq.38).

$$\tilde{S}(\vec{k}) * \tilde{S}(\vec{k} - \vec{p}_{oj}) \tag{38}$$

This correlation produces a sharp peak because of the overlap that both domains share (fig.3.5a/b/c)[37]. The peak position is an estimate $\vec{p}'_{oj}$ of the actual pattern frequency $\vec{p}_{oj}$ and the reciprocal of its norm yields the experimental pattern period. 2D-SIM acquisitions of the beads were carried out at angular displacements α between -15 to 15 mrads. Using the SIM data for the first orientation, 0°, we extracted the frequency p'_o from the correlation in eq.38 and plotted the curve $p'_o(\alpha)$ (fig.3.5d black dotted curve). This approach is validated by the good match of the optically detected pattern frequencies (black squares) with the initial points of the curve. The reciprocal values of $p'_o(\alpha)$ yield the experimental period as function of α (red dotted curve, $T_o(\alpha)$). Matching the experimental period with its value in the theoretical curve $T_o(\theta)$ (eq.18, red solid line) leads to the argument θ and so to the interference angle 2θ. The four axis plot of fig3.5b summarizes the results of the $\theta(\alpha)$ calibration. Two landmarks are to be found in the plot: firstly $\alpha=0$ leads to $2\theta=128°$, which is only a 2° deviation from the angle of 130° between the illumination objectives. Thus, corroborating a good alignment of the light-sheets. Second, the

curve $T_o(\alpha)$ converges to ~183 nm, which is the minimum value of the theoretical curve $T_o(\theta)$ and represents the minimum pattern period provided by the csiLSFM.

3.5 Results

3.5.1 PSF and resolution measurements in the csiLSFM

We extracted the point spread function of the wide field (WF), 2D deconvolved wide field (2D DecWF) and SIM reconstruction of the csiLSFM by imaging fluorescent beads of 40 nm in diameter (F8759,Invitrogen,515 nm emission peak) embedded in a phytagel column (sec.3.3.4). Three different image stacks were acquired, one with a period of 297 nm and two with 183 nm, which correspond to generic resolution gains of 2 and 2.4 generic respectively (eq.33,35). The pattern orientations for the first pattern were 0°, 48°, 130°, and for the second one 0°, 33°, 150°.

30 beads were selected from the first stack (T_o=297 nm) and 60 in total from the other two (T_o=183 nm). Images of the wide field and the SIM reconstruction can be seen in fig.3.5a-d. The SIM reconstruction was carried with our reduced artifact algorithm which will be introduce in chapter 4. The 2D deconvolution was applied by deconvolving the raw SIM data individually, i.e. each image at each phase and pattern orientation, and then extracted from the central domain $\tilde{S}(\vec{k})OTF$. The *PSF* used for deconvolution was calculated from eq.3. The wide field image was also extracted from the central domain but from the non-deconvolved data.

The lateral and axial resolutions d_{xy} and d_z were obtained by fitting the intensity profile of each selected bead to eq.8. The fitting was done with the Fiji plug-in metroloJ[54]. The experimental resolution measurements are

summarized in tables 3.1. The result to highlight there is the resolution of $d_x=87$ nm achieved with the 183 nm pattern, superior to the 117 nm of the 297 nm pattern.

A second method we used to measure the resolutions was summing all the 3D intensity profiles of the beads to obtain the average bead, this calculation was carried out with the commercial software Amira. Figs.3.6g/h show the average bead of the wide field and SIM reconstruction respectively, we fitted their xy, yz and xz projections to a Gaussian curve and extract the FWHM as estimate of the resolution (fig.3.6i/j/k). The obtained results are: for the SIM reconstructions $d_x=87$ nm, $d_y=108$ and $d_z=898$, and for the wide field $d_x=281$ nm, $d_x=297$ nm and $d_x=898$ nm. These values do not differ greatly from those in table 3.1.

A small anisotropy of 1.045 was detected in the lateral resolutions of the wide field measurements since as seen in table 3.1 d_y is slightly large than d_x. We theorize that the source of this difference is a lensing effect in the x-axis caused by the cylindrical shape of the phytagel column. The short axis of the column is parallel to the x-axis of the image (fig.3.2e), hence a small difference in refractive index between the immersion medium and the phytagel is translated into a (de)magnification factor. Table 3.2 shows the d_x resolutions of table 3.1 after multiplying them by 1.045, this operation yields the corrects resolution along the x-axis, obtaining now a resolution of 122 and 91 nm for the 297 and 183 nm pattern periods respectively.

The experimental results are comparable to the theoretical values shown in table 3.3; where eqs.5,32 and 37 were used to calculate the WF, 2D DecWF and SIM resolutions respectively.
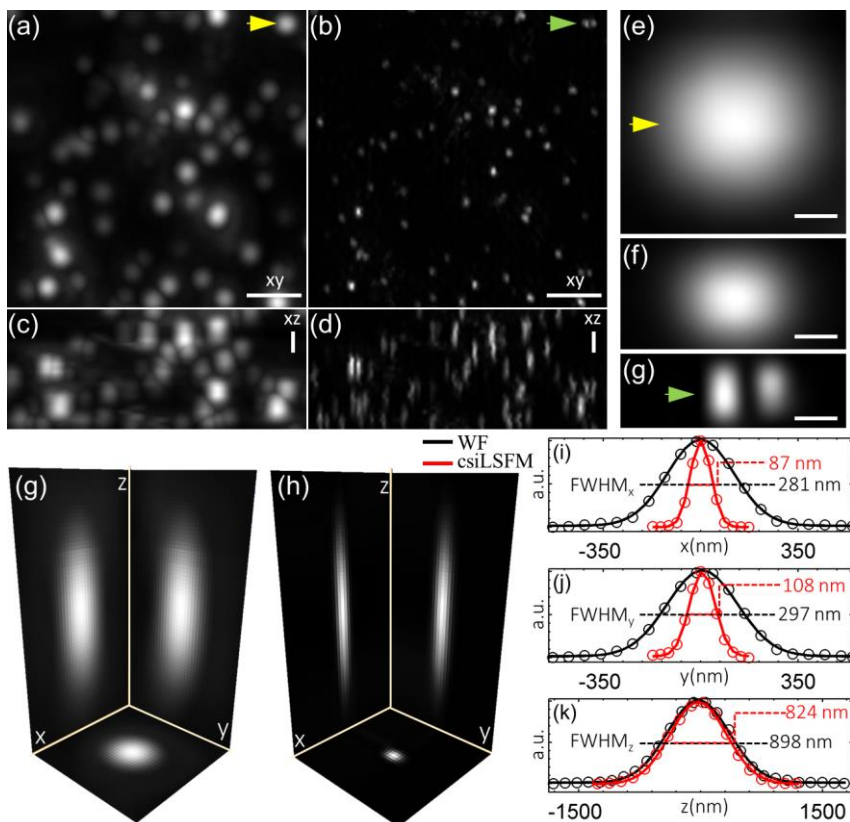
Fig.3.6 PSF of the csiLSFM with the counter-propagating light-sheets. 6 µm stack of fluorescent beads (40 nm diameter). **(a/c)** wide field and **(b/d)** SIM reconstruction of *xy/xz* maximum intensity projections. **(e)** Extract from the wide field (yellow arrow) and its **(f)** 2D deconvolved image, the **(g)** SIM reconstruction allows to distinguish two beads rather than a blob of light (green arrow). Rendering of the average PSFs of the **(h)** wide field and **(i)** SIM. The average was calculated from 60 beads. **(j/k/l)** Intensity profiles (solid line curves) of the average PSFs along its long and short axis; a Gaussian function (dotted curves) has been fitted to estimate the FWHM along *x,y* and *z*.

Resolution (nm)	WF	2D DecWF	SIM (T_o=297 nm)	SIM (T_o=183 nm)
d_x	288 ± 9	180 ± 8	117 ± 11	87 ± 11
d_y	301 ± 11	192 ± 9	130 ± 10	110 ± 13
d_z	922 ± 111	826 ± 87	826 ± 112	830 ± 142

Table 3.1 Experimental resolution values.

Resolution (nm)	WF	2D DecWF	SIM (T_o=297 nm)	SIM (T_o=183 nm)
d_x	301 ± 9	188 ± 8	122 ± 11	91 ± 11

Table 3.2 Corrected experimental resolution along the *x*-axis.

Resolution (nm)	WF	2D DecWF	SIM (T_o=297 nm)	SIM (T_o=183 nm)
d_{xy}	314	206	120	97
d_z	1373	1373	1373	1373

Table 3.3 Theoretical resolution values.

3.5.2 Resolution gains in the csiLSFM

From the d_x values of tables 3.2 and 3.3 we calculated the theoretical and experimental maximum resolution gains of the csiLSFM. The gain was calculated respect to the wide field and the deconvolved wide field. The results are shown in table 3.4. Our resolution calculations are validated by the similarity between the theoretical and experimental values. An effective resolution gain of 3.3, very close to the 3.2 predicted in eq.36, has been attained with the counter-propagating light-sheets.

Resolution gain	WF/ 2D DecWF		2D Dec WF/ SIM(T_o=183 nm)		WF / SIM(T_o=183 nm)	
	Theo.	Exp.	Theo.	Exp.	Theo.	Exp.
rg	1.5	1.6	2.1	2.1	3.2	3.3

Table 3.4 Theoretical and experimental maximum resolution gains along the *x*-axis with the csiLSFM.

3.5.3   SIM resolution uniformity in the csiLSFM

Another factor to explore is the isotropy/anisotropy of the SIM resolution obtained with the csiLSFM(table 3.5).   The resolutions d_x and d_y are different (table 3.1) because as explained in sec.3.2.2 the pattern rotation in the csiLSFM is limited to 48° which does not cover the 60° necessary for an isotropic resolution gain like in the epi-fluorescence configuration. Yet the ratio d_y/d_x indicates that the csiLSFM is closer to an isotropic resolution than the other method that combines light-sheet microscopy and SIM, i.e. the lattice light-sheet fluorescence microscope (LLSFM) (table 3.1). Nevertheless, since the csiLSFM presents no axial resolution gain since it is a 2D-SIM implementation, hence having a worse d_z/d_x ratio than the 3D-SIM methods.

Resolution uniformity	Epi-fluorescence (3D-SIM)	LLSFM (3D-SIM)	csiLSFM (2D-SIM)	
			T_o=297 nm	T_o=183 nm
d_y/d_x	1	1.5	1.1	1.2
d_z/d_x	3	1.9	6.8	9

Table 3.5 Resolution uniformity along different directions for various SIM set-ups.

3.5.4   Imaging of biological samples at resolution gains >2 with the csiLSFM

Figs.3.7c and 3.8c show the SIM reconstructions of two biological samples, a cell immune-stained against α-tubulin and wild yeast with its endoplasmic reticulum (ER) GFP-tagged.   Their resolution gain is noticeable when compared to their corresponding wide field or the deconvolved images. We visually estimated the gain from the SIM image spectrum by outlining it with two concentric circles of radii ω_o and $2\omega_o$ (fig.3.7f/3.8f).   Information beyond $2\omega_o$ can be found in both cases α-tubulin and ER indicating a resolution larger than 2, nevertheless the amplitude of those frequencies is larger in the former sample than in the

latter even though both were illuminated with the same pattern period. The cause of this is the effective modulation of the pattern, which is influenced by the SNR and sample structure. To obtain significant resolution gains, SIM requires optimal modulation values and during the running time of the csiLSFM project these value had not yet been quantified so no method to evaluate whether a SIM acquisition would result in a significant resolution gains or not was not available. In chapter 5 we present a quantitative criterion, called the Q-factor, to evaluate the modulation as function of the experimental acquisition parameters, such as SNR, laser power, exposure time, pattern period and sample structure. Since the purpose of the current chapter is to demonstrate the large resolution gains attained with the csiLSFM we will retake the discussion on the significant resolution gains in chapter 5 in terms of the Q-factor. We are aware that resolution gains > 2 entail a challenge due to the low pattern modulations, consequence of the pattern period lying beyond the cut-off frequency, but for the time being we showed that this is possible not only with fluorescent beads but also with biological samples (figs.3.7c and 3.8c).
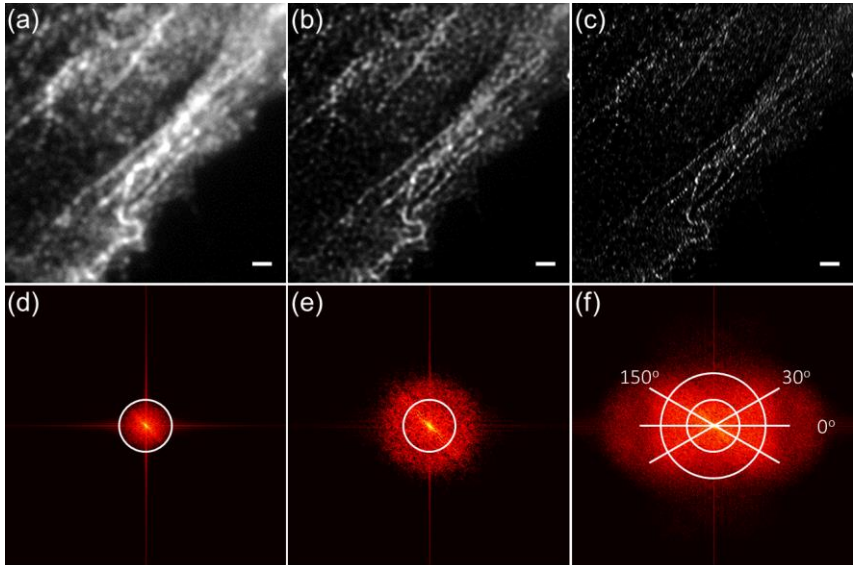
Fig.3.7 Eukaryotic cell in the csiLSFM under 183 nm pattern period. The sample is a human umbilical vein endothelial cell immunostained with α-tubulin/Alexa 488 and embedded on a coverslip. **(a)** Wide field. **(b)** 2D deconvolved wide field **(c)** SIM reconstruction. The respective power spectrum of the images can be found in **(d)**, **(e)** and **(f)**. The white circle outlines the cut-off frequency (ω_o) of the detection objective. In (f) a second circle with radius $2\omega_o$ has been added as well as adjacent lines indicating the illumination pattern direction (150°, 30°). Scale bar:1 μm.
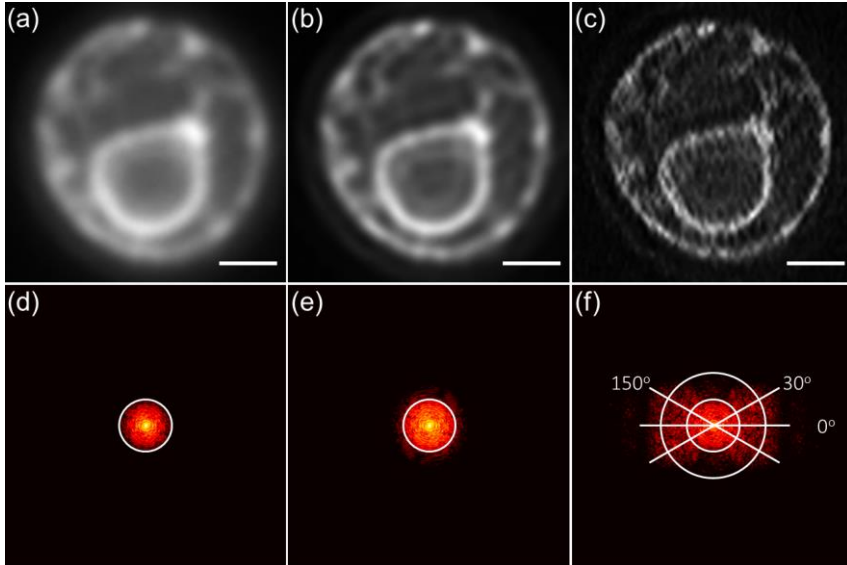
Fig.3.8 Yeast sample in the csiLSFM under counter-propagating light-sheets. The sample is wild type yeast with its endoplasmic reticulum GFP-tagged and embedded in a phytagel column. **(a)** Wide field. **(b)** 2D deconvolved wide field **(c)** SIM reconstruction. The respective power spectrum of the images can be found in **(d)**, **(e)** and **(f)**. The white circle outlines the cut-off frequency (ω_o) of the detection objective. In **(f)** a second circle with radius $2\omega_o$ has been added as well as adjacent lines indicating the illumination pattern direction (150°, 30°). Scale bar:1 µm.

3.6   Discussion

The main goal of our csiLSFM set-up was to demonstrate that resolution gains larger than 2 are possible with linear SIM. We achieved so by decoupling the illumination and detection paths based on the light-sheet microscopy principle. The csILSFM is based on a triangular three objective configuration that allows pattern periods out of the standard resolution of the detection objective. By counter-propagating two light-

sheets we casted an illumination pattern of 183 nm with a 488 nm wavelength laser (fig.3.5a). This period led to a generic resolution gain of 2.4 (eq.35) and an effective resolution gain of 3.3 times respect to the wide field resolution (table 3.4). The maximum attainable resolution of in the csiLSFM was experimentally measured and resulted in 91 nm (table 3.2). These experimental results were validated when compared to the theoretical values (tables 3.1-3.4). The 91 nm resolution is outstanding considering that the detection objective was water immersion with an NA=1. Such sub-100 nm resolutions are only reported in TIRF-SIM microscopes which require NAs>1.45[45,55,56]. The high resolution gain in the csiLSFM can be appreciated in the pair of beads of figs.3.6e/f/g.

A demonstration of resolution gains larger than two in biological samples with the csiLSFM was shown in sec.3.5.4, though the success of attaining such gains depends highly on the sample structure. We empirically noticed that discrete biological structures, like the α-tubulin of fig.3.7c, are more likely to yield good SIM reconstructions than packed ones. The reason for this is that the sample structure affects the effective pattern modulation, discrete structures allow the display of a high modulation but packed structures undermine it. A low pattern modulation difficults the extraction of high spatial frequencies, therefore optimal modulations are required to produce significant resolution gains. Deriving those optimal conditions is the topic of chapter 5, there we will develop a metric to assess the feasibility of attaining large gains in SIM and resume the discussion of resolution gains>2 in the csiLSFM.

Combining light-sheet microscopy and SIM for super-resolution is a relatively new approximation which has in the lattice light-sheet fluorescence microscope its most functional and representative set-up[36,46,57,58], yet there is always space for improvement and the configuration of the csiLSFM offers lateral resolutions closer to isotropy

than the LLSFM (table 3.5). This is thanks to the two illumination objectives of our set-up that provide a flexible control of the pattern rotation, which is a feature lacking in the LLSFM. Of course, being a 2D-SIM implementation our set-up does not offer an axial resolution gain but its design can serve as basis for future structured illumination+light-sheet microscopes that aim at isotropic resolutions. In fact a three objective configuration similar to the csiLSFM has already been suggested for isotropic super-resolutions in the LLSFM[59].

4 Pre-reconstruction filtering strategy to reduce periodic artifacts in super resolution images

4.1 Spectra analysis of artifacts

In this section we carry the spectral analysis of two kinds of artifacts in SIM reconstructions: 1) periodic artifacts arising from out-of-focus fluorescence and 2) side-lobe artifacts owed to a drop of information in the reconstruction spectrum. The analysis served to design a filtering strategy to reduce these artifacts in a direct manner[37], without requiring the empirical parameter tuning strategy that is usually implemented.

4.1.1 Intensity modulated out-of-focus fluorescence as source of periodic artifacts

We illustrate the problem in fig.4.1a, the wide field image on the left column indicates with a yellow arrow the out-of-focus signal of a fluorescent beads sample. The SIM reconstruction in the center was carried with eq.25, i.e. without any optimization processing. The reconstructed image brings a resolution gain which can be noticed in the two beads marked by the blue arrow, they are not distinguishable in the wide field but they are in the SIM reconstruction. Despite the increase in resolution this image presents periodic artifacts that occur in the areas where out-of-focus signal is present in the wide field. The same can be noticed on fig.4.1b notice that the left side (yellow arrow) of the beads presents out-of-focus signal but not the right one. This is correspondingly translated into periodic artifacts on the left side but not to the right side of the SIM reconstruction. Finally the same effect is seen in the mitochondria

images of fig.4.1c, the SIM reconstruction provides higher resolution but the image quality is strongly reduced by the periodic artifacts.

So what causes these artifacts and why do they arise in the reconstruction?. In fig.4.2a we show a simulated sample as pairs of beads arranged in a two columns, the in-focus sample was produced by convolving the beads with a *PSF* of NA=1 and λ_{em}=515 nm (eq.3). To represent the out-of-focus signal we created a second image by shifting the beads to the right and convolved them with the *PSF* corresponding to NA=1 and a wavelength three times larger than the 515 nm (eq.3). We simulated a 2D-SIM acquisition on the beads by illuminating the in-focus image with a modulation of M=0.4 and the out-of-focus image with two different pattern conditions: no modulation (M=0) and a modulation of M=0.5. Phases and orientations were the same for the in-focus and out-of-focus images, hence due to the linearity of the convolution and of eq. 25 the reconstruction is formed by two components, the in-focus (IF) spectrum plus the out-of-focus (OF) spectrum:

$$O_{SIM}(x,y,z) = \left\| \sum_{u}^{N} \exp(\vec{r} \cdot \vec{p}'_u)\, FT^{-1}\{ (\tilde{\boldsymbol{S}}^{\text{IF}}(\vec{k} - \vec{p}_u) + \tilde{\boldsymbol{S}}^{\text{OF}}(\vec{k} - \vec{p}_u)) OTF(\vec{k}) \} \right\|, \quad (39)$$

The non-modulated out-of-focus signal (M=0) does not bring artifacts to the reconstruction (fig.4.2a) but the periodic artifacts arise in the case of M=0.5. The spectrum of coarse features in an image, e.g. the out-of-focus fluorescence, is only formed by the low frequencies found in the center of the *OTF*. The spectrum of the reconstruction in fig.4f shows prominent amplitude peaks in the center of the extended domains (blue arrows), which correspond to the shifted $\tilde{\boldsymbol{S}}^{\text{OF}}$ frequencies. Because the frequency content of $\tilde{\boldsymbol{S}}^{\text{OF}}$ is only comprised by low frequencies its span is not large enough to generate a continuous spectrum of the OF features, thus

generating isolated information domains that produce the periodic artifacts. As it is well known in spectral analysis, periodic features in real space correspond to discrete points in the frequency space. Although in this case the $\tilde{S}^{OF}(\vec{k} - \vec{p}_u)$ domains are not points they are discrete regions of information that cannot be connected to each other, this situation is depicted in fig.4.2g/h.

The OF signal does not form discrete islets in the case M=0 (fig.4.2.e), because with M=0 the domains $\tilde{S}^{OF}(\vec{k} - \vec{p}_u)$ does not even exist except for the central one, i.e. $\tilde{S}^{OF}(\vec{k})$, hence no artifacts are originated.
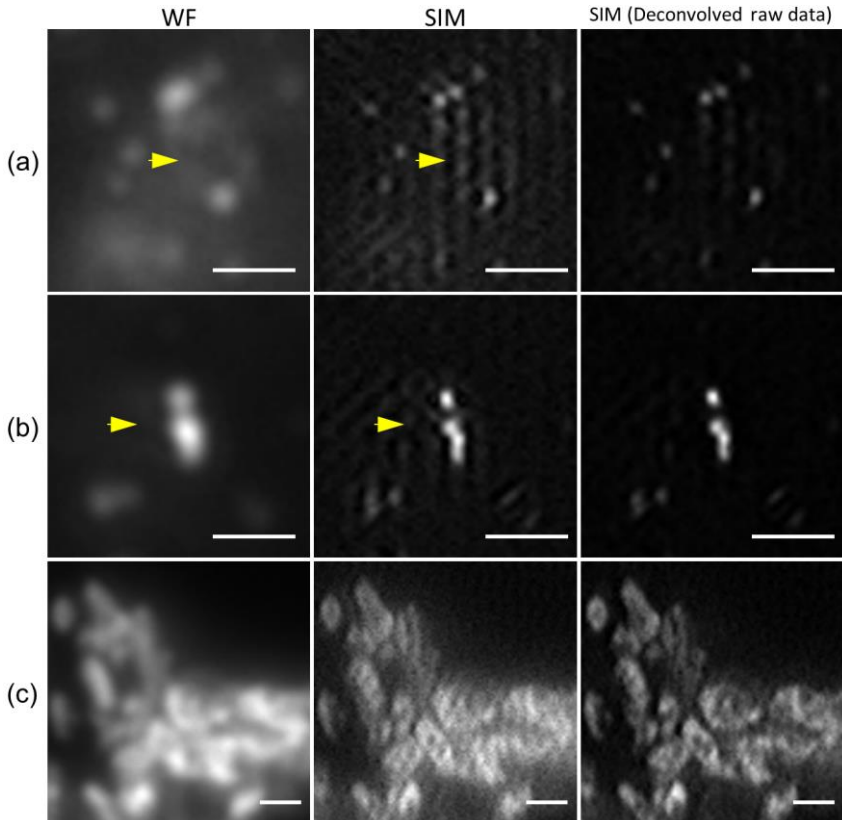
Fig.4.1 Periodic artifacts in SIM reconstructions. **(a/b)** Fluorescent beads. **(c)** Immunostained mitochondria in Hep G2 cell. Left: wide field. Center: SIM reconstruction without any optimization (eq.25). Right: SIM reconstruction using the 2D deconvolved raw data. Out-of-focus background is converted into periodic artifacts by the SIM reconstruction, if this background signal is reduced before reconstruction the artifacts are also diminished (yellow arrows). Scale bar: 1 µm.
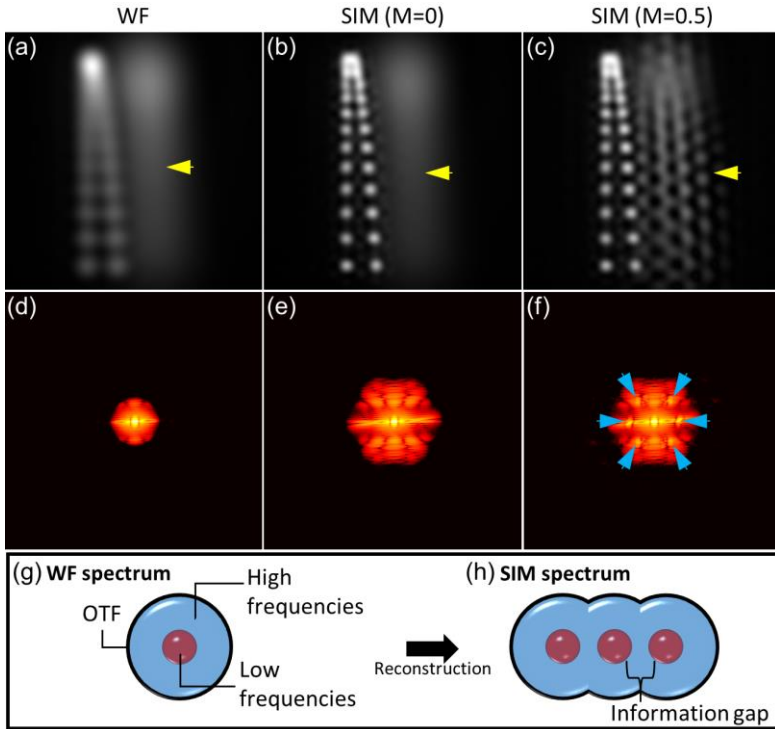
Fig.4.2 Simulating periodic artifacts in SIM. **(a)** Wide field composed by in-focus and out-of-focus signals (yellow arrow). The in-focus component is always illuminated under a pattern modulation of M=0.4 and the out-of-focus component has two conditions M=0/0.5. **(b)** SIM reconstruction with a non-modulated out-of-focus signal (M=0). **(c)** SIM reconstruction with modulated out-of-focus signal (M=0.5). **(d)** Power spectrum of the wide field. **(e/f)** Power spectrum of the SIM reconstructions in both modulation conditions (M=0/0.5). The modulated out-of-focus fluorescence is shifted by the reconstruction process, thus forming discrete frequency domains (blue arrows) that transform into periodic artifacts in real space. **(g)** Sketch of the frequency content in the *OTF*, out-of-focus signals correspond to low frequencies concentrated in the center of the *OTF* (red domain). **(h)** In the SIM reconstruction this low frequency domains form information gaps that originate the periodic artifacts.
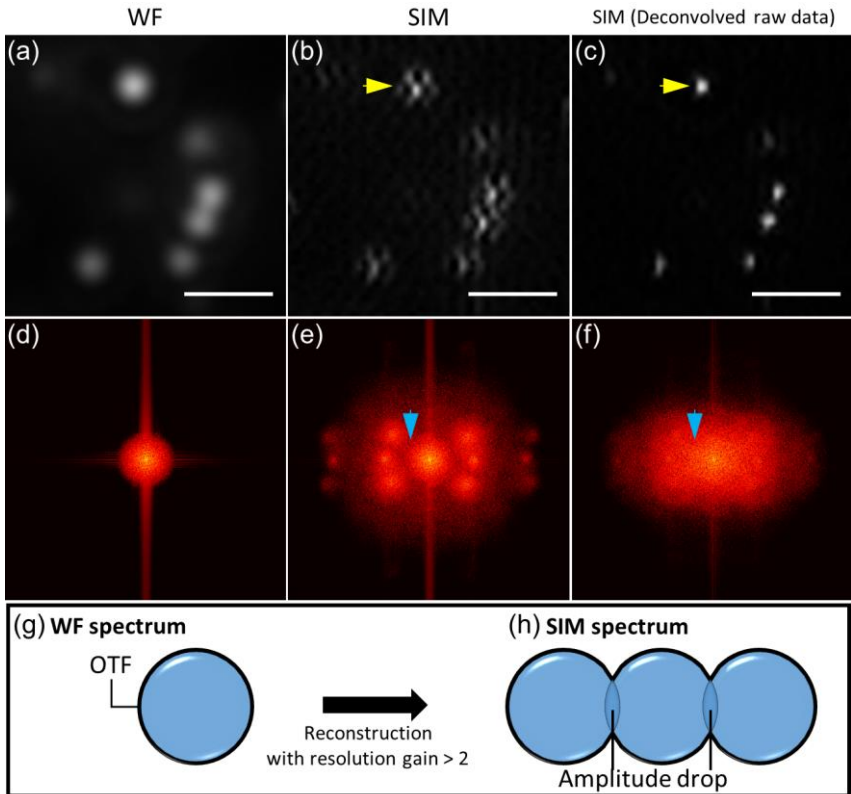
Fig.4.3 Origins of lobe-like artifacts in SIM reconstructions. Fluorescent beads. **(a)** Wide field. **(b)** SIM reconstruction without any optimization (eq.25) displaying lobe-like artifacts around the beads (yellow arrow). **(c)** SIM reconstruction using the 2D deconvolved wide field images. And their corresponding power spectra **(d/e/f)**. Low pattern modulations or large resolution gains ($rg>2$) create drops in the amplitude of mid-range frequencies (blue arrow in (e)). This drops are the origin of lobe-like artifacts but they can be eliminated by using the deconvolved data to reconstruct the image. **(g)** Sketch of the OTF. **(h)** SIM reconstructions with large gains decrease the overlap between extended and central domains, thus hindering the amplitude of mid-range frequencies. Scale bar: 1 µm.

4.1.2 Spatial frequency amplitude drops as source of lobe-like artifacts.

Fluorescent beads have been imaged with the csiLSFM using the counter-propagating light-sheets, the reconstruction carried with eq.25 yields an image with the beads surrounded by a flower-like pattern or lobes (fig4.3b). The spectrum of this reconstruction shows a clear amplitude drop in a rim just around the cut-off frequency(fig.4e blue arrow). The information drop occurs because by aiming at large resolution gains the extended domains $\tilde{S}(\vec{k} - \vec{p}_u)OTF$ are shifted further away from the center of the spectrum, hence reducing its overlap with the central domain (fig.2.3e). The mid-range frequencies of the SIM reconstruction spectrum suffer particularly from this decreased overlap because the *OTF* inherently assigns more weight to the frequencies in its center than to those in the rim of the cut-off value. This produces noticeable amplitude drops in the spectrum (fig.4.3e) that translate into lobes in the real space. The cause of the lobe-like artifacts is not to be confused with the cause of the periodic artifacts (fig.4.2g/h), in the latter information gaps are formed while in the former the amplitude of the information drops (fig.4.3g/h).

Analyzing the side-lobe artifacts with beads as we just did, allows to have a representation of how the *PSF* is aberrated by the artifacts. In an image of a biological structure the side-lobes associated to each emitter accumulate and form "echo" or "ghost" structures. TIRF-SIM reconstructions are prone to this kind of artifacts because the pattern periods used in it are just in the resolution limit of the objective[45,55], hence providing low modulations that translate into weaker extended domains. This produces the same effect of reducing the overlap between the central and extended domains, fig.4.4 provides an example of this with an α-tubulin sample. The image set was downloaded from an online

repository and corresponds to a TIRF-SIM acquisition with an emission wavelength of 525 nm[60]. The reconstruction, done with eq.25, contains several "ghost" bundles that do not appear in the wide field (fig.4.4b yellow arrows). If the spectrum of the reconstruction (fig.4.4c) is analyzed one will find that the cause of the "ghost" structures are the information drops characteristic of the side-lobe artifacts.
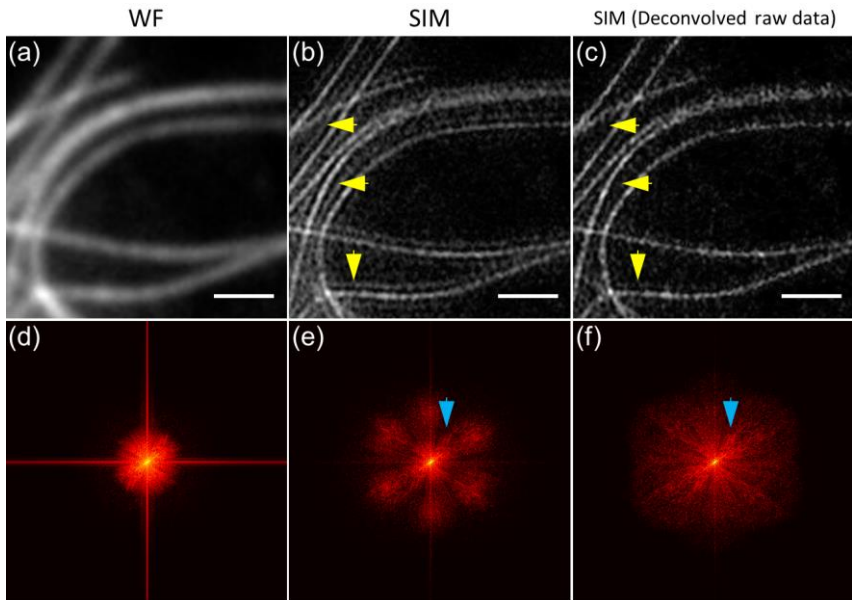
Fig.4.4 Lobe-like artifacts in biological samples. Immunostained α-tubulin. **(a)** Wide field. **(b)** SIM reconstruction without optimization. **(c)** SIM reconstructions using the 2D deconvolved data. Their corresponding spectra appear in **(d/e/f)**. The lobe-like artifacts accumulate in a complex structure to form "ghost images" (yellow arrows), in the case of image (b) there are bundles that are not originally in the wide field (yellow arrows). The spectra of (b) displays the amplitude drops (blue arrow) characteristic of the lob-like artifacts. This is not the case for the optimized reconstruction in (c). Scale bar: 1 µm.

4.2 Deconvolution of the SIM raw data as strategy to improve the reconstruction

Based on the spectral analysis of SIM artifacts we just carried out, we proposed a new reconstruction strategy to deal directly with artifact reduction[37]. The strategy consists of deconvolving the raw image data set of the SIM acquisition, then use the deconvolved data to solve eq.20/22 and apply eq.25 for obtaining the reconstruction O_{SIM}. By raw SIM data set we refer to the images $O_{ij}(\vec{r})$ acquired at phase i and pattern orientation j.

The 3D deconvolution of a stack of images acquired with patterned illumination presents a challenge that might require a spatially variant *PSF*. In order to keep our reconstruction pipeline robust we adhere to the use of a 2D deconvolution which only requires the calculation of the detection objective lateral *PSF* given (eq.3). The deconvolution of $O_{ij}(\vec{r})$ can be applied to 2D-SIM sets, i.e. $i=3$ and $j=3$, or to 3D-SIM sets (i=5, j=3). The deconvolution method we selected was the Richardson-Lucy (R-L) algorithm because compared to the Wiener filter that is usually applied in SIM, it does not require parameter tuning. R-L deconvolution is an iterative Bayesian method that accounts for the Poisson noise in the camera and requires few iterations to reduce out-of-focus signal and enhance high frequencies[61,62]. The algorithm is available in both commercial and open source software like fiji[63], we used the MATLAB implementation of this algorithm. The general inputs for this method are the *PSF*, which we calculated from eq. 3, and number of iterations, which we estimated less than 20 as an optimal value[36], in practice we always applied the R-L deconvolution with 10 iterations[36,37].

This new pre-reconstruction deconvolution strategy that we propose brings direct image quality enhancement by addressing the artifacts sources before the data undergoes the reconstruction process.

4.2.1 Reduction of periodic artifacts

The deconvolution of the raw data reduces the amplitude of the low spatial frequencies associated to the out-of-focus background, thus reducing the periodic artifacts because the out-of-focus signal has been filtered out. The third column of figs.4.1a/b/c shows the increased quality of the SIM reconstruction thanks to the pre-reconstruction deconvolution. The periodic artifacts around the beads are barely visible now and the mitochondria sample presents more recognizable features since the periodic artifacts are not imprinted on top of the reconstruction.

4.2.2 Reduction of lobe-like artifacts

During the decovolution process the frequencies at the edge of the cut-off value are boosted so their amplitude is increased. This helps to enlarge the overlap between the extended and central domains eliminating the lobe-like artifacts. The beads reconstructions in figs.4.3c clearly demonstrate this, the flower-like patterns around the beads do not appear anymore and the spectrum (fig.4.3f) looks more regular now that all the domains overlap. Similarly occurs for the α-tubulin bundles of fig.4.4, the "ghost" structures appearing in fig.4.4b do not show up in the reconstruction using our approach at fig.4.4c (yellow arrows). The improvement is also seen in the reconstruction spectrum in fig4.4f as it presents a more regular profile without the amplitude drops seen in the spectrum of fig.4.4e.

4.2.3 Enhancing the extraction of the pattern frequency

As we explained in section 3.4.3 the cross-correlation between the central extended domains shows a sharp peak whose position gives an estimate of the spatial frequency of the illumination pattern (eq.38, fig.3.5a/b/c). Extracting the peak is not always straightforward and weighted cross-correlations are suggested to enhance the result of the correlation[38]. In our reconstruction strategy the cross-correlation is directly enhanced because

the overlap of the domains has been enlarged. Fig.4.5 illustrates this with the α-tubulin data set of fig.4.4, there the cross-correlation for the third pattern orientation has been calculated to extract p_o' and $-p_o'$. Figs.4.5a/b show the result of the correlation using the unprocessed raw data, the area where the peaks is expected is indicated by a blue arrow and enlarged in the figure inset displayed at the right bottom corner; no clear peaks are detected. Figs.4.5c/d show the same correlation but using the deconvolved raw data, in this case the peaks are clearly visible facilitating the estimate of the spatial frequencies p_o' and $-p_o'$.

$$\tilde{S}(\vec{k}) * \tilde{S}(\vec{k} - \vec{p}_{o3}) \qquad \tilde{S}(\vec{k}) * \tilde{S}(\vec{k} + \vec{p}_{o3})$$
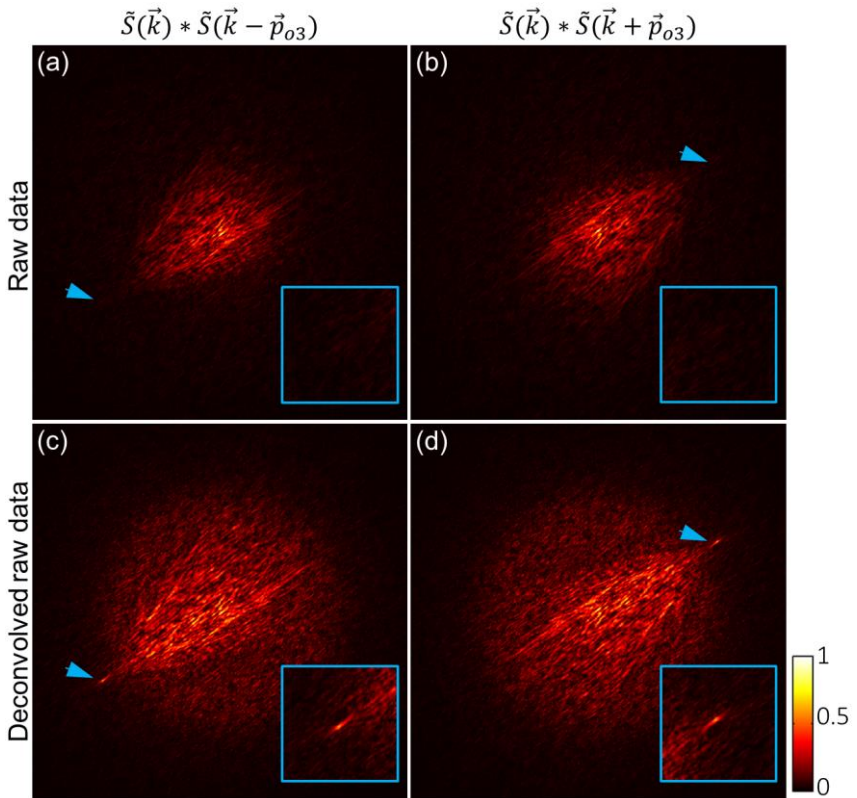
Fig. 4.5 Deconvolution of SIM raw data enhances the extraction of the pattern frequency. Cross correlation between the central and (a) right shifted extended domain, (b) left shifted extended domain, (c) right shifted extended domain from the deconvolved SIM data and (d) left shifted extended domain deconvolved SIM data. The blue arrow indicates the area where the estimate of p_o is expected, a magnification of the area is shown in the insets at the bottom left corner.

4.3 Deconvolution of the SIM reconstruction for further improvement

4.3.1 2D Post-reconstruction deconvolution

A deconvolution can be applied to the reconstruction O_{SIM} in order to emphasize high frequencies and maximize resolution gain. This is equivalent to the deconvolution applied on multi-view image fusion to enhance the contrast of the reconstructed image[64]. Since Richardson-Lucy deconvolution is an iterative method this second deconvolution step can be seen as the continuation of the one performed on the raw images but with an extended *PSF*. Based on eq.25 this extended *PSF* is given by:

$$PSF_{SIM}(x, y, z) = \left\| \sum_{j=1}^{3} \sum_{u=1}^{N} exp(\vec{r} \cdot \vec{p}'_{uj}) \, FT^{-1}\{OTF(\vec{k})\} \right\|, \qquad (40)$$

i.e. the OTF of the detection objective is displaced according to the spatial frequencies $\vec{p}'_{uj}$ to form the footprint of the extended point spread function (PSF_{SIM}). We used PSF_{SIM} to deconvolve the reconstruction O_{SIM} with the R-L algorithm, in order to not pass the 20 iterations we restricted this second deconvolution step to 5 to 10 iterations.

The performance of the post-reconstruction deconvolution is demonstrated in fig.4.6. The reconstruction of the mitochondria sample in fig.4.1c (third column) is shown in fig.4.6a next to its deconvolved version (fig.4.6b), this latter image displays a higher contrast than the former. The intensity profile of the PSF_{SIM} for this data set can be seen in fig.4.6e, the deconvolution with this function has emphasized certain frequencies of the reconstruction, this can be seen when comparing the spectra of both images (fig.46c/d). The region of the emphasized frequencies can be identified in fig.4.6f where the circular average of both spectra has been plotted. There

we have marked with two horizontal arrows the region in which the frequencies of the deconvolved reconstruction (red line) are above the one without deconvolution (black line).

4.3.2   3D Post-reconstruction of 2D-SIM images

Although the pre-reconstruction deconvolution is only applied in a 2D fashion due to the lack of a *PSF* for patterned illumination, the post-reconstruction deconvolution can be applied in a 3D manner as the function is given by PSF_{SIM}. We used the Gaussian approximation of eq.8 as 3D *PSF* and calculated its Fourier transform to obtain the OTF that eq.40 requires.

Fig.4.7 shows the deconvolved reconstructions of yeast mitochondria acquired with the csiLSFM. Fig.4.7a and 4.7b shows the 2D and 3D deconvolved reconstructions respectively.   Even though the 3D deconvolution does not increment the axial resolution dramatically it does offer a better contrast than the 2D deconvolved image. As validation of our SIM reconstruction strategy the images in fig.4.7a/b can be compared to the one in fig.4.7c, this reconstruction was carried out by another algorithm called BlindSIM[65–67]. In the next section we will compare our reconstruction strategy to other methods in order to have an assessment of their artifact reduction capabilities.
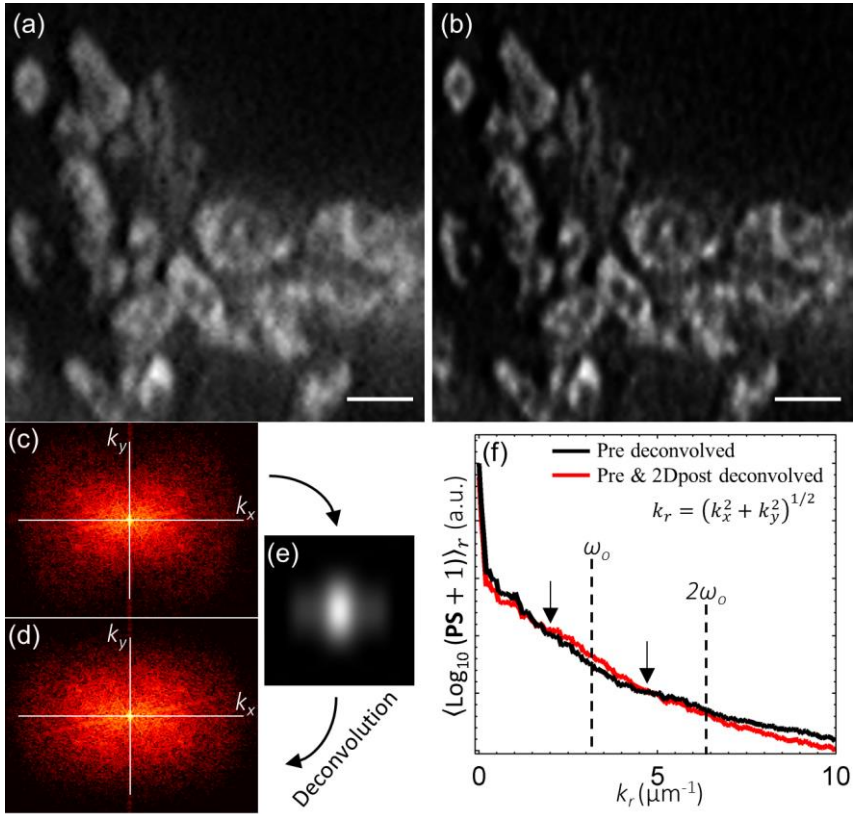
Fig.4.6 Post-reconstruction deconvolution further enhances contrast. Mitochondria sample. **(a)** SIM reconstruction using the 2D deconvolved SIM data. **(b)** Same SIM reconstruction but deconvolved with the extended PSF shown in **(e)**. **(c)** and **(d)** are the power spectra of (a) and (b) respectively. **(f)** Circular average of the logarithm of the power spectrum, the black solid line corresponds to the spectrum in (c) and red solid line to the spectrum in (d). Scale bar: 1 μm.
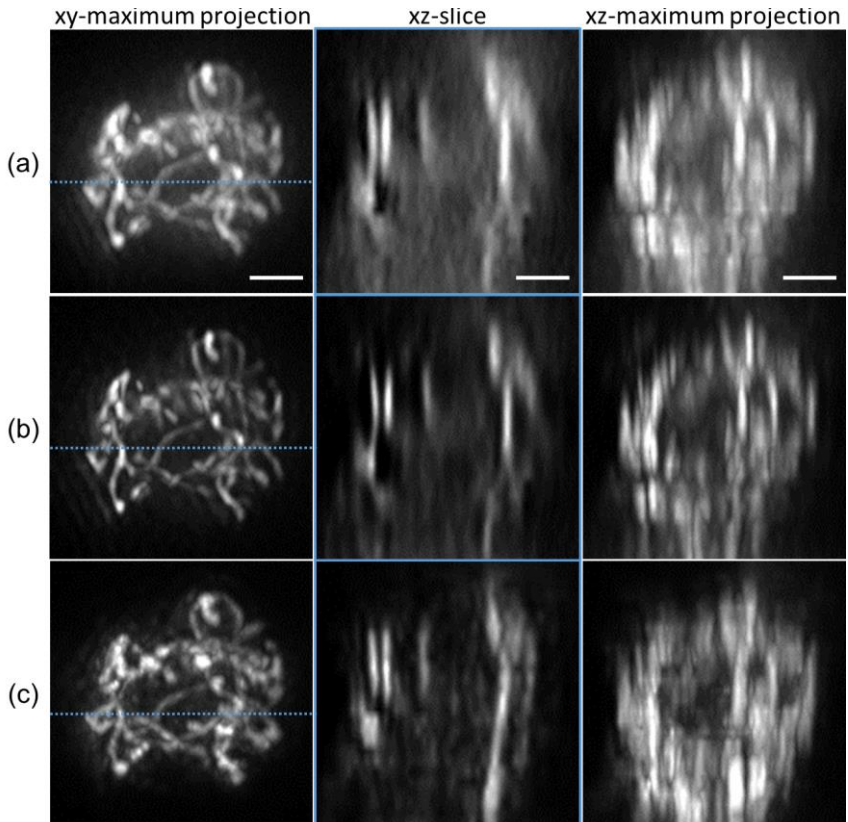
Fig.4.7 Application of 3D post-reconstruction deconvolution in 3D stacks. 2D-SIM slice-by-slice reconstructions of GFP-tagged mitochondria in yeast (5 um stack). **(a)** SIM reconstruction with 2D post-reconstruction deconvolution. **(b)** SIM reconstruction with 3D post reconstruction deconvolution. **(c)** SIM reconstruction with the Blind-SIM algorithm. Left column: *xy* maximum projection. The blue dashed line indicates the position of the *xz* slice in the central column. Right column: *xz* maximum intensity projection. Scale bar: 1 µm.

4.4   RL-SIM vs other reconstruction algorithms

The goal of any SIM reconstruction algorithm is to provide an image with resolution gain and no artifacts that hinder its quality, in one way or another the main reconstruction strategies in the literature provide these results but their processing approaches vary. In this section we compare general features of our reconstruction method, the RL-SIM, against those used in two commonly applied reconstruction algorithms, the BlindSIM and fairSIM.

The processing steps of the RL-SIM are summarized in fig.4.13b, the codes of the MATLAB implementation of this reconstruction are provided at the end of this thesis (pp.135-142). The features of our reconstruction is that it is strategically designed to reduce artifacts by addressing the artifact sources before reconstruction. The approach is direct and it needs no parameter tuning so it provides a standard and objective reconstruction procedure. BlindSIM uses a maximum a posteriori likelihood approach, in which a reconstruction is provided as a probabilistic estimation of the most suitable *PSF* and pattern intensity profile[65–67]. This algorithm offers good results and its main advantage is that it does not require a perfect sinusoidal pattern since it accounts for local pattern deformations[65], the drawback of BlindSIM is that is computationally very costly. For example, a 3D-SIM data set with an image size of 200x200x13 pixels takes 330 minutes to be reconstructed; the reconstruction time can be decreased to 25 minutes if a GPU is used to increase calculation speed (8 processors of 3.40 GHz/RAM: 32 GB)[67]. For comparison we tested the speed of our pre-reconstruction 2D deconvolution approach with a 3D-SIM data set of 256x256x13 pixels, the reconstruction took only 1.3 minutes (4 cores/2.53 GHz/RAM: 24 GB). Thus, BlindSIM can offer excellent image quality but it is very time consuming even for relatively small image sizes. A single plane of the stack presented in fig.4.7 is shown in fig.4.8, there the BlindSIM reconstruction can be compared to the result obtained by RL-

SIM (fig.4.8b/c). There are no significant differences between the two images and the main structural features in both are basically the same, though BlindSIM seems to eliminate better the residual background fluorescence in the center of the image.
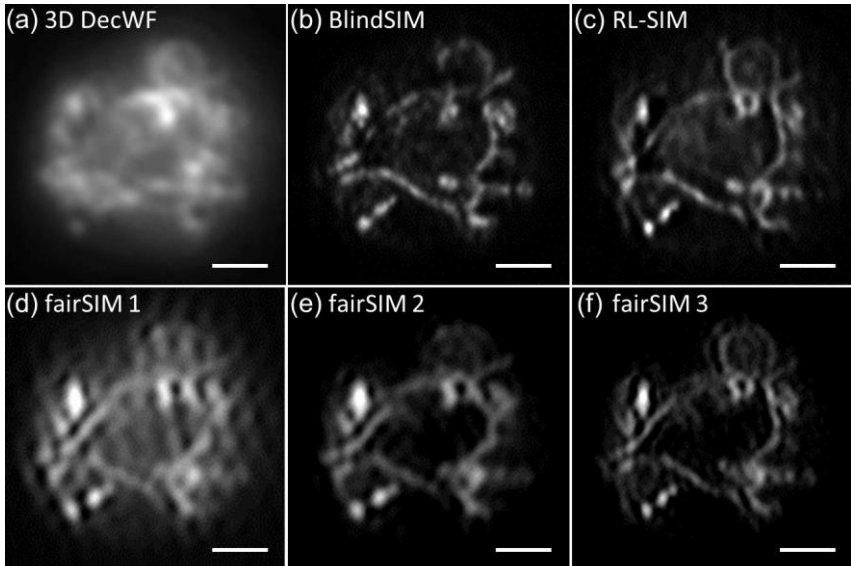
Fig.4.8 Comparison of different SIM reconstructions methods. Single plane of the stack in fig.4.7. **(a)** 3D deconvolved wide field. **(b)** Blind-SIM reconstruction. **(c)** RL-SIM reconstruction. **(d)** fairSIM reconstructions with parameters: w=0.499, a=0, d=0 μm^{-1}, Apo cut-off=$2\omega_o$, **(e)** w=0.499, a=0.990, d=1.5 μm^{-1}, Apo cut-off=$2\omega_o$, **(f)** w=0.0.499, a=0.990, d=1.5 μm^{-1}, Apo cut-off=$2.5\omega_o$. The function of each parameter can be found in eq.27 and 28 for the function of each parameter. Scale bar: 1 μm.

A second common reconstruction algorithm is the one used in eqs.27/28; a fiji implementation of this method is found in the fairSIM plug-in[50]. The strategy of this reconstruction approach is to eliminate artifacts by adjusting the reconstruction spectrum with an attenuation function (eq.28),

a Wiener filter and an apodization function $A(\vec{k})$. The fairSIM plug-in offers parameters to tune this functions, *a* and *d* define the strength and FWHM of the attenuation function respectively, see eq.28. *w* is the Wiener filter parameter and is related to the SNR of the images (eq.27). The apodization function $A(\vec{k})$ follows the footprint of the extended OTF, decaying linearly from 1 in the center of the reconstruction spectrum to 0 at certain cut-off value, this cut-off value is given as multiple of the detection cut-off frequency (ω_o) and can be tuned in the plug-in[29,50]. The main drawback of this method is that there are no general optimal values for the tunable parameters and they have to be empirically adjusted for each data set. Since the quality of the reconstruction is visually evaluated this approach can turn into a trial and error approach in which multiple attempts are required before obtaining a satisfactory result. Figs.4.8 shows three fairSIM reconstructions to be compared with those obtained by BlindSIM and RL-SIM. fairSIM 1 (fig.4.8d) presents visible artifacts since no attenuation function was applied, fairSIM 2 (fig.4.8e) and fairSIM 3 (fig.4.8f) seem to provide good results but the elimination of background signal is not as optimal as in the BlindSIM or RL-SIM images. Moreover a change in some parameters can lead to a change in the resolution gain[68], in this particular case fairSIM 2 has lower resolution than fairSIM 3 because the apodization cut-off ($2\omega_o$) of the former is smaller than the latter ($2.5\omega_o$). This is an obvious result, but it illustrates that the final outcome of the reconstruction is subjective when using a tunable parameter reconstruction strategy. Fig.4.9 provides another example of RL-SIM reconstruction vs the fairSIM approach.

Overall we can state that the RL-SIM is a balanced SIM reconstruction method as it is faster than BlindSIM while offering similar results (fig.4.8), additionally the RL-SIM does not require any parameter tuning hence it provides a standard and objective reconstruction procedure. The limitation

of RL-SIM arises when implementing it in images with low signal-to-noise ratios (SNR).
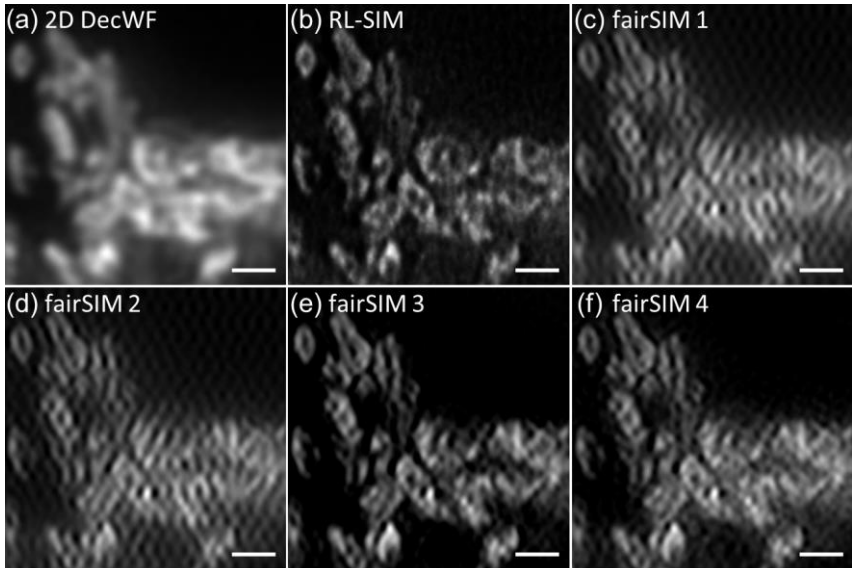
Fig.4.9 Direct reconstructions in the RL-SIM vs empirical optimization in fairSIM. Mitochondria sample of fig.4.1c. **(a)** 2D deconvolved wide field. **(b)** RL-SIM reconstruction. fairSIM reconstructions with parameters: **(c)** w=0.499, a=0, d=0 μm^{-1}, Apo cut-off=$2\omega_o$, **(d)** w=0.499, a=0, d=0 μm^{-1}, Apo cut-off=$2.5\omega_o$, **(e)** w=0.499, a=0.990, d=1.5 μm^{-1}, Apo cut-off=$2.5\omega_o$, **(f)** w=0.25, a=0.990, d=1 μm^{-1}, Apo cut-off=$2\omega_o$. Scale bar: 1 μm.

4.5   RL-SIM in commercial set-ups and in the csiLSFM

4.5.1   RL-SIM in the 3D-SIM Elyra (Zeiss)

The reconstruction steps of SIM images in commercial set-ups are usually not accessible to the user, this is compensated by offering an interface with a set of tunable parameters to improve the reconstruction in case the provided results are not optimal. The drawback of this strategy is that it requires the same trial and error approach of other reconstruction algorithms. In contrast our reconstruction method offers a direct and immediate result without the need of any empirical tuning. In many instances we found out that our reconstruction provided better results than those carried by the commercial system. Fig.4.10 and 4.11 are evidence of that, there we compared the reconstructions provided by the 3D-SIM Elyra system from Zeiss against our reconstruction. Fig.4.10a shows the reconstruction of α-tubulin molecules automatically provided by Elyra, 4.10b shows our reconstruction. Even though we only applied the first deconvolution step for this data set, the image quality of our reconstruction is noticeably better than the Elyra's, which presents plenty of artifacts (see fig.4.10c/d).

In fig.4.11 is the same case, our reconstruction (fig4.11b) offers an artifact-free image of actin fibers while the Elyra reconstruction displays some artifacts (fig.4.11a). From the spectrum of this reconstruction the origin of the artifacts seem to be the amplitude drops characteristic of the lobe-like artifacts (fig.4.11c), on the other hand the spectrum of our reconstruction does not present this drops (fig.4.11d).
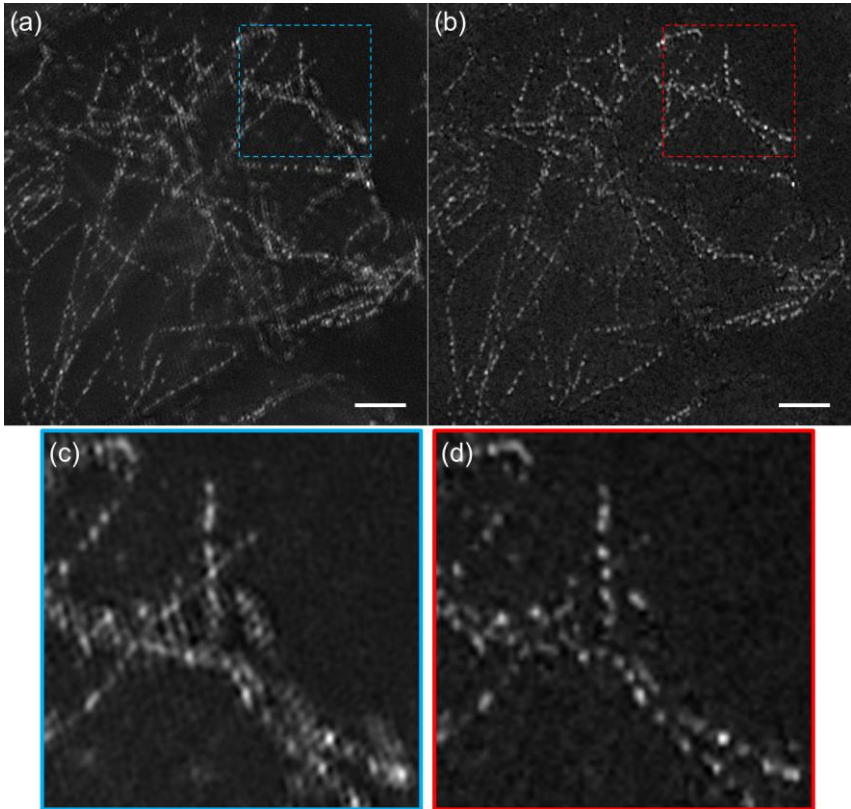
Fig.4.10 RL-SIM in commercial set-ups I. Reconstructions of single plane of α-tubulin/Alexa488 sample. Data set acquired with 3D-SIM in the Elyra Zeiss microscope. **(a)** Automatic reconstruction provided by the Elyra system. **(b)** RL-SIM reconstruction. **(c/d)** Magnification of the same region in (blue square/red square). Acquisition conditions: NA=1.4 oil immersion/Exc=488 nm/ Em=525 nm. T_o= 182.3 nm. Scale bar: 2 μm.
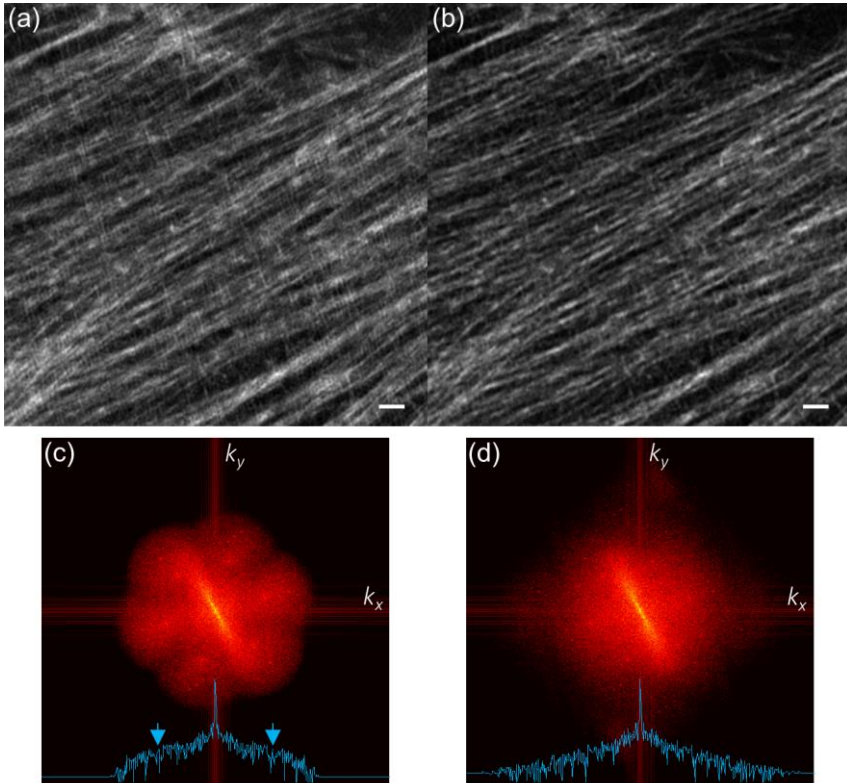
Fig.4.11 RL-SIM in commercial set-ups II. Reconstructions of single plane of actin/Alexa488 sample. Data set acquired with 3D-SIM in the Elyra Zeiss microscope. **(a)** Automatic reconstruction provided by the Elyra system. **(b)** RL-SIM reconstruction. **(c/d)** Spectra of the reconstructions in (a/b). The blue line is a plot of spectrum profile at k_y=0. The spectrum in (c) displays amplitude dips that can be observed in the blue line at the points marked by the blue arrows. This creates the artifacts that hinder the contrast in the Elyra reconstruction. The blue profile in (d) does not present such amplitude drops so the RL-SIM reconstruction looks artifact-free. Acquisition conditions: NA=1.4 oil immersion/Exc=488 nm/ Em=525 nm. T_o= 221 nm. Scale bar: 1 μm.
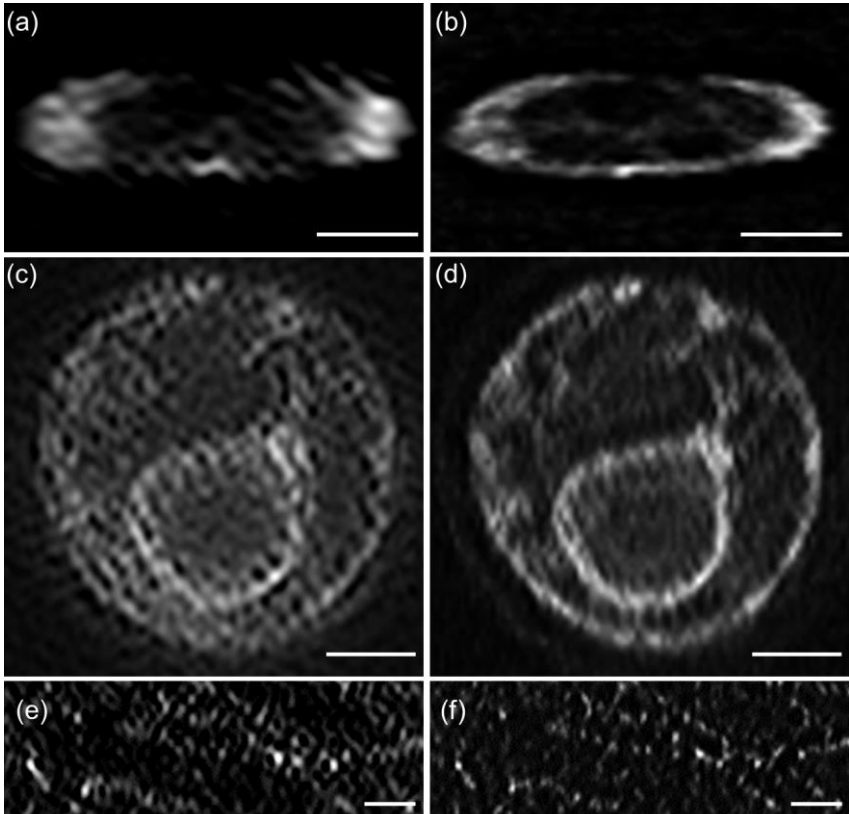
Fig.4.12 RL-SIM and fairSIM in the csiLSFM. **(a)** SIM reconstruction of E. coli sample with fairSIM; w=0.498, a=0.9995, d=1.5 μm^{-1}, Apo cut-off=2.5ω_o, **(b)** and RL-SIM. **(c)** SIM reconstruction of ER in yeast with fairSIM; w=0.1, a=0.990, d=1.2 μm^{-1}, Apo cut-off=2.5ω_o, **(d)** and RL-SIM. **(e)** SIM reconstruction of α-tubulin in HUVE cell with fairSIM; w=0.499, a=0.990, d=1.5 μm^{-1}, Apo cut-off=2.5ω_o, **(f)** and RL-SIM. Acquisition conditions: NA=1.0 water immersion/Exc=488 nm/ Em=515 nm. T_o= 244/187/208 nm. Scale bar: 1 μm.

4.5.2   The role of RL-SIM in the csiLSFM

The patterns produced in the csiLSFM are beyond the cut-off frequency of the detection objective, hence when images are acquired under this conditions two complications arise: the estimation of the pattern spatial frequency p'_o and the lobe-like artifacts. Trying to overcome these two issues with the standard reconstruction procedures (eq.26 and 27) led to unsuccessful results. The RL-SIM reconstruction was designed from the need to overcome these issues directly and many of the csiLSFM images could not have been reconstructed without its application. Fig.4.12 shows the reconstructions of two data sets acquired with the csiLSFM, yeast and E.coli, the left column presents the best result we could obtain with the fairSIM plug-in, the right column shows our reconstructions.

4.6   Discussion

In this chapter we presented a SIM reconstruction strategy to reduce periodic and lobe-like artifacts that are common in SIM. The strategy consists on the 2D deconvolution of the 2D/3D-SIM raw data set to reduce out-of-focus background and increase the extent of the OTF, both features are critical to reduce reconstruction artifacts (sec.4.2). Our reconstruction approach was designed after performing the spectral analysis of images with both types of artifacts (sec.4.1). The analysis showed that periodic artifacts arise from modulated background signals and the lobe-like artifacts from an irregular spectrum caused by weak extended domains (low pattern modulations) or high resolution gains $(rg>2)$[37].

Besides the pre-reconstruction deconvolution applied to the SIM raw data we also demonstrated that a second deconvolution can be applied to the reconstruction to emphasize the high frequencies and improve contrast (sec.4.3). The diagram in fig.4.13 shows the steps of the typical reconstruction methods and ours, the RL-SIM. While typical reconstruction implementations use a parameter tuning approach to address

periodic artifacts[38,50,68–70], ours directly delivers an artifact-reduced image, thus providing a standardized and user-independent procedure for reconstruction.

Concerning the limitations of our method, we found two: 1) The method cannot be applied to data sets with low SNR because the Richardson-Lucy deconvolution is not suited for dominant Gaussian noise. As potential outlook, the same pre-reconstruction strategy proposed here could be investigated using modifications of the Richardson-Lucy algorithm adapted to deal with low SNR[71,72]. 2) The method will not perform optimally under extreme out-of-focus signal because the pre-reconstruction deconvolution is applied in a 2D manner, therefore this will not be completely eliminated and periodic artifacts will still occur.

The key step in our approach to reduce artifacts is the deconvolution of the raw data, this might be seen as a simple change in the reconstruction strategy but according to our spectral analysis it is a logic step to implement. The effectivity of this step was tested in a commercial microscope, the 3D-SIM Elyra from Zeiss, there we were able to deliver better reconstruction quality than the one provided by the set-up software (fig.4.10 and fig.4.11). Our method demonstrated to deliver good reconstructions with data sets of both commercial and custom set-ups (fig.4.4/4.6/4.10/4.11), in the case of the images acquired with the csiLSFM, the RL-SIM was essential to provide the reconstructions since the typical method (eq.27) was not able to correctly extract the frequency p_o of the small pattern periods used in the csiLSFM (fig.4.12)[36,37].
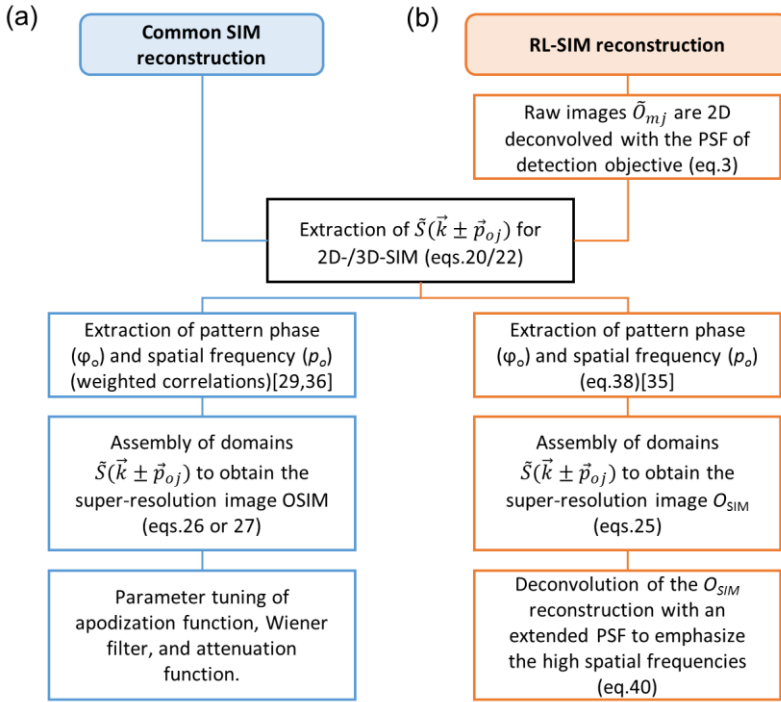
Fig.4.13 Flow chart of typical SIM and RL-SIM reconstruction.

5 *Q*-factor: a quantitative criterion for assessing raw image quality in SIM

5.1 Theory

5.1.1 Pattern modulation affects the resolution gain

SIM generates resolution gains because the spatial frequency of the pattern $(\vec{p}_o)$ shifts the spectrum of the object into the support of *OTF* (sec.2.5), hence conveying access to high frequencies that were not previously available. These frequencies are what comprised the extended domains $\tilde{S}(\vec{k} - \vec{p}_{uj})$ and their amplitude is determined by the intensity changes provided by the pattern modulation, this is made clear when explicitly solving the linear systems of eq.20 and 22; for simplicity let us take the 2D-SIM case (eq.20), for the extended domains the solution is:

$$\tilde{S}(\vec{k} \pm \vec{p}_{oj}) = 0.5 \left[\pm e^{\pm\frac{4\pi}{3}i} \left(\tilde{O}_{1j}(\vec{k}) - \tilde{O}_{oj}(\vec{k}) \right) \pm e^{\pm\frac{2\pi}{3}i} \left(\tilde{O}_{oj}(\vec{k}) - \tilde{O}_{2j}(\vec{k}) \right) \dots \right.$$
$$\left. \pm \left(\tilde{O}_{2j}(\vec{k}) - \tilde{O}_{1j}(\vec{k}) \right) \right]$$

(41)

and for the central domain:

$$\tilde{S}(\vec{k}) = 0.5^2 \left[\left(\tilde{O}_{oj}(\vec{k}) + \tilde{O}_{2j}(\vec{k}) \right) \left(e^{\frac{2\pi}{3}i} - e^{-\frac{2\pi}{3}i} \right) + \tilde{O}_{1j}(\vec{k}) \left(e^{-\frac{4\pi}{3}i} - e^{\frac{4\pi}{3}i} \right) \right]. \quad (42)$$

While the central domain is a linear combination of the spectra of the raw images $\tilde{O}_{mj}$ the extended domains are a linear combination of their differences $\tilde{O}_{mj}(\vec{k}) - \tilde{O}_{m^*j}(\vec{k})$, $m \neq m^*$. This means that the amplitude of the information in $\tilde{S}(\vec{k} \pm \vec{p}_{oj})$ is defined by how large are the intensity

differences induced by the pattern at each of its *m* phases, thus the role of the pattern modulation is to define the weight of the new spatial information and consequently the attainable resolution gain.   To demonstrate the latter statement we simulated a 2D-SIM acquisition on the beads of fig.5.1a and measure the resolution at modulation values from *M*=0 to *M*=1 in steps of 0.1 (fig.5.1d). The details of the simulation can be found in sec.5.3.1 for now it suffices to know that the WF resolution is 314 nm and that pattern period was chosen to be 257.5 nm in order to provide a maximum resolution gain of 2 (eq.33), hence the expected SIM resolution is ~150 nm. In order to not affect the resolution of the SIM reconstructions no processing, filtering or apodization were applied to the images, thus reconstructions were carried simply with eq.25.

The sample in fig.5.1a consists of pairs of beads arranged in rows, the separation of the beads in the top row is 100 nm and this distance increases by 25 nm at each row, this overlay serves as a ruler to measure resolution. The WF image of the beads and the SIM reconstructions for *M*=0, 0.1 and 1 are shown in fig.5.1a., the plots in fig.5.1b show the intensity profile in the SIM reconstructions of the beads separated by 150 nm (third row), resolving them means achieving the 2-fold resolution gain. According to the Rayleigh resolution criterion, two structures are resolved when the intensity of the two peaks is 26% larger than the valley between them (fig.5.1b)[4,73]. In terms of contrast this value translates to 0.12:

$$C = \frac{I_{peak} - I_{valley}}{I_{peak} + I_{min}} = \frac{(1.26 - 1)I_{valley}}{(1.26 + 1)I_{valley}} = 0.12. \tag{43}$$

It is clear from the profiles in fig.5.1b that not all modulation values will produce the required contrast value to consider the beads as resolved. In

fig.5.1c we plotted the contrast C for all the pairs of beads against their separation distance, the horizontal dashed red line marks the Rayleigh contrast criterion (C=0.12). According to these curves the 150 nm resolution line is only resolved for $M \geq 0.5$ (orange curve), any modulation lower than that will convey a resolution gain respect to the WF data (black dots) but it will not achieve the entire 2-fold gain. This demonstrates that the pattern modulation in SIM requires a minimum value in order to produce significant resolution gains.

The motivation of this chapter is to find this minimum modulation value for different noise levels and use it as assessment criterion for the quality of the SIM raw data, in the simulations of fig.5.1 no noise was considered and furthermore we controlled the pattern modulation M. Hence our goal is to develop a metric not to measure M but rather to measure the effective modulation displayed in the raw data. The differences $\tilde{\boldsymbol{O}}_{mj}(\vec{k}) - \tilde{\boldsymbol{O}}_{m^*j}(\vec{k})$ are an indirect measurement of this because they are affected, as we will demonstrate in sec.5.2, by the brightness of the fluorophore, the SNR and the structure of the sample. Our baseline to measure the effective modulation will be the variance of the Gaussian noise, under the logic that the differences $\tilde{\boldsymbol{O}}_{mj}(\vec{k}) - \tilde{\boldsymbol{O}}_{m^*j}(\vec{k})$ have to be above the variance level in order to produce relevant information.
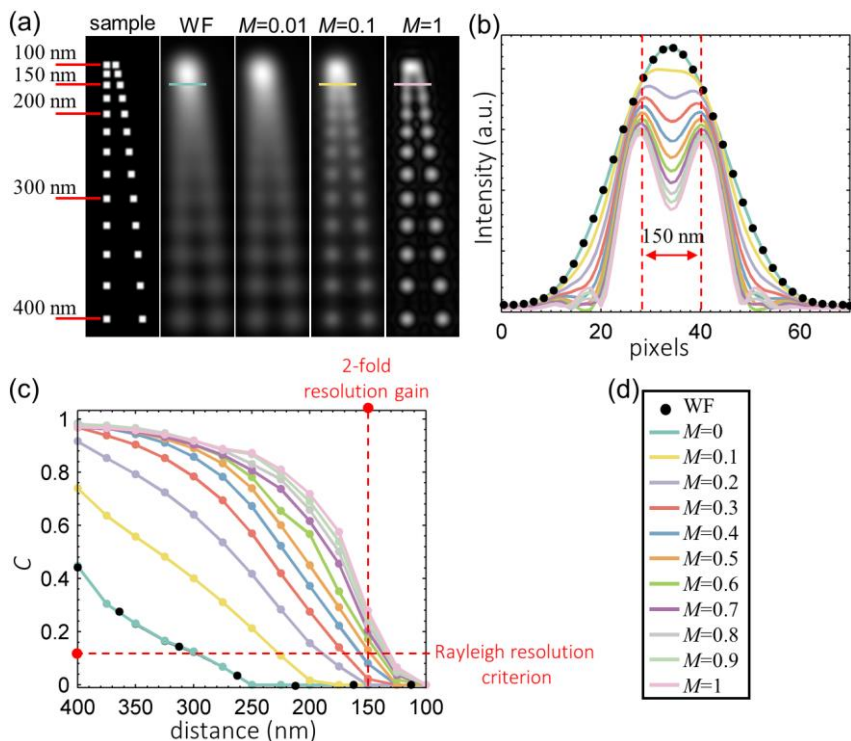
Fig. 5.1 Effects of pattern modulation in the resolution gain of SIM images. **(a)** Simulated sample consisting of pairs of beads separated by distances from 100 to 400 nm, its wide field (WF) and SIM reconstructions under three different pattern modulations, M=0.01, 0.1 and 1. No Gaussian noise was applied to the images. **(b)** Intensity profiles of the WF and SIM reconstructions of the beads separated by 150 nm. **(c)** Contrast vs beads separation distance at different modulation values. The horizontal red dashed line marks the contrast required by the Rayleigh's resolution criteria to consider two objects as resolved. The vertical red dashed line indicates the distance of 150 nm which is the maximum attainable resolution if a two-fold resolution gain is achieved. **(d)** Color code for the curves in (b) and (c).
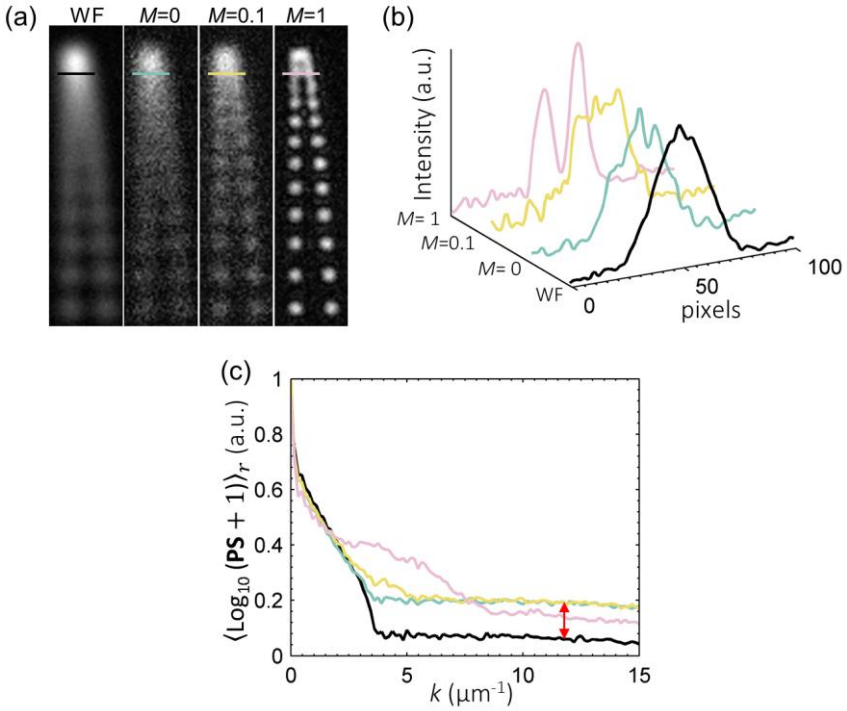
Fig. 5.2 Noise amplification in SIM reconstructions. (a) WF and SIM reconstructions of the sample under illumination patterns of M=0, 0.1 and 1. Gaussian noise of variance 0.1% was added to the SIM raw images. (b) The intensity profiles of the beads separated by 150 nm exhibit the amplification of Gaussian noise in the SIM reconstructions respect to the WF, while the WF curve (black solid line) presents a smooth profile the reconstructions display a more noisy intensity variation. (c) Circular average of the logarithmic power spectra of the WF and the SIM reconstructions. The double headed red arrow shows the vertical separation between the spectra in the regions associated only to noise, this demonstrates the noise amplification in the SIM images.

5.1.2 SIM reconstruction process amplifies the noise variance

Before using the noise variance as baseline to measure the effective modulation we investigated how this is transformed under the SIM reconstruction. We applied to the sample of fig.5.1a Gaussian noise of zero mean at three noise variance (σ^2) conditions: 0.01, 0.05, and 0.1%. Such variance values led to WF images with signal-to-noise ratios (SNR) of 60, 20 and 10 respectively (fig.5.3b). The noise was applied to the SIM raw images (O_{mj}) and then the reconstruction was carried out. The WF and the reconstructions for M=0, 0.1 and 1 can be seen in fig.5.2a (σ^2=0.1%). A visual comparison between the WF image and the reconstruction with M=0 hints to a noise amplification in the latter, since M=0 adds no resolution gain it is expected to look similar as the WF image but notice that the Gaussian noise is higher in the reconstruction despite the fact that both were derived from images with the same noise variance (σ^2=0.1%). Fig.5.2b shows the intensity profile of the beads in the third row, the profiles of the reconstructions with low modulation (M=0, 0.1) seem clearly noisier than the WF data (black line). To make obvious the noise amplification due to the reconstruction we have plotted in fig.5.2c the circular average of the logarithmic power spectrum of the images in fig.5.2a; these curves show that the noise of the SIM reconstructions is always above that of the wide field (red double headed arrow).

To quantify the noise amplification we account for Gaussian noise in eqs.41 and 42 and calculate the ratio between their noise variances. Since Gaussian noise is additive we add the noise spectrum ($\widetilde{N}$) to eqs.41 and 42, thus the noisy domains ($\widetilde{S}^{[N]}$) are expressed as the sum of the signal and noise terms, for the extended domains we have that:

$$\widetilde{S}_j^{\pm[N]} = \widetilde{S}_j^{\pm} + \widetilde{N}_j^{\pm}. \tag{44}$$

and for the central domain:

$$\tilde{\boldsymbol{S}}_j^{o[N]} = \tilde{\boldsymbol{S}}_j^o + \tilde{\boldsymbol{N}}_j^o. \tag{45}$$

To simplify notation in these last equations we have labeled with $\pm$ the signal and noise spectra of the extended domains, i.e. $\tilde{\boldsymbol{S}}_j^{\pm} = \tilde{\boldsymbol{S}}(\vec{k} \pm \vec{p}_{oj})$. Similarly for the central domain but with the symbol o, $\tilde{\boldsymbol{S}}_j^o = \tilde{\boldsymbol{S}}(\vec{k})$. From eqs.41 and 42 the spectra $\tilde{\boldsymbol{N}}_j^{\pm}$ and $\tilde{\boldsymbol{N}}_j^o$ are composed by the individual noise of the images' spectra $\tilde{\boldsymbol{O}}_{mj}$, i.e.:

$$\tilde{\boldsymbol{N}}_j^{\pm} = 0.5\left[\pm e^{\pm\frac{4\pi}{3}i}\left(\tilde{\boldsymbol{N}}_{1j}(\vec{k}) - \tilde{\boldsymbol{N}}_{oj}(\vec{k})\right) \pm e^{\pm\frac{2\pi}{3}i}\left(\tilde{\boldsymbol{N}}_{oj}(\vec{k}) - \tilde{\boldsymbol{N}}_{2j}(\vec{k})\right)\ldots \right.$$
$$\left. \pm \left(\tilde{\boldsymbol{N}}_{2j}(\vec{k}) - \tilde{\boldsymbol{N}}_{1j}(\vec{k})\right)\right] \tag{46}$$

and

$$\tilde{\boldsymbol{N}}_j^o = 0.5^2\left[\left(\tilde{\boldsymbol{N}}_{oj}(\vec{k}) + \tilde{\boldsymbol{N}}_{2j}(\vec{k})\right)\left(e^{\frac{2\pi}{3}i} - e^{-\frac{2\pi}{3}i}\right) + \tilde{\boldsymbol{N}}_{1j}(\vec{k})\left(e^{-\frac{4\pi}{3}i} - e^{\frac{4\pi}{3}i}\right)\right]. \tag{47}$$

The spectra of Gaussian noise is linked to the noise variance by the following relation[74]:

$$\tilde{\boldsymbol{N}}_{mj} \cdot \tilde{\boldsymbol{N}}_{nj}^* = \sigma^2 \delta_{m,n}. \tag{48}$$

Considering that the noise variance is the same for all spectra $\tilde{\boldsymbol{N}}_{mj}$, we use this last relation to calculate the norm of $\tilde{\boldsymbol{N}}_j^{\pm}$ and $\tilde{\boldsymbol{N}}_j^o$ (eqs.46/47) and obtain the ratio of their variances:

$$\frac{\widetilde{\boldsymbol{N}}_j^{\pm} \cdot \widetilde{\boldsymbol{N}}_j^{\pm*}}{\widetilde{\boldsymbol{N}}_j^{o} \cdot \widetilde{\boldsymbol{N}}_j^{o*}} = \frac{\left\|\widetilde{\boldsymbol{N}}_j^{\pm}\right\|^2}{\left\|\widetilde{\boldsymbol{N}}_j^{o}\right\|^2} = \frac{16\sigma^2}{4\sigma^2} = 4, \tag{49}$$

hence the variance of the noise in the extended domains is four times larger than the variance of the wide field.

5.1.3   *Q*-factor: defining a metric of effective pattern modulation in SIM

In sec.5.1.1 we showed that the pattern modulation determines the amplitudes of the extended domains that produce the resolution gain in SIM. The SNR of these domains measure then the relevance of the information content in them, simply because this quantity will yield the strength of the newly acquired spatial frequencies over the noise. To estimate the SNR of the extended domains we divided the image spectrum in two areas, one containing the signal (Σ) and the other containing only noise (v, fig.5.3a). These areas are divided by a radius ρ such that:

$$\rho = \sqrt{k_x^2 + k_y^2} \ | \ OTF(k_x, k_y) = 0.05 \cdot \max(OTF). \tag{50}$$

The SNR of is given then by the ratio between the average spectrum norm in the regions Σ and v:

$$SNR(\tilde{\boldsymbol{S}}_j^{\pm}) = \frac{\langle\|\tilde{\boldsymbol{S}}_j^{\pm}(\vec{k} < \rho)\|\rangle}{\langle\|\tilde{\boldsymbol{S}}_j^{\pm}(\vec{k} \geq \rho)\|\rangle}. \tag{51}$$

and the same for the central domain:

$$SNR(\tilde{S}_j^o) = \frac{\langle\|\tilde{S}_j^o(\vec{k} < \rho)\|\rangle}{\langle\|\tilde{S}_j^o(\vec{k} \geq \rho)\|\rangle}. \tag{52}$$

In fig.5.3b/c the SNR of the extended and central domains of the beads (fig.5.1a) are plotted against the pattern modulation M. The three lines in each plot correspond to the variance conditions: 0.01 (blue), 0.05 (red) and 0.1% (green). The SNR of central domain remains a constant (fig.5.3b) while the SNR of the extended domain behaves linearly respect to the modulation (fig.5.3c), the slope of these lines decreases with an increasing noise variance, meaning that high noise levels hinder the effectiveness of increasing the amplitude of the frequencies in the extended domains. The SNR as calculated in eq.51 does not provide information about the resolution gain achieved in the SIM reconstruction, its values are unbound and they depend on the noise variance, thus an optimal SNR would have to be defined at each noise level when evaluating SIM images. Moreover the SNR of the extended domains alone does not provide the weight of these domains respect to the central one. Therefore in order to use the SNR of the extended domains as a standard metric for SIM image quality we rescale its values respect to the SNR of the central domain, additionally the noise amplitude is taken as lower bound to limit its range from 0 to 1:

$$Q_j^{\pm} = \frac{\langle\|\tilde{S}_j^{\pm}(\vec{k} < \rho)\|\rangle - \langle\|\tilde{S}_j^{\pm}(\vec{k} \geq \rho)\|\rangle}{\langle\|\tilde{S}_j^o(\vec{k} < \rho)\|\rangle + \langle\|\tilde{S}_j^{\pm}(\vec{k} \pm \vec{p}_j \geq \rho)\|\rangle} \tag{53}$$

We define the Q-factor of a set of SIM images $\widetilde{\boldsymbol{O}}_{mj}$ as the average of all $Q_j^{\pm}$. For 2D-SIM six extended domains are obtained for three pattern orientations, accordingly:

$$Q = \frac{1}{6} \sum_{j=1}^{3} (Q_j^+ + Q_j^-).$$ (54)

A practical calculation of eqs.53 and 54 can be found in the MATLAB codes section of this thesis, more specifically in the function named twoSIMrec.m in the code lines 59-69 and 105.

In terms of the SIM acquisition Q can be interpreted as an indirect measure of the effective pattern modulation displayed in the raw images $\widetilde{\boldsymbol{O}}_{mj}$. From an information perspective Q measures the content of relevant spatial information in $\tilde{\boldsymbol{S}}_j^{\pm}$, for instance, since by definition the range of Q is the interval [0,1], a value of $Q=0$ means that no new information can be extracted to provide a resolution gain because the extended domains are only comprised by noise or entangled with it. If relevant high spatial frequencies are to be produced with SIM then high values of Q must be procured. We calculated Q from the noiseless data set (fig.5.1) at its different modulation values $M=0\text{-}1$. A curve of the beads' contrast at three resolution lines, 300, 200 and 150 nm (fig.5.1a), is plotted as function of Q in fig.5.3c. These three resolution values were chosen because they represent hallmarks of the resolution gain, if resolved they represent a lateral resolution gain (rg) of 0, 1.5 and 2. The curve associated to $rg=0$ is used as control since the resolution of the wide field is around 314 nm, $rg=2$ is the standard gain expected from SIM and $rg=1.5$ we consider it as an adequate lower bound for significant resolution gains since such gain is hardly achieved by any image processing or linear fluorescence microscopy method. The curves in fig.5.3c show an ascending trend,

hence higher contrasts are related to increasing Qs, the minimum Q required for resolving the beads is obtained by applying the Rayleigh resolution criteria in the same manner we did in fig.5.1c, namely, finding the argument of $C(Q)$ such that $C=0.12$. To find this value for each of the curves we firstly obtained $C(Q)$ by fitting the corresponding data to a logistic function, (sec.5.3.2), the fitted curves correspond to the black solid lines (fig.5.3c). The arguments that yield $C=0.12$ for the three lines are 0, 0.11 and 0.33, we indexed these arguments as Q_{rg} to associate them with the resolution gain that each of the curves measure, hence $Q_0=0$, $Q_{1.5}=0.11$ and $Q_2=0.33$. The result $Q_0=0$ obtained from the control curve expresses the fact that no modulation is required to access the spatial frequencies that are intrinsically given by the detection objective. The values $Q_{1.5}=0.11$ and $Q_2=0.33$ represent an estimate of the minimum values that a SIM data set should present to achieve a resolution gain of 1.5 and 2 respectively, when the illumination pattern is tuned to attain a maximum gain of 2. Either $Q_{1.5}$ or Q_2, depending on how stringent one wishes to be, mark the threshold that divides optimal from sub-optimal data. The existence of these values is equivalent to the result of the minimum modulation required to attain a resolution gain (sec.5.1.1). The question now is if the same values can be used to evaluate data acquired under different SNR conditions. We plotted in figs.5.4a/b/c the $C(Q)$ curves of the three resolution lines (300, 200 and 150 nm) of the data sets with the three different noise variances, 0.01 (blue), 0.05 (red) and 0.1% (green) and compared them to the fitted curve of the noiseless data set (black). The trajectories of the colored curves initially run parallel to that of the noiseless data and diverge from it as Q increases, this occurs because the largest available contrast is limited by the noise variance. If we take into account the error bars of the colored curves, their proximity to the contrast values given by the black curve around $Q_{1.5}$ and Q_2 should allow the use of $Q_{1.5}=0.11$ and $Q_2=0.33$ as adequate estimates for dividing optimal and sub-optimal SIM data under different SNR conditions. The insets in figs.5.4b and 5.4g illustrate the

SIM reconstructions of the beads, any SIM data set with $Q > Q_{rg}$ carries enough information to produce reconstructions with a resolution gain rg or larger while a set with $Q < Q_{rg}$ does not.
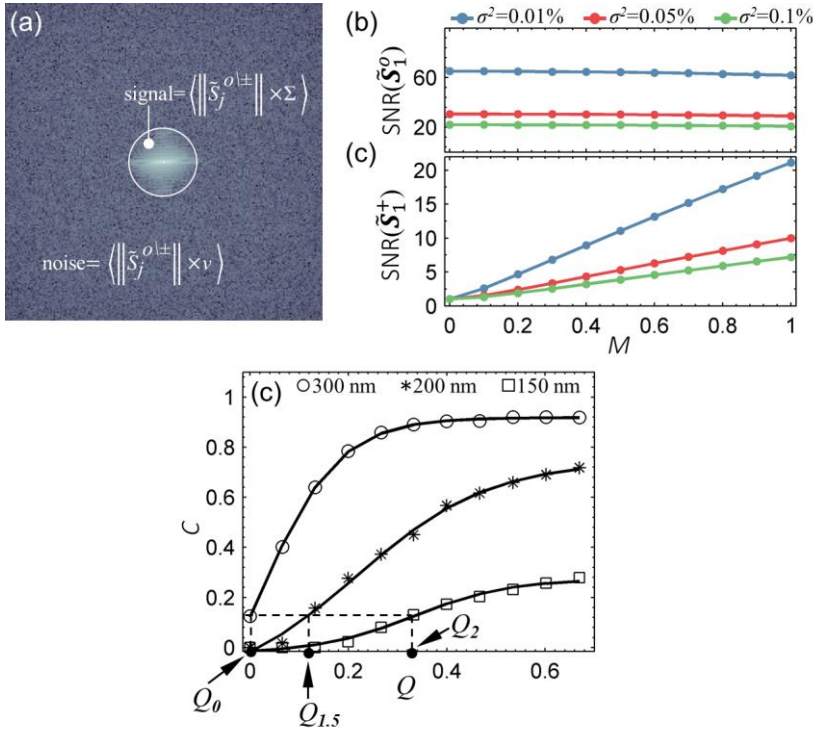
Fig. 5.3 Q-factor as measurement of resolution gain attainability in SIM. (a) Scheme of the extraction of the signal and noise average amplitude from the central and extended domains. The cut-off frequency of the OTF outlined by the white circle. The regions Σ and v correspond to the areas within and out of the OTF respectively. **(b)** SNR of the central domain and **(c)** SNR of the extended domain against pattern modulation. SNR was calculated from the simulated sample in fig.5.1 under three different noise variances, 0.01 (blue), 0.05 (red) and 0.1% (green). **(d)** Contrast vs Q curves for the beads separated at 300, 200 and 150 nm. The latter curves were obtained using the noiseless data set. The minimum Q values required to obtain resolution gains of 0, 1.5 and 2 are accordingly marked on the horizontal axis at 0, 0.11 and 0.33. The solid lines are the curves fitted with eq.58 to the data points ($\circ$,*,$\square$).
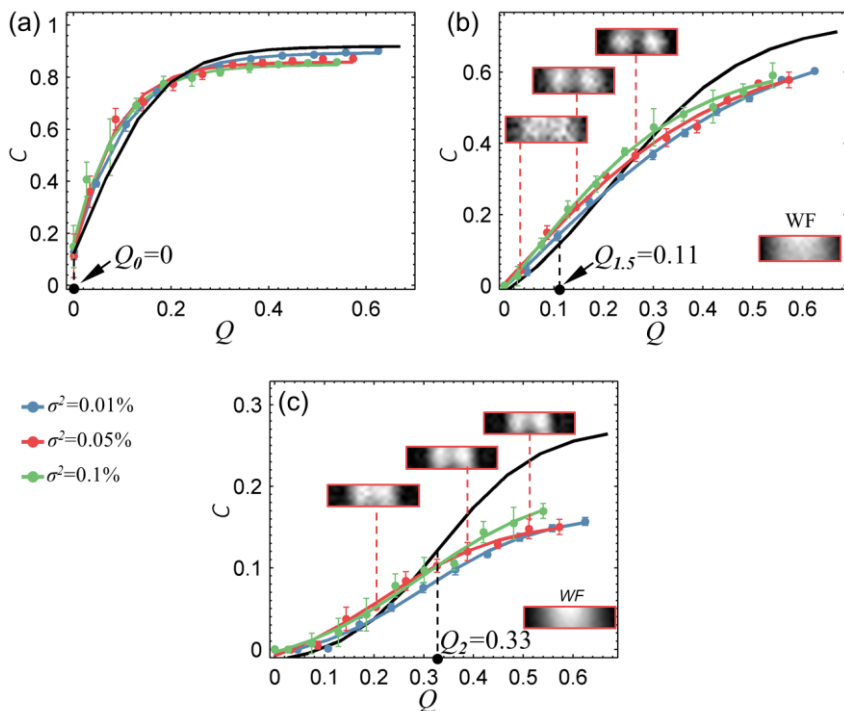
Fig. 5.4 Q-factor under different SNR values. Contrast vs Q curves calculated from the noiseless (black) and noisy data sets, σ^2=0.01, 0.05 and 0.1% (blue, red, green). The curves are plotted for the for the beads separated by **(a)** 300 nm, **(b)** 200 nm and **(c)** 150 nm. The rectangular insets in (b) and (c) show the WF and three SIM reconstructions of the corresponding beads pair (σ^2=0.05%). One reconstruction is carried with a sub-optimal data set, i.e. $Q < Q_{rg}$, and the other two with optimal Qs ($Q > Q_{rg}$).

5.2 Results

5.2.1 Implementation of Q in 2D-SIM and 3D-SIM data

In 2D-SIM the extended domains obtained per orientation are $\tilde{S}(\vec{k} + \vec{p}_{oj})$ and $\tilde{S}(\vec{k} - \vec{p}_{oj})$ (eq.17). In the case of 3D-SIM four extended domains per orientation are extracted from the raw data: $\tilde{S}(\vec{k} + 0.5\vec{p}_{oj})$, $\tilde{S}(\vec{k} - 0.5\vec{p}_{oj})$, $\tilde{S}(\vec{k} + \vec{p}_{oj})$ and $\tilde{S}(\vec{k} - \vec{p}_{oj})$ (eq.21), the first two are related to a 1.5 lateral resolution gain. The last two are equivalent to the domains obtained in 2D-SIM, in the sense that they carry the frequencies needed for a 2-fold lateral resolution gain, therefore we use only those two domains to calculate Q in 3D-SIM data through eqs.53 and 54. If a 3D stack is acquired Q can be calculated for each plane, yet to have an estimate of the maximum Q that can occur in the stack it is only necessary to make the calculation for the central plane since it usually contains more in-focus features. If Q is calculated from the first or last planes, where the signal is mostly out-of-focus, Q will be very close to zero because the pattern has been blurred (fig.5.11).

Calculating Q does not require prior knowledge of the reconstruction parameters, i.e. pattern's phases, periods and orientations, it only requires the raw images as input. Hence, Q provides a pre-reconstruction criterion of the raw data quality on which a decision can be based to adequately proceed with sub-optimal data. In the following sections we demonstrate practical implementations on how to evaluate sub-optimal data through Q and how to use it as guideline to optimize the acquisition parameters, such as pattern period, exposure time and laser power to increase the data quality. The assessment strategy is carried out by considering the value $Q_{1.5}=0.11$ as the borderline between optimal and sub-optimal data quality.

5.2.2   *Q* as guideline to optimize pattern modulation

Fig.5.5a shows two SIM reconstructions of a DAPI stained nucleus. The raw images were acquired with a pattern period of 183 nm (left) and 222 nm (right), they correspond to an expected resolution gain of 1.9 and 1.7 respectively. The laser power for both acquisitions was maintained constant to achieve similar SNR in both data sets. A visual inspection of the reconstructions will immediately conclude that the image on the right panel displays a better contrast than the one on the left. This is inconsistent if we evaluate the images based on their expected resolution gains, but it is completely congruent if we compare the *Q* values of the data sets. While the image with expected *rg* of 1.9 has a *Q* of 0.08, the one with *rg*=1.7 presents a *Q* of 0.12. The raw images of the former reconstruction are sub-optimal according to the threshold value of $Q_{1.5}$=0.11, thus no significant resolution gain can be expected. The sub-optimal acquisition is due to the low modulation of the 183 nm pattern period in comparison with the 222 nm pattern, fig.5.5c shows the intensity profile of lines perpendicular to the illumination pattern in an excerpt of the raw images (fig.5.5b), the peaks and valleys of the 222 nm pattern (red) are clearly more noticeable than those of the 183 nm pattern (blue). By increasing the pattern period from 183 nm to 222 nm we have increased the pattern modulation and so strengthen the high spatial frequencies contained in the data sets to produce a better reconstruction. This illustrates the impracticality of aiming at high resolution gains without fulfilling the minimum modulation conditions, although increasing the pattern period has decreased the expected maximum resolution gain, the increase in modulation has also enhanced the amplitudes of the extended domains leading to an effective resolution improvement. To demonstrate the resolution gain of these reconstructions we compared the intensity profile of a feature in the WF against its profile in the two reconstructions (fig.5.5a, left corner insets). The profile of the structure in the WF (green curve) shows two peaks that present higher contrast in the reconstruction

with Q=0.12 (white line) while in the case of the sub-optimal reconstruction the peaks have lost their profile (yellow line, Q=0.08). The latter curve is very noisy due to the little strength of the high spatial frequencies and the amplification of the noise variance, both effects combine to produce a reconstruction that does not attain a significant resolution gain and deteriorates the original information with amplified noise.

The analyzed nucleus images have a moderate SNR of 8; images with higher SNR do not guarantee resolution improvement if the pattern modulation is extremely low[39]. A high quality reconstruction requires also high pattern modulations. An instance of this is illustrated with the mitochondria data set in fig.5.5d, the figure shows the WF (left panel) and two SIM reconstructions, corresponding to acquisitions with low (central panel) and high pattern modulations (right panel). The raw images have a high SNR of 21; the low modulation acquisition was achieved by deliberately illuminating the sample with a pattern period of 173 nm, which 0.66 times smaller than the resolution of the detection objective (sec.5.3.3). Accordingly, the data set has a low Q value of *0.03* and the reconstruction presents periodic artifacts due to a complete lack of mid-range frequencies (sec.4.1.2), effect that becomes evident in the power spectrum of the reconstruction (inset in fig.5.5d/center, white arrows). The low Q factor is a reflection of that frequency shortage but it is possible to provide the extended domains $\tilde{\boldsymbol{S}}(\vec{k} - \vec{p}_{oj})$ with a larger weight by increasing the pattern modulation in a second acquisition, e.g. the data set acquired with a period of 221 nm (fig.5.5d/right). This data has now a Q value of *0.17* which overcomes the $Q_{1.5}$ threshold, thus the data set is considered optimal for obtaining a significant resolution gain; a higher Q also means that the amplitudes of the high spatial frequencies are now larger, hence the power spectrum of this reconstruction displays a continuous profile (inset top right corner) which in return eliminates the

periodic artifacts arising from an irregular spectrum, like the one in the reconstruction acquired with the 173 nm pattern.

In conclusion, comparing the Q value of a SIM image set with the threshold values $Q_{1.5}$ provides a numerical guideline to diagnose sub-optimal data due to low pattern modulation. Shifting sub-optimal data to an optimal status can be done by re-acquisition of the data with an increased pattern modulation, this can be easily achieved in practice by changing the illumination grid to increase the pattern period; alternatively illumination modes that enhance the modulation of the pattern can be implemented, such as the line scan in linear SIM or patterned activation/excitation in non-linear SIM[75,76].
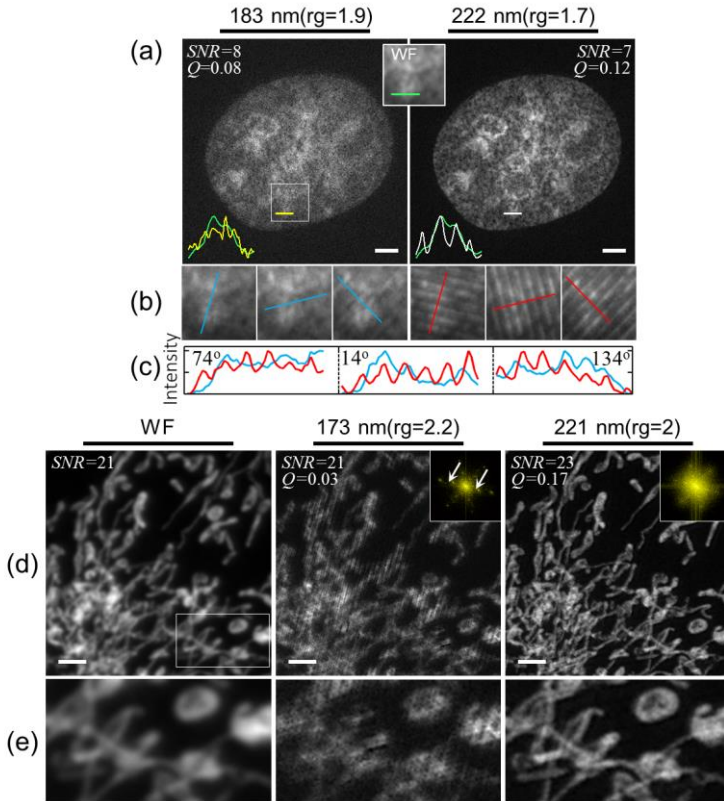
Fig.5.5 Optimization of pattern modulation by adjusting pattern period. **(a)** SIM reconstructions of a cell nucleus stained with DAPI. Raw data was acquired under two different pattern periods, 183 nm (left panel) and 222 nm (right panel), the expected maximum resolution gains are 1.9 and 1.7 respectively. The average SNR of the WF image and the Q value of the SIM data set is shown in reconstructions. The WF of the region within the white box has been magnified in the central panel. A feature of that region has been selected and its intensity profile plotted for its WF image (green) and SIM reconstructions (yellow, white), the curves are compared against each other in the bottom left corner. **(b)** Raw images of the white box area under the sinusoidal illumination pattern, the first phase of each pattern orientation is shown. Orientation angles are 74º, 14º and 134º. **(c)** Intensity profiles of the illumination patterns at the lines indicated in figure (b), pattern period of 183 nm in blue and 222 nm in red. **(d)** Images of mitochondria stained with MitoTracker, Left: wide field, Center: SIM reconstruction (173 nm pattern period), Right: SIM reconstruction (221 nm pattern period). The power spectrum of each reconstruction is shown in the top left corner of the image. **(e)** Magnifications of the white outlined box in (d). Scale bar: 2 μm.

5.2.3   *Q* as guideline to optimize laser power and exposure time

As shown in the previous section, a low modulation can be corrected by increasing the pattern period. Likewise, laser power and exposure time can be tuned to increase SNR using *Q* as guideline. Fig.5.6b shows the WF image of actin filaments, its corresponding SIM reconstructions with data sets acquired at different laser powers and exposure times are presented in fig.5.6a. Three different exposure times, 10, 50 and 100 ms, and two illumination powers, 20 and 40%, were used. The overlay of figs.5.6a is used in fig.5.6c to make a color map of the *Q* values of each data set, the color association is red for $Q < Q_{1.5}$, yellow for $Q=Q_{1.5}$ and green for $Q > Q_{1.5}$. The *Q* values in the color map help to identify optimal acquisition conditions, for instance, in the actin sample only one pair of acquisition conditions produced optimal data, namely 40% of laser power and 100 ms of exposure time, which yielded a *Q* of 0.13 (fig.5.6c). Another example of this optimization is illustrated in the mitochondria sample of fig.5.7b. Fig.5.7a shows the SIM reconstructions of this sample at three exposure times (1, 5 and 10 ms) and three laser powers (10, 20 and 40%). The color map of the *Q* values indicates that any power $\geq 20\%$ and exposure time $>$ 5 ms will provide *Qs* larger than $Q_{1.5}$, acquisition of images using the lower bounds 20% and 5 ms will jointly minimize power and exposure time while keeping the raw data optimal (fig.5.5c). Minimizing power and/or exposure time is important in live imaging to maintain sample integrity and obtain fast acquisition speeds, *Q* helps to minimize those parameters while tracking if the information content in the raw data is still sufficient to yield a resolution gain.

It is clear that to acquire multiple data sets under different power and exposure conditions requires several acquisitions that might produce photodamage, to avoid this the optimization strategy can be implemented only on a small area of the whole field of view. Besides, the standardization of fluorescent labeling protocols within a lab means that a

sample could be used to obtain the minimum required conditions of power and exposure time through Q and later apply these same parameters for the following samples.

One last thing to draw attention to in the reconstructions of fig.5.6a is that they represent a remarkable visualization of the role of $Q_{1.5}$ as the threshold between sub-optimal and optimal data, certainly only after the data sets obtain a $Q=0.11$ the reconstructions commenced to display a resolution gain respect to the WF whereas the sets with lower Qs did not accomplish this (figs.5.6a/c).
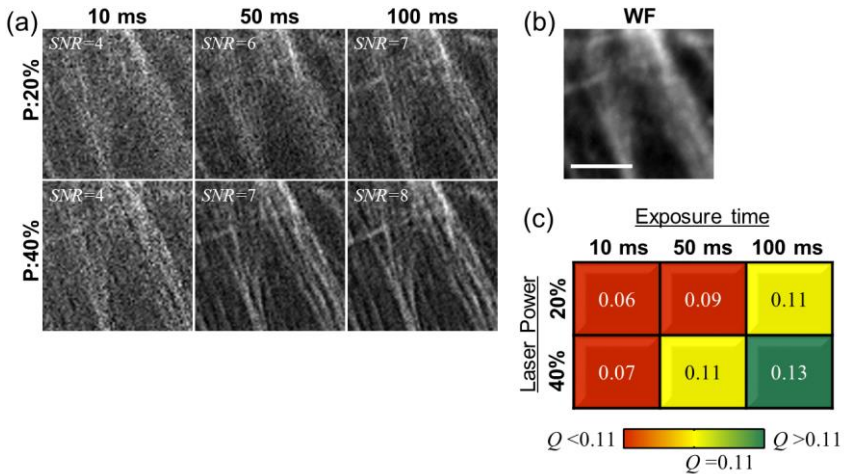
Fig. 5.6 Optimization of laser power and exposure time in actin sample. **(a)** SIM reconstructions of an actin sample under laser powers of 20 and 40% and exposure times of 10, 50 and 100 ms. The excitation wavelength is 488 nm and the pattern period is 183 nm. **(b)** Wide field. **(c)** Color map of the Q values of the data sets used in (a), colors indicate sub-optimal (red), fair (yellow) and optimal data sets (green). Scale bar: 2 μm.
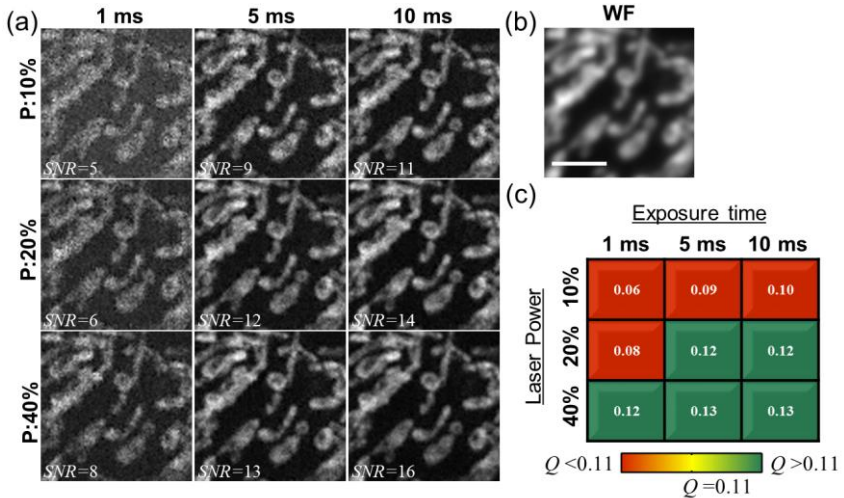
Fig. 5.7 Optimization of laser power and exposure time in mitochondria sample.
(a) Reconstructions of the mitochondria sample under laser powers of 10, 20 and 40%
and exposure times of 1, 5 and 10 ms. The excitation wavelength is 560 nm and the
pattern period is 221 nm. **(b)** Wide field. **(c)** Color map of the Q values of the data sets
used in (a), colors indicate sub-optimal (red), fair (yellow) and optimal data sets
(green). Scale bar: 2 μm.

5.2.4   Assessing fluorophore brightness suitability for SIM

As we demonstrated in the previous two sections laser power, exposure
time and pattern period are acquisition parameters that can be tuned to
increase the value of Q. These are set-up related parameters that affect the
extraction of spatial information with SIM. There are also sample related
parameters like the fluorophore brightness or the packing density of the
observed structure that play a role in the withdrawal of high spatial
frequencies from the raw data. For instance, if the brightness delivered by
the fluorophore is not high enough due to a low quantum yield, the
responsiveness of the sample to the tuning of acquisition parameters is
extremely hindered. Such case is shown in fig.5.8, a DAPI stained nucleus

has been reconstructed with an image set at 10% laser power (fig.5.8c/left) and another at 40% (fig.5.8c/right), the gain in the SNR of the raw data is not significant, going from SNR=2 to SNR=3. The dye in this case has a low quantum yield, hence producing low SNRs. Increasing the pattern period from 183 to 222 nm (fig.5.8c/f) to improve the modulation does not carry a major improvement because the modulation is limited by the low SNR. This is reflected in the low Q values of the images, the maximum Q obtained for this sample was Q=0.08 (fig.5.8f right), which does not overcomes the threshold $Q_{1.5}$ and consequently no resolution gain can be expected. Additionally, due to the low SNR the noise amplification in the reconstructions becomes very noticeable, fig.5.8b shows the surface plot of the region within the red box (fig.5.8a WF), the same plot of any of the SIM reconstructions (fig.5.8d/e/g/h) is very spiky in comparison to the smooth profile of the wide field (fig.5.8b). The studied case illustrates the application of the Q factor to diagnose problems in the raw data due to a low brightness of the fluorophore, in such samples tuning of illumination pattern, laser power or exposure time will not turn gainful in increasing the quality of the raw data and it would indicate that an enhanced fluorophore should be applied in a reacquisition.

5.2.5   Assessing suitability of sample structure for SIM

The structure of a sample can affect the effective pattern modulation displayed in the raw images. For instance, given a pattern period, a discrete structure will inherently displayed a higher pattern modulation than a "continuous" one, because in the former the point spread functions across the image will have less overlap than in the latter. To depict these conditions we imaged with the csiLSFM (chapter 3) the Lamin A structure of a HeLa cell sprinkled with 100 nm fluorescent beads. Lamina A is a fibrous structure while beads represent a discrete fluorescent unit (figs.5.9a/b). We illuminated the sample with a pattern of 200 nm in period, i.e. 0.6 times smaller than the Rayleigh resolution limit, hence the

modulation is expected to be sub-optimal. Fig.5.9a shows the WF and the SIM raw data of the three phases of the first pattern orientation, φ_o, φ_1 and φ_2, the low modulation of the pattern is certainly reflected in the low Q value of the data ($Q=0.02$). A red rectangle in the WF image encloses a region with a bead close to the cell, the magnifications of this region in fig.5.9b demonstrate that the bead blinks when the phase of the pattern is shifted (white arrow), whereas the intensity modulation in the Lamin A is barely perceptible. Fig.5.9c shows the intensity profiles of the images along the white dashed line (fig.5.9b WF), a visible intensity bump owed to the bead blinking occurs in phase φ_1 (red curve) but the profile corresponding to the Lamin A area remains basically the same in any of the phases, so even if the pattern produces a low intensity modulation in the cell structure it is able to produce a high modulation of the bead because it fits in between the dark and bright fringes of the pattern. This demonstrates that the effective pattern modulation displayed in the raw images does not only depend on the inherent modulation of the illumination pattern but also on the size and packing density of the imaged structure. In the data set of fig.5.9a the reconstruction attempts were unfruitful due to the low information contained in the images ($Q=0.02$). Successful reconstructions were attained in discrete structures at even smaller patterns, like the fluorescent beads and α–tubulin of fig.5.9d and fig.5.9e. Both samples were illuminated under a pattern of 183 nm and yet good SIM reconstructions were obtained. The success of these reconstructions is due to the discrete spatial distribution of the samples that enhance the modulation displayed by pattern, this is evident in the large Q values of both samples ($Q=0.33$ and $Q=0.16$).

Packed structured and patterns with periods below the resolution limit of the objective lens are usually not compatible because of the low modulation displayed in the images. Such fine patterns are not only applied in the csiLSFM but also in TIRF-SIM or non-linear SIM, assessing

if a fluorescently labeled structure is adequate for any of these SIM modalities can be also done through the calculation of Q.
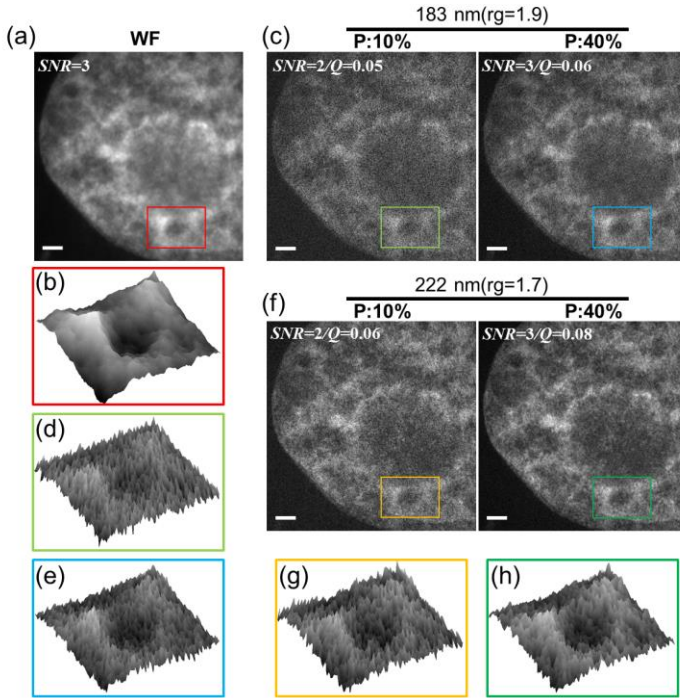
Fig. 5.8 Q-factor to assess the suitability of fluorophore brightness for SIM. **(a)** Wide field of a cell nucleus. **(c/f)** SIM reconstructions under a pattern period of 183/222 nm and two illumination powers, 10 and 40 %. The SNR and Q of the data sets appear in the images. The fluorophore has little responsiveness to changes of modulation or laser power and so it is reflected in the modest increase of the Q factor. Also the small change of SNR with increasing laser powers hints to a low quantum yield of the fluorophore. **(b/d/e/g/h)** Surface plots of the rectangular area outlined in the WF and the SIM reconstructions. The spiky profile of the surface plots corresponding to the reconstructions exhibit the noise amplification respect to the WF. Scale bar: 2 μm.
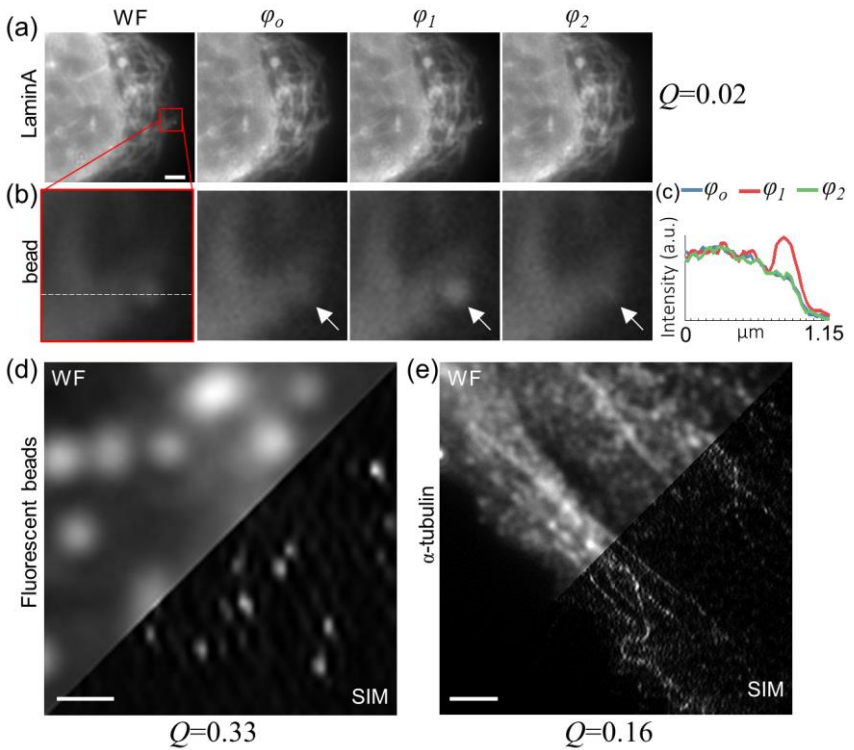
Fig. 5.9 Q-factor to assess the suitability of sample structure for SIM. **(a)** WF of Lamin A in a cell illuminated with a pattern period 1.3 times smaller than the resolution of the detection objective. The SIM raw images taken for the first pattern orientation at phases φ_o, φ_1 and φ_2 are also shown. **(b)** Magnifications of a 100 nm fluorescent bead near the cell. The position of the bead is indicated by a white arrow. **(c)** Intensity profile of the raw images along the white dashed line in (b, WF) at phases φ_o, φ_1 and φ_2. **(d)** WF and SIM reconstruction of fluorescent beads and **(e)** α-tubulin. Scale bar: 2 μm/(d) 500 nm.

5.2.6 Testing *Q* to evaluate SIM raw images acquired with commercial set-ups

We tested the *Q*-factor with images acquired in three SIM commercial set-ups, Elyra (Zeiss), OMX (Delta Vision) and N-SIM (Nikon). The reconstructions appearing in figs.5.5 to 5.8 were acquired with the Elyra system, therefore the application of *Q* in this system is already demonstrated there.

The Nikon microscope provides an interesting experiment to test the underperformance of sub-optimal SIM data. This system is equipped with a confocal and SIM acquisition, fig.5.10a shows the confocal image of actin bundles and three SIM reconstructions at three different exposure times (10, 50 and 100 ms), the SNR and *Q* of each data set is displayed above each image. Only the reconstructions with optimal data (*Q*=0.18/*Q*=0.23, fig.5.10c/d) reveal structures of the sample in more detail than that conveyed by the confocal image. On the other hand, notice that the reconstruction with sub-optimal data (*Q*=0.07,fig.5.10b) does not exhibit a significant gain in contrast nor resolution respect to the confocal image. This example shows that SIM data acquired with inadequate parameters leads to underperformance of SIM. Thus to demand that SIM outperforms standard diffraction limited microscopes one has to assure that optimal data sets have been acquired.

Finally, in fig.5.11 we illustrate with the OMX system how to evaluate with *Q* a 3D stack. In this case it is only necessary to calculate the *Q* factor in a middle plane since this assures that the highest pattern modulation will be probed. Calculation of *Q* in planes that contain plenty of out-of-focus features will not yield representative results of the best acquisition conditions since *Q* decays in these planes due to the low pattern modulation.
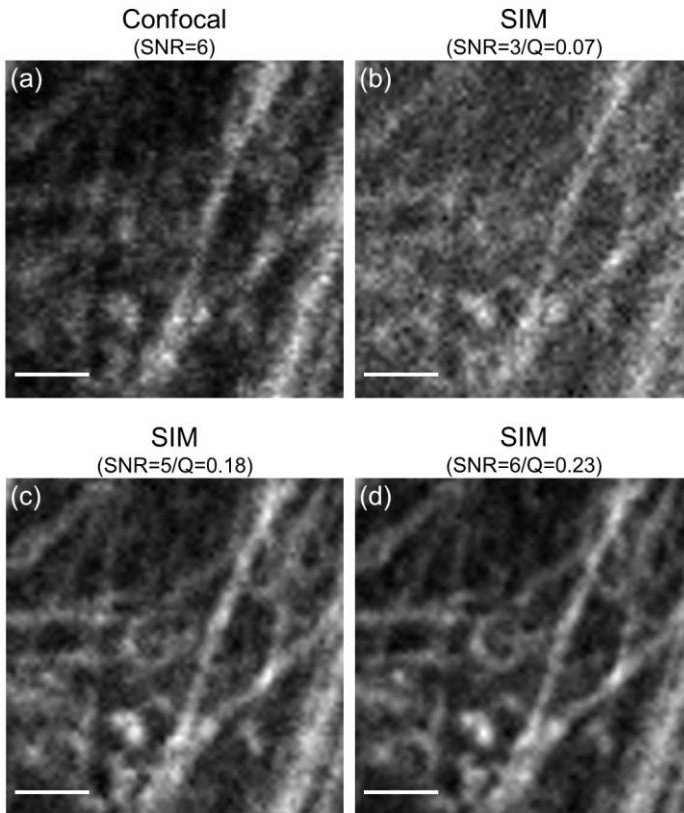
Fig.5.10 Underperformance of SIM set-ups owed to sub-optimal data. **(a)** Confocal image with a pixel dwell time of 100 ms. **(b/c/d)** SIM reconstructions acquired with exposure times of 10, 50 and 100ms. Only the data sets with an optimal Q, i.e. Q>0.1, display a resolution gain respect to the confocal image. The sub-optimal data (Q=0.07) does not show this improvement. Scale bar: 1 μm.
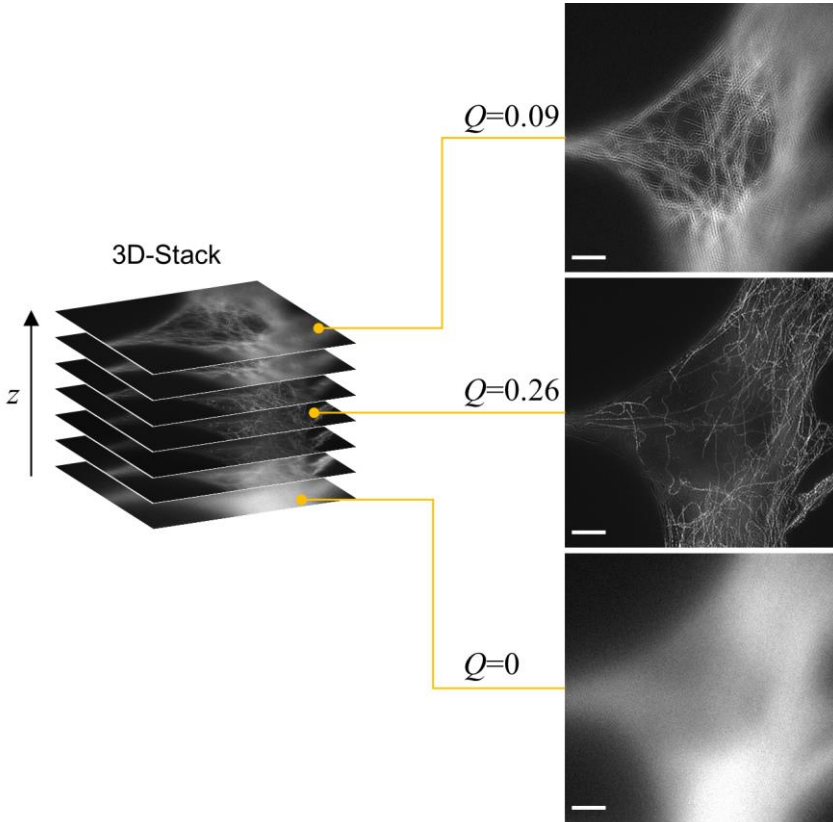
Fig.5.11 Q in 3D stacks. The pattern modulation in the outer planes of an image stack is low because they contain plenty of out-of-focus features. Consequently the value of Q in this planes is very low. To evaluate the quality of the pattern in a stack it suffices with the calculation of Q in a middle plane. Scale bar: 5 µm.

5.3   Materials and methods

5.3.1   2D-SIM simulations on beads

We created a synthetic 2D sample consisting of 13 pairs of beads arranged in rows (fig.5.1a). Each bead has a size of 3x3 pixels. The centers of the first pair of beads are separated by 4 pixels, this distance increases 1 pixel at each row up to a separation of 16 pixels in the last one. The pixel size was set to 25 nm, thus the minimum and maximum separations are 100 and 400 nm. We simulated 2D-SIM illumination on this sample, under the following conditions: λ_{em}=515 nm emission, wavelength, this wavelength was chosen since it is close to the emission of fluorophores excited with 488 nm.   A detection objective with NA=1 and 257.5 nm period of illumination pattern (T_o). This period was calculated to provide the SIM reconstructions with a maximum resolution gain of 2 (eq.33). The wide field resolution is $0.61\lambda_{em}$/NA=309 nm.   The three standard pattern orientations for SIM were applied: 0°, 60° and 120°. The intensity profile of the 2D sinusoidal pattern with phase m and orientation j is given below in eq.55, the pattern phases φ_m were defined as given by eq.16, lastly the pattern modulation (M) is given by the ratio of the constants B and A (eq.56).

$$I_{mj}(\hat{r}) = A + Bcos(\hat{r} \cdot \vec{p}_{oj} + \varphi_m).$$

$$\text{(55)}$$

$$M = \frac{B}{A}, B \leq A. \qquad \text{(56)}$$

We performed the simulations with modulation values from 0 to 1 in steps of 0.1 (M). Hence obtaining 11 data sets of the same sample with different modulations. Besides the noiseless data set used for fig.5.1 we also created sets with three different noise variance conditions (fig.5.2/5.3).   The

applied noise was Gaussian with zero mean and variances of $\sigma^2 = 0.01$, 0.05, and 0.1%. Such variance values lead to images with SNRs of 60, 20 and 10 respectively (fig.5.3b).

5.3.2 Curve fitting

Intensity profiles $I(x)$ of the pairs of beads were fitted to a sum of two Gaussian curves using non-linear regression and six fitting parameters a_1, a_2, b_1, b_2, d_1 and d_2 (eq.57). The contrast (C) used in figs.5.1c, 5.3c and 5.4 was calculated with eq.43 applied to the fitted curve $I(x)$.

$$I(x) = a_1 \exp\left(-\frac{(x-b_1)^2}{d_1^2}\right) + a_2 \exp\left(-\frac{(x-b_2)^2}{d_2^2}\right). \tag{57}$$

The points in the C vs Q curves in figs.5.3c and 5.4 were fitted to the logistic function in eq.58 using non-linear regression and four fitting parameters a_1, a_2, α and β.

$$C(Q) = \frac{a_1}{1 + \exp(-\frac{(Q-\beta)}{\alpha})} + a_2. \tag{58}$$

The parameter values for the fitted $C(Q)$ curves plotted in figs.5.3 and 5.4 are shown in tables 5.1-5.3. For each of the resolution lines 300, 200 and 150 nm the corresponding values Q_0, $Q_{1.5}$ and Q_2 have been highlighted in the grey cell. This value is calculated from the inverse function $Q(C)$ evaluated at $C=0.12$ (sec.5.1.3).

Noise variance (σ^2)	a_1	a_2	β	α	$Q(C=0.12)$
Noiseless	1.46	-0.54	0.02	0.08	0
0.01	4.55	-3.66	-0.15	0.10	0
0.05	7.23	-6.37	-0.17	0.08	0
0.1	6.30	-5.45	-0.17	0.08	0

Table 5.1 Values of the fitted parameters in function $C(Q)$ for the 300 nm resolution line.

Noise variance (σ^2)	a_1	a_2	β	α	$Q(C=0.12)$
Noiseless	0.92	-0.17	0.22	0.14	0.11
0.01	1.10	-0.45	0.07	0.16	0.08
0.05	1.30	-0.65	0.00	0.17	0.06
0.1	1.38	-0.72	-0.02	0.17	0.06

Table 5.2 Values of the fitted parameters in function $C(Q)$ for the 200 nm resolution line.

Noise variance (σ^2)	a_1	a_2	β	α	$Q(C=0.12)$
Noiseless	0.30	-0.02	0.33	0.10	0.33
0.01	0.25	-0.03	0.23	0.09	0.27
0.05	0.26	-0.03	0.20	0.09	0.23
0.1	0.28	-0.03	0.24	0.10	0.25

Table 5.3 Values of the fitted parameters in function $C(Q)$ for the 150 nm resolution line.

5.3.3 Samples

Bovine Pulmonary Artery Endothelial Cells (BPAE): Prepared slide with BPAE cells stained with MitoTracker RED CMXRos, Alexa Fluor 488 Phalloidin and DAPI. Invitrogen Fluo Cells Probe F36924 (figs.5.5 to 5.8).

<u>HeLa Kyoto cells</u>: Immuno-stained with Anti-Lamin A & Alexa Fluor 488 (fig.5.9a).

<u>100 nm fluorescent beads</u>: (505/515) (blue) Invitrogen TetraSpeck (fig.5.9d).

<u>Human umbilical vein endothelial cell (HUVEC)</u>: Immuno-stained with α-tubulin & Alexa Fluor 488 (fig.4e).

5.3.4   Microscopes
3D-SIM microscopy: The data sets for the reconstructions in figs.5.5 to 5.8 were acquired with the Zeiss Elyra PS. 1. The excitation lines were 405 nm (50 mW), 488 nm (100 mW) and 561 nm (100 mW). The detection objective was a Plan-Apochromat NA 1.4 63X Oil immersion. N-SIM from Nikon was used for the confocal and SIM acquisition in fig.5.10, the detection objective was NA 1.49 100X oil immersion.   The data for fig.5.11 was acquired with an OMX system (DeltaVision). The detection objective was a NA 1.49 100X oil immersion. Both acquisitions N-SIM and OMX were carried with a 488 nm excitation line.

2D-SIM microscopy: Data for figs.5.9 was acquired with the csiLSFM using an excitation line of 488 nm. Illumination and detection objectives were three Plan-Apochromat NA 1.0 63X Water immersion (chapter 3).

5.3.5   SIM image reconstruction
The 2D- and 3D-SIM reconstructions were carried using only eq.25. No filtering, deconvolution or enhancement was applied to the raw images nor to the reconstructions except for the images acquired with the csiLSFM which required a deconvolution prior to reconstruction to avoid artifacts (figs.5.9d/e).
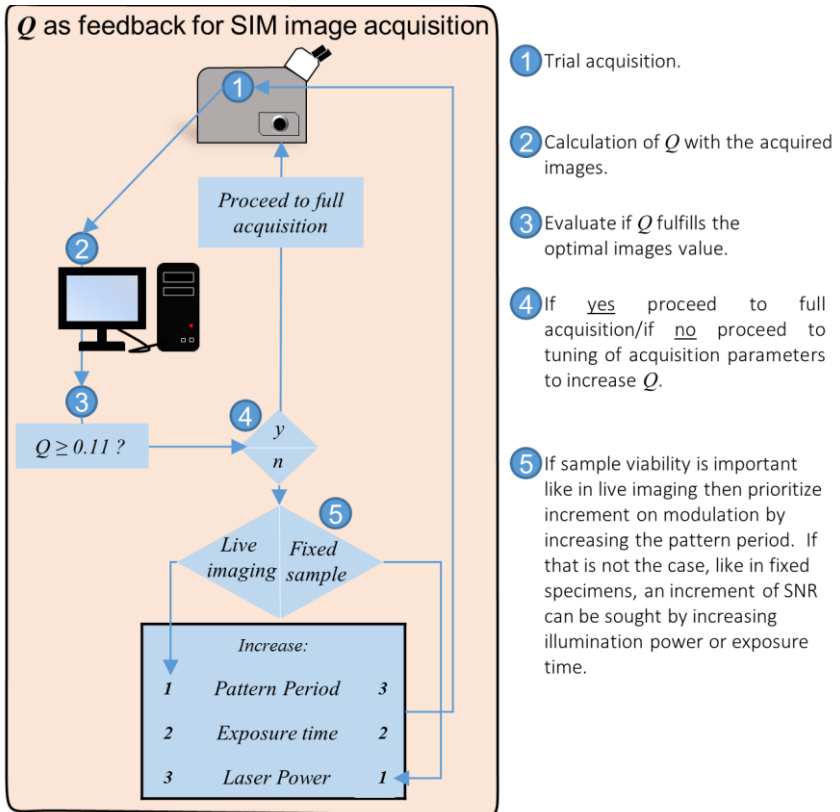
Fig.5.12 Scheme of Q as feedback for acquisition of optimal SIM data sets.

5.4 Discussion

In SIM the period of the illumination pattern determines the maximum attainable resolution gain (sec.2.7), in this chapter we showed through simulations that that this maximum gain is only achieved if the pattern modulation overcomes certain minimum value, only then a significant resolution gain respect to Abbe's limit can be expected (sec.5.1.1). The

amplitude of the high spatial frequencies in the extended domains are directly dependent on the modulation, hence to produce relevant information during the acquisition of the raw data one must guarantee that the intensity changes due to the pattern modulation are higher than those of the noise variance. Based on this, we have introduced the normalized metric Q to indirectly measure the intensity modulation from the raw data (sec.5.1.3). Q yields the strength of the high spatial frequencies respect to the variance of the Gaussian noise. We estimated that a SIM data set requires $Q \geq 0.11$ to generate significant resolution gains, more specifically when using a pattern period from which a maximum resolution gain of 2 is expected, $Q=0.11$ will convey a resolution gain of 1.5 while a value of $Q=0.33$ will deliver the full 2-fold resolution gain. The value $Q=0$ implies that no relevant information was extracted from the SIM acquisition because the modulation produced was entangled with the noise.

The values $Q=0.11$ and 0.33 represent a rough estimate and more rigorous estimations could be carried with a probabilistic analysis but they are certainly not arbitrary because although the spectra of an image depends on the sample, its frequencies are distributed according to the OTF profile[77]. By considering $Q=0.11$ as the boundary between sub-optimal and optimal SIM data we developed three practical applications using this value as guideline: 1) Detection of sub-optimal data, i.e. any data set with $Q<0.11$ does not contain enough new spatial frequencies to increase the resolution, therefore the data is deemed as sub-optimal (fig.5.5). 2) As benchmark for optimization, e.g. in case fast acquisition or reduced photo-damage is required during acquisition, minimization of exposure time or laser power can be carried out taking $Q=0.11$ as lower bound (fig.5.6/5.7). 3) As general acquisition feedback, e.g. tuning acquisition parameters by aiming at higher Qs to improve the data quality in a reacquisition; fig.5.12 illustrates a scheme of such application.

In the SIM reconstructions presented in this chapter we avoided the filtering and enhancement of the reconstructed spectrum. While the majority of publications treating the SIM reconstruction algorithm discuss the quality of the final image in terms of these processing steps, Q allows centering the discussion in terms of the quality of the raw data, quality that is measured in terms of information content. To extend the link between Q and information we refer to the papers by Mendlovic[78] and Lipson[79] which analyze the resolution gain in terms of the Shannon entropy. If resolution is gained then the entropy of the image must decrease because new spatial information has been obtained, but in return the fall in entropy must be compensated by an increase somewhere else in the system. Indeed the SIM acquisition process implies an increase in the total entropy because more photons are used to extract the information, i.e. acquisition of multiple images per plane requires more photons than the acquisition of a single wide field image. In this context Q measures how effectively the acquisition process was transformed into relevant spatial information. We believe that it is important to assess that the high spatial information is present in the raw images before even applying any correction or filtering to it, only then can be guaranteed that the resolution gain comes from the spatial frequencies extracted from the pristine data rather than from the image processing steps. This said, we clarify that the calculation of Q and filtering of the SIM reconstruction are not incompatible, Q is an assessment metric that provides insight of the raw data before attempting a reconstruction with it, for instance if a data set yields a Q very close to 0 we know that producing a resolution gain from it will be very unlikely, independently of the filters that are applied to it. On the other hand data sets with high Qs do not require any processing to yield a significant resolution gain but if needed the images can be filtered or deconvolved to get rid of background related artifacts.

The interest on developing guidelines and assessment strategies to evaluate super-resolution microscopy methods lies in the underperformance that these occasionally present. Such underperformance can be discouraging but it mostly arises from not knowing the limitations or fulfilling the minimum experimental conditions required from the method itself. Guidelines can be designed by establishing these limitations and evaluation metrics can further provide a quantitative approach to support a strategic decision on how to proceed with image acquisition or processing. In the particular case of SIM practical guidelines are very recent[39,53,80,81], the Q-factor contributes to them by conveying a quantitative quality criteria.

6 Conclusion

In this dissertation three projects were carried out under the scope of structured illumination microscopy: 1) The design and construction of a structured illumination microscope that produces lateral resolution gains of 3.3 respect to the wide field (csiLSFM, table 3.4). 2) The establishment of a SIM reconstruction processes designed to reduce periodic artifacts (RL-SIM, fig.4.13). 3) The development of a quantitative metric to evaluate whether a SIM data set contains enough information to produce a resolution gain or not (Q-factor). Besides the general results we just mentioned, each of the projects contributes to the field of SIM in the following aspects:

a) The most sophisticated set-up that combines light-sheet with structured illumination is the lattice light-sheet microscope[46], this set-up suffers from anisotropic resolution gains due to the lack of control over the pattern rotations. Under this context, the design of the csiLSFM contributes to achieving resolution gains closer to isotropy thanks to the flexible control of the light-sheets that our set-up offers (table 3.5)[36,59].

b) Contrary to the typical reconstruction approaches, the RL-SIM[37] does not require empirical tuning of functions to reduce artifacts[29,38], hence it provides a standardized pipeline for 2D/3D-SIM reconstruction. The design of the RL-SIM reconstruction was done after doing a spectral analysis of SIM artifacts. Section 4.1 of this thesis presents such analysis and unveils the origin of periodic and lobe-like artifacts, they arsie from discontinuous frequency domains and irregular spectrum respectively. To our knowledge such analysis and explicit

establishment of the artifacts' origin had not been done in literature before.

c) Evaluating the performance of structured illumination microscopy is a current field of interest, the literature for this subject is as recent as 2015[39,53,80,82]. This literature provides practical guidelines, covering topics like system calibration, sample mounting, corrections of intensity drops or sample drift, documenting types of artifacts that might be encountered in SIM and resolution assessment. The Q-factor contributes to this SIM evaluation tools with a quantitative metric that establishes a threshold value to rate a data set as optimal ($Q>0.11$) or sub-optimal ($Q>0.11$). This allows the use of Q as guideline to improve the data quality by tuning parameters like exposure time, laser power and pattern period (sec.5.2).

Although the projects presented here deliver standalone results their development was linked. The csiLSFM, involved casting patterns that are 1.4 times smaller than the resolution limit of the detection objective, thus acquisition of images with this set-up occurred beyond the capabilities of the detection lens. This made difficult to extract information for a super-resolution gain and evaluate when the acquired data set was good enough to produce high quality images. The role of the RL-SIM reconstruction was to facilitate the extraction and processing of a csiLSFM data set but not before confirming its suitability through the Q-factor. Such framework allowed us to dismiss dubious data and focus only on the processing of optimal data sets; this framework represents a future perspective of what an efficient structured illumination microscope could aim for, meaning that the set-up should provide live feedback to assist in the acquisition and to determine the quality of the recorded data (fig.5.12).

Appendix

7 Correction of defocus aberration in the DSLM due to refractive index mismatch in cleared spheroids

7.1 Motivation

Certain samples in the digital scanned laser light-sheet microscope (DSLM[83]) require a very specific mounting; in the case of cleared spheroids this involves multiple material layers with different refractive indices (fig.A1a). The spheroid needs to be introduced in a glass capillary of refractive index n_2 which contains a clearing solution (e.g. BABB (n_1)). Additionally, the detection objective requires an immersion medium (n_3)). In a single layer mounting the focal plane of the detection objective is at a fixed distance from the front lens, refered as nominal focus position (NFP). In the case of multiple layers mounting, the refractive index mismatch leads to a shift of the focal plane as function of the imaging depth (z), if this shift is not compensated the acquired images will be defocused (fig.A1b). To bring the image back to focus the detection objective must be moved to set the illuminated plane in the actual focus position (AFP) (fig.A1c).

To implement an automated re-focusing mode in the DSLM we calculated the AFP as function of the imaging depth and the refractive indices of the mounting layers. The function AFP($z;n_1, n_2, n_3$) was programmed in the detection objective motorized mount to achieve 3D stacks of cleared spheroids with focused images at each acquired plane.
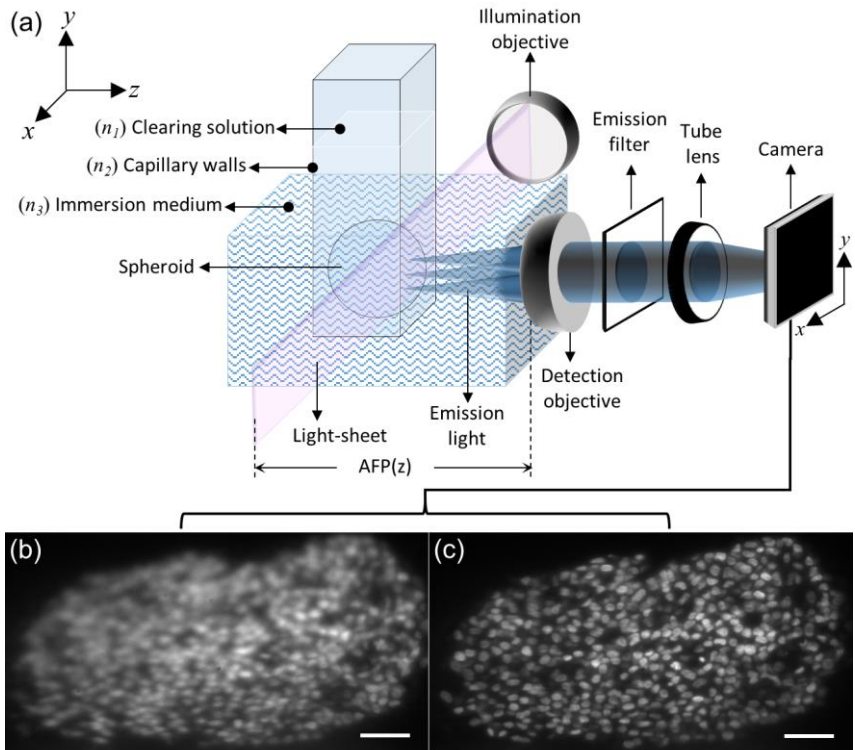
Fig.A 1 Defocused aberration in DSLM for cleared spheroids. (a) Cleared spheroid mounted in the DSLM. The mounting involves three clearing solution, glass capillary and immersion medium. The refractive index mismatch between these materials leads to a defocusing aberration that originates in the shift of the actual focus position as function of the imaging depth. **(b)** An out-of-focus plane within the spheroid. **(c)** The same plane but with the detection objective shifted along z to correct for the focus shift, i.e. this plane lies in the AFP of the detection lens. Scale bar: 50 μm.
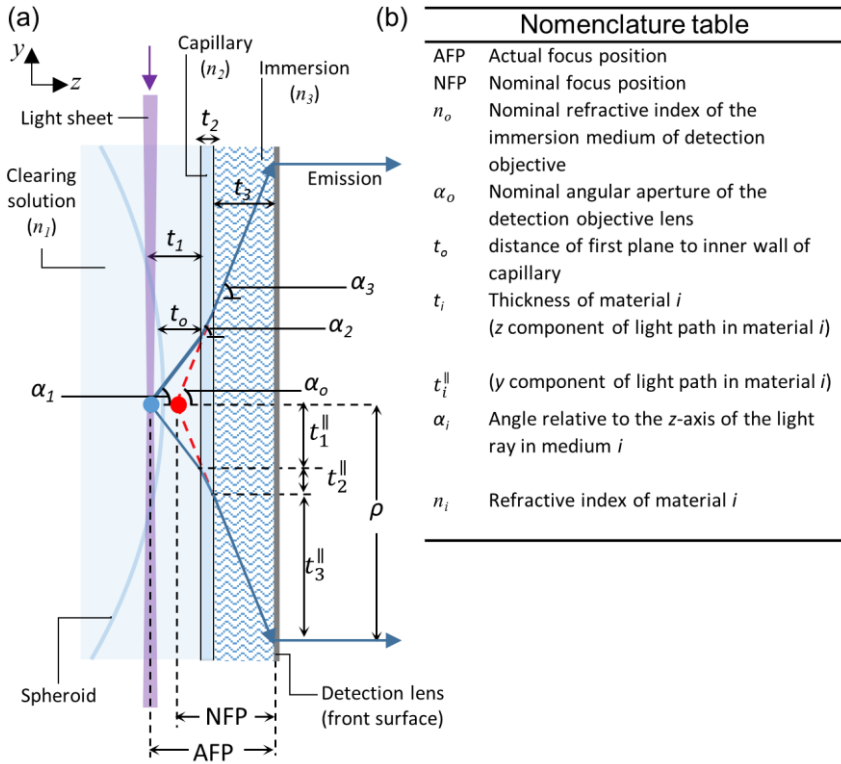
Fig.A2 Optical path of the emission light in the DSLM. **(a)** Top view (zx) of the main rays of the emission light traveling throught the different material layers before reaching the front surface of the detection lens. The blue solid line represents the actual path, i.e. accounting for refraction at each interface. The red dashed line represents the virtual path, i.e. as if no refractive index mismatch occurred. **(b)** Nomenclature of parameters involved in the mathematical model.

7.2 Theory

Fig.A2a shows the sketch of the main emission rays traveling through the different material layers. We considered a virtual path corresponding to non-refracted rays (dashed red lines), i.e. no index mismatch, and the

actual path accounting for the refraction at each interface (blue solid line). The list of parameters involved in the geometrical optics model are listed in fig.A2b.

The largest angle of emitted rays that the detection objective can detect is given by its nominal angular aperture α_o, the focusing condition for the refracted rays is then that its entry angle α_3 to the lens is equal to the angle α_o. The geometric condition for the refracted rays to fall within the focused cone of light is to equal the optical path lengths along the y axis of the virtual and actual rays, i.e.:

$$\frac{sin\,\alpha_o}{cos\,\alpha_o} NFP = \rho = t_1^{\parallel} + t_2^{\parallel} + t_3^{\parallel}, \tag{A1}$$

where $t_i^{\parallel}$ is proportional to the materials thicknesses t_i:

$$t_i^{\parallel} = \frac{sin\,\alpha_i}{cos\,\alpha_i}\,t_i. \tag{A2}$$

The angle α_o is given by the definition of NA, α_1 and α_2 are calculated from Snell's law, hence:

$$\alpha_o = \alpha_3 = \arcsin\left(\frac{NA}{n_o}\right); \alpha_1 = arcsin\left(\frac{n_3}{n_1}\frac{NA}{n_o}\right); \alpha_2 = arcsin\left(\frac{n_3}{n_2}\frac{NA}{n_o}\right), \tag{A3}$$

with n_o being the refractive index of the detection objective nominal immersion medium. According to the geometry of fig.A2a:

$$t_3 = AFP - (t_1 + t_2) \tag{A4}$$

and

$$t_1(j) = t_o + j\Delta z. \tag{A5}$$

Appendix

j is the plane number, $j=0,1,2,\ldots(N\text{-}1)$ and Δz is the axial pitch of the image stack comprised by N planes. Finally, using eqs.A2 to A5 in eq.A1, we obtain the AFP:

$$AFP(j) = j\Delta z \left(1 - \frac{n_3}{n_1}\frac{cos\alpha}{cos\alpha_1}\right) + t_2 \left(1 - \frac{n_3}{n_2}\frac{cos\alpha}{cos\alpha_2}\right) + t_o \left(1 - \frac{n_3}{n_1}\frac{cos\alpha}{cos\alpha_1}\right) + NFP. \qquad \text{(A6)}$$

This last equation shows that the actual focus position holds a linear relation with the imaging depth $j\Delta z$, hence to correct for defocusing the detection objective must be moved in constant steps at each acquired plane j. The correction factor m is given by the slope of eq.A6:

$$m = \left(1 - \frac{n_3}{n_1}\frac{cos\alpha}{cos\alpha_1}\right). \qquad \text{(A7)}$$

and the correction step of the detection objective is:

$$m\Delta z \qquad \text{(A8)}$$

7.3   Set-up and sample mount

The detailed functioning and configuration of the DSLM can be found in multiple references. We show in fig.A3 different perspectives of the chamber and the orthogonal arrangement of the illumination and detection objectives (fig.A3a/b/c). The illumination objective is air immersion with NA=0.16/5X. The illumination wavelength is a 370 nm laser used to excited DAPI. The detection objective is water immersion with NA=0.5/20X. This objective is mounted on a nanopositioner with 400 μm of travel range (P-725 PIFOC) (fig.A3b). In the detection path we have a 390 nm longpass emission filter (F47-390, AHF Analysentechnik), a tube lens and a CMOS camera (DMK23UX174, imaging source). The chamber is filled with the immersion medium of the detection objective, we tried

two: water which is the nominal one (n_3=1.333) and thiodiethanol (TDE /n_3=1.52)[84].

For the sample mounting we first dehydrated the DAPI stained fixed spheroid with ethanol. The dehydration was carried out by keeping the spheroids in ethanol solutions with ascending concentrations: 30, 50, 70, 90, 96 and 100%. The spheroid was maintained in each solution at room temperature for two minutes. After dehydration we proceeded with the optical clearing of the spheroid by immersing it in an embryo dish filled with approximately 200 µl of Benzyl Alcohol/Benzyl Benzoate (BABB, n_1=1.56)[85,86]. The spheroid remains in BABB for 5 minutes and then is gently extracted along with few microliters of BABB solution (~5 µl). The pipette's content is injected in a squared glass capillary of dimensions: 2.5 cm in length, inner walls of 1.10x1.10 mm and outer walls of 1.35x1.35 mm (fig.A3f). One end of the capillary is sealed with a Teflon pin and the other with a metallic pin that is inserted in the sample holder. Lastly, the chamber is filled with the selected immersion medium, either water or TDE, and the sample is ready for imaging.

Fig.A3d show the front view of the capillary mounted in the microscope, the spheroid is being illuminated with the light-sheet, the fluorescence can be seen with the bare eye (figs.A3e, red square).

Appendix
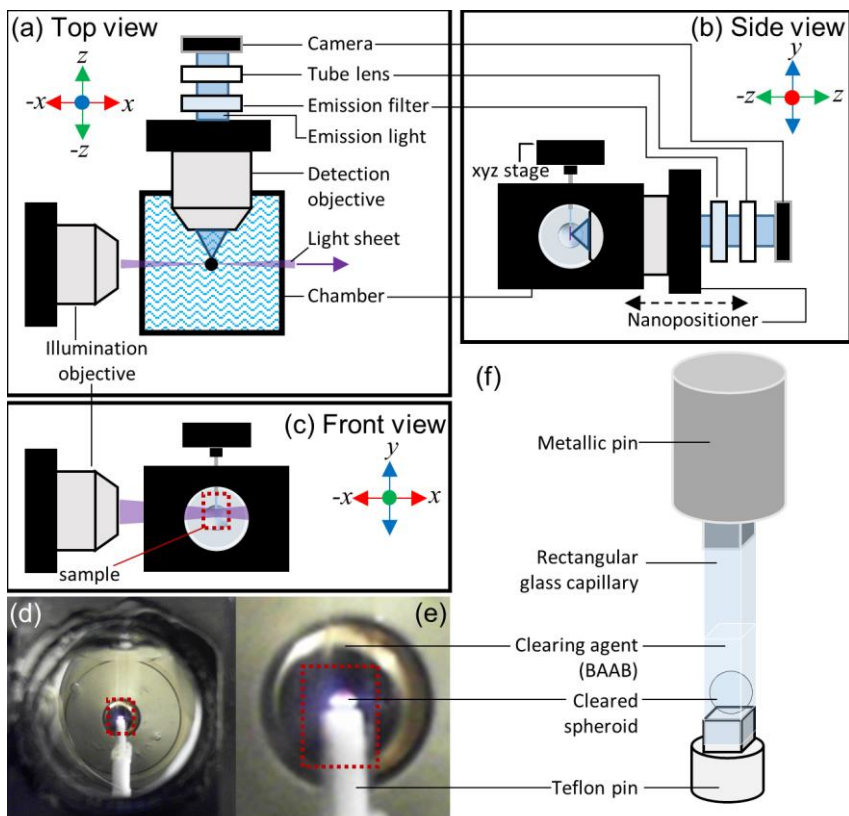
Fig.A3 DSLM set-up and sample mounting. Set-up configuration seen from (**a**) Top view, (**b**) side view and (**c**) front view. The nanopositioner in which the detection objective is mounted is the main element to achieve the automated re-focusing of each plane, side view. (**d**) Front view, the glass capillary containing the spheroid is seen in front of the detection lens (dashed box). (**e**) Magnification of (**d**). (**f**) Sketch of the elements involved in the spheroid mounting.
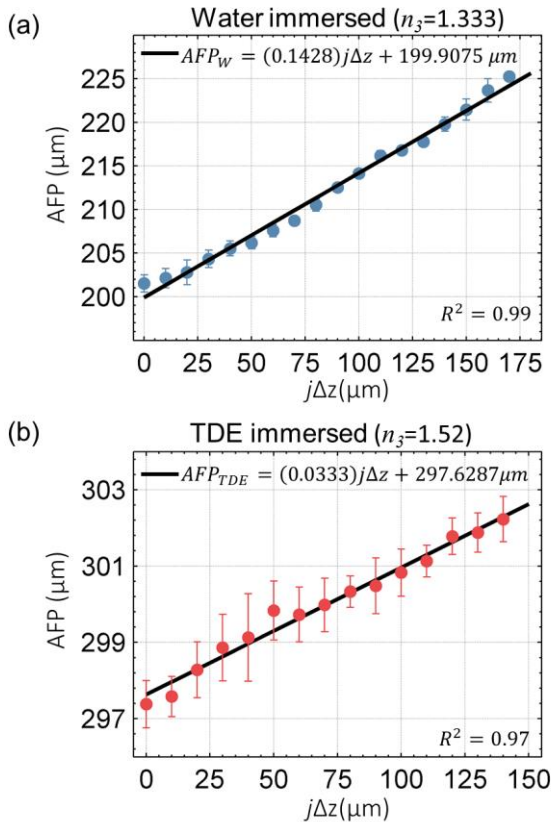
Fig.A4 AFP vs imaging depth plots. Each point represents an imaging depth relative to the first plane (j=0) and the AFP recorded as the displacement of the detection objective. The points were acquired by visually determining the best in-focus image, two immersion medium were used: **(a)** Water and **(b)** TDE. The black lines are the fitted lines to the points.

Appendix

7.4 Results

7.4.1 Experimental confirmation of equation A6 by manual re-focusing

To experimentally confirm the linearity of eq.A6 we acquired images of a cleared spheroid at an inter-plane distance of $\Delta z=10$ µm. The detection objective was moved along the z-axis to re-focus the image at each plane, the focused image was determined by visual inspection. The in-focus position of the detection objective was recorded as a relative AFP and plotted against the imaging depth ($j\Delta z$). This acquisition process was repeated three times to obtain average results, the plots for water and TDE as immersion media (n_3) are shown in fig.A4a/b. The fitted lines give a slope of 0.1428 ± 0.0036 and 0.0333 ± 0.0014 for water and TDE respectively. These values are very close to those that can be obtained from eq.A7:

$$m_{water} = 0.1718; m_{TDE} = 0.0299, \tag{A9}$$

thus the model established by eq.A6 is validated.

7.4.2 Automated re-focused acquisition

The nanopositioner mount was programmed to move with a constant step size $m\Delta z$ at each acquired plane. Although the theoretical values of m are of the same order of the experimental ones (eq.A9), they are not exactly the same, hence to have an immediate experimental estimate of m, we use the linearity of eq.A6 and calculate it using only two reference points, an initial in-focus plane at a position z_o and a finale one at z_f. The positions of the detection objective that set these planes in-focus are recorded as AFP_o and AFP_f (fig.A5), accordingly the experimental correction factor m is given by:

$$m = \frac{AFP_f - AFP_o}{z_f - z_o}. \tag{A10}$$

Figs.A6/A7 show the *xz* maximum projection of a spheroid acquired without the defocusing correction, i.e. detection objective fixed, and with the automated re-focusing using the correction step *m*. The images in fig.A6 were acquired with water as immersion medium and in fig.A7 with TDE. The inter-plane distance for both acquisitions was Δz=1.29 μm and the experimental *m* were m_{water}=0.1631 μm and m_{TDE}=0.0297 μm (eq.A10). The improvement brought by the re-focusing in fig.A6 is obvious as the ratio between the BABB and water refractive indices is large, about 1.2. In the case of BABB and TDE this is only 1.02, thus the improvement in fig.A7 is not so evident across the entire stack, nevertheless the re-focusing correction is required in the last planes of the stack as shown by the magnifications in the orange squares (fig.A7).

Appendix
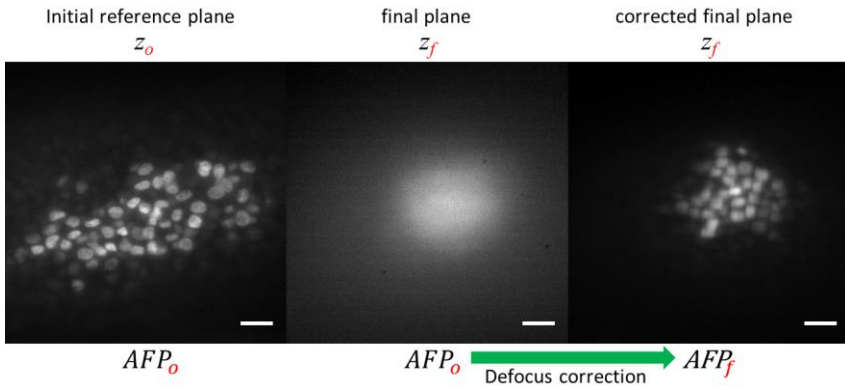
Fig.A5 Experimental estimation of correction factor *m*. A first plane is imaged at an imaging depth z_o, the plane is in focus thus the detection objective focal plane is at AFP_o. The sample is moved to illuminate a plane at a greater depth (z_f), since the detection objective is still in AFP_o the image appears defocused, to get a sharp image the detection objective has to be moved so its focus at this depth coincides with AFP_f. The two points (z_o,AFP_o) and (z_f,AFP_f) are used to calculate the correction factor *m* as shown in eq. A10. Scale bar: 25 µm.
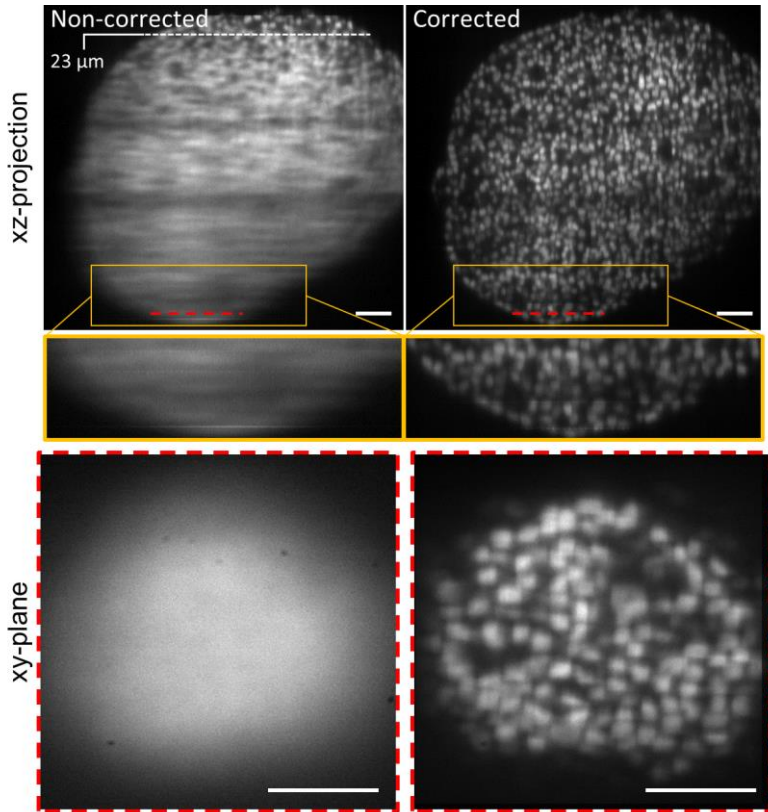
Fig.A6 Automated re-focus correction vs non-corrected stacks (water immersion).
Left column (top): *xz* projection of a cleared spheroid, the detection objective was not
programmed to move during acquisition so not defocus correction was applied. The
white dashed line indicates the first plane that is out-of-focus according to eq.A12
(23 µm). **(center):** magnification of the last planes of the stack. **(bottom):** *xy* view
of the plane marked by the dashed red line. **Right column (top):** *xz* projection with the
re-focused acquisition. **(center):** magnification. **(bottom):** *xy* view. Scale bar:
50 µm.
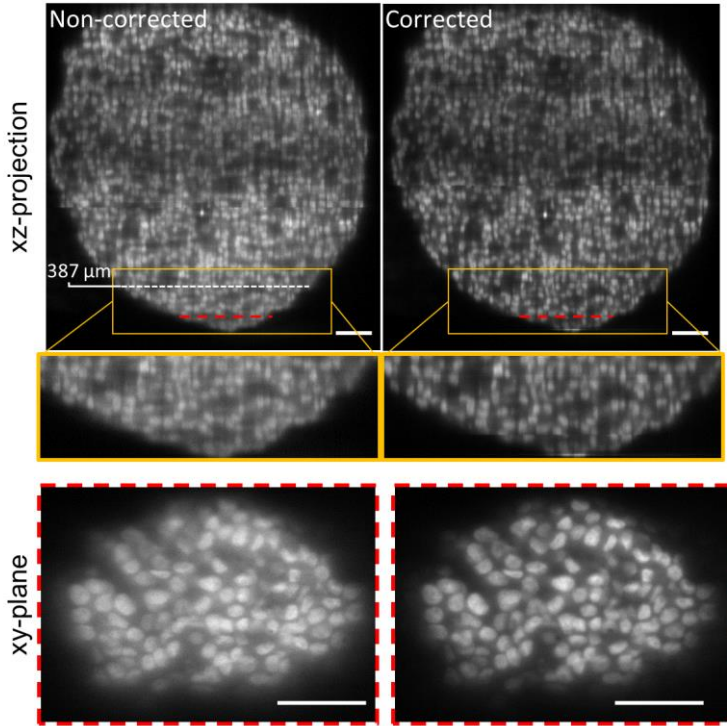
Fig.A7 Automated re-focus correction vs non-corrected stacks (TDE immersion).
Left column (top): *xz* projection of a cleared spheroid, the detection objective was not
programmed to move during acquisition so not defocus correction was applied. The
white dashed line indicates the first plane that is out-of-focus according to eq.A12
(387 µm). **(center):** magnification of the last planes of the stack. **(bottom):** *xy* view
of the plane marked by the dashed red line. **Right column (top):** *xz* projection with the
re-focused acquisition. **(center):** magnification. **(bottom):** *xy* view. Scale bar:
50 µm.
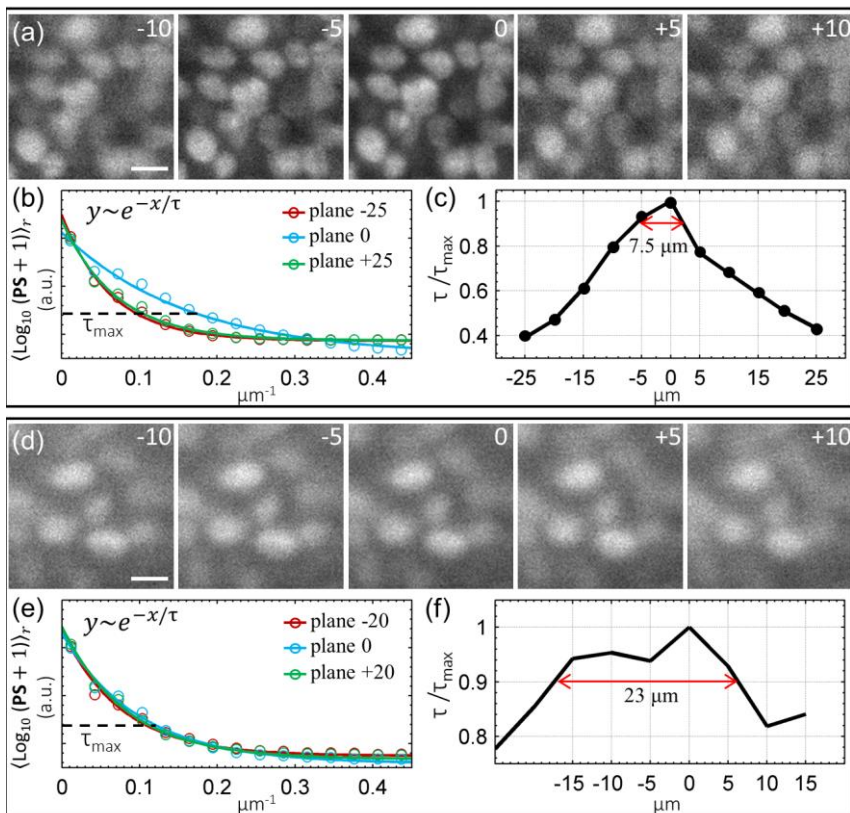
Fig.A8 Experimental calculation of the DOF. (Water/TDE) **(a)** Multiple images of a central plane (0) acquired at different displacements of the detection objective (-10,-5,+5,+10). **(b)** Circular average of the images' logarithmic power spectrum (solid lines) and its fitted curve, an exponential decay (circles). **(c)** The decay constant is extracted from the fit and plotted against the detection objective displacement.

Appendix

7.4.3 Defocusing condition. When is the re-focusing necessary?

Using an immersion medium like TDE which has a refractive index closer to that of BABB reduces the defocusing aberration and it makes the correction relevant only at large imaging depths (fig.A7). We define a quantitative criterion to determine at which plane the correction becomes necessary. The criterion is logically defined considering the following, the a plane in the stack is defocused when the accumulated shift of the AFP is larger than the depth of field (DOF) of the detection objective, i.e.:

$$jm\Delta z \geq \frac{DOF}{2} \qquad (A11)$$

The term 2 in the denominator supposes that the best in-focus condition is in the center of the DOF. According to eq.A11 the first plane j^* which will be out-of-focus occurs at an imaging depth of:

$$j^*\Delta z = \frac{1}{m}\frac{DOF}{2}. \qquad (A12)$$

To estimate the DOF of the detection objective we focused on a small region of a central plane and moved only the detection objective back and forth in steps of 5 µm to acquire images at each step (fig.A8a/d). Then we calculated the circular average of their logarithmic power spectrum and fit it to an exponential decay function $\sim exp(-x/\tau)$ (fig.A8b/e). The plots in fig.A8c/f show the relative decay constant (τ/τ_{max}) vs the detection objective displacement. The constant τ decreases as the detection objective moves away from the central in-focus position (0), which yields the maximum value τ_{max}. We consider the size of the DOF as the length between the points at which τ_{max} has lost 10% of its value, hence the DOF of the detection objective in water is 7.5 µm and in TDE 23 µm. Substituting these values in eq.A12 and using the factors m of figs.A6 and

A7, we conclude that the focus correction is required after an imaging depth of 23 and 387 µm for water and TDE respectively. These planes have been marked with a white dashed line in the *xz* projections of figs.A6 and A7.

The criterion given in eq.A12 can have another standpoint, namely it can be applied to estimate the sample sizes that do not need the refocusing correction, for instance if we take the theoretical value *m* for TDE (eq.9) into eq.A12 the result is 384 µm , then we can generally say that samples much smaller than 384 µm along the *z* direction do not need the focus correction since any plane of the stack will be within the DOF.

RL-SIM MATLAB implementation

The following lines contain 6 MATLAB functions that comprise the implementation of the RL-SIM reconstruction pipeline for 2D-SIM data sets; it can also be adapted to 3D-SIM data by using the corresponding linear system of equations (eq.22). The general work flow of the pipeline occurs as described by the diagram in fig.4.13. All functions are commented and explained, comments in MATLAB follow after the percentage symbol '%'. The syntax to start a code is function[Outputs]=name(Inputs). At the beginning of each function there are three sections, "Documentation", "Inputs" and "Outputs", the first one gives a general description of the function, second and third explain the required inputs and outputs. The functions of RL-SIM are:

1) **twoSIMrec.m**: core function of the pipeline.
2) **PointSF.m**: creates a theoretical 2D *PSF* of the detection objective.
3) **PreDecon.m**: applies the pre-reconstruction deconvolution and transforms the data into the Fourier space.
4) **correlations.m**: calculates the pattern spatial frequency through correlations.
5) **PostDec.m**: applies the post-reconstruction deconvolution.
6) **reconstruction_data.m**: produces a.txt file with the reconstruction info, including the *Q*-factor to evaluate the quality of the input data.

twoSIMrec.m

```
   function [DeconSIM,SIM,WF,Ktrans_all,ExtPSF,SNR,avgSNR,...
      SNR_SIM,avgSNR_SIM,Qfactor]=...
      twoSIMrec(path,NA,lambda,ps,rg,Sx,Sy,n,state)
   tic
 5 %----Documentation----
   %This code reconstructs a superresolution image from a 2D-SIM acquisition
   %comprised by a set of 9 2D-SIM images (tif format).  The images are named
   %000i,026i and 154i for the 1st, 2nd and 3d pattern directions
   %respectively i is an index indicating the phase of the pattern. i=1,2,3.
10 %----Inputs-----------
   %path(string)=file path of the folder containing 000i,026i and 154i
   %NA=Numerical aperture of the detection objective
   %lambda=emission wavelengths in nm
```

```
   %ps=image pixel size in nm
15 %rg=expected resolution gain
   %Sx=image dimensions along x in pixels
   %Sy=image dimensions along y in pixels
   %n=number of elements in which the interval [0,2pi] is divided
   %state(string)='on' or 'off' switches the pre-deconvolution on/off
20 %----Outputs----------
   %DeconSIM=SIM reconstruction with postdec
   %SIM=SIM reconstruction (predec/no predec) depends on the state input
   %WF=Wide field image (dec/no dec) depends on the state input
   %Ktrans_all=Estimated pattern frequency
25 %ExtPSF=Extended point spread function
   %SNR=SNR of the raw images
   %avgSNR=Mean of SNR
   %Qratio=Qfactor
   %----START------------
30 format='tif';% Image format
   [PSF]=PointSF(NA,lambda/ps,Sx,Sy);
   [FTimages]=preDecon(path,Sx,Sy,format,PSF,state);
   est=max([Sx Sy]);
   Rad=(((est*NA)/(0.55*(lambda/ps)))*(rg-1));
35 x=1:1:Sx;y=1:1:Sy;
   [X,Y]=meshgrid(x,y);X=repmat(x,[Sy 1]);Y=repmat(y',[1 Sx]);
   %----Allocation Matrices---
   A=zeros(Sy,Sx,n);B=zeros(Sy,Sx,n);C=zeros(Sy,Sx,n);
   Ktrans_all=zeros(2,2,3);K_all=zeros(2,2,3);
40 angle=linspace(0,2*pi,n);
   Pixelshift_all=zeros(2,2,3);
   HRcomponents=zeros(Sy,Sx,3);Standardcomp=zeros(Sy,Sx,3);
   %----Linear system solution---
   u=(0.5^2)*(2*(exp(-2i*pi/3)-exp(2i*pi/3))+(exp(4i*pi/3)-exp(-4i*pi/3)));
45 phi=repmat(reshape(linspace(0,2*pi,n),[1 1 n]),[Sy Sx]);
   for j=1:3%pattern orientation j
   A=((0.5/u)*exp(1i*phi)).*repmat((((exp(4i*pi/3)-exp(2i*pi/3))*...
       FTimages(:,:,j,1))+((1-exp(4i*pi/3))*FTimages(:,:,j,2))+...
       ((exp(2i*pi/3)-1)*FTimages(:,:,j,3))),[1 1 n]);%Left shifted domain
50 B=(0.5^2/u)*(((exp(-2i*pi/3)-exp(2i*pi/3))*(FTimages(:,:,j,1)+...
       FTimages(:,:,j,3)))+((exp(4i*pi/3)-exp(-4i*pi/3))...
       *FTimages(:,:,j,2)));%Central domain
   C=-((0.5/u)*exp(-1i*phi)).*repmat((((exp(-4i*pi/3)-exp(-2i*pi/3))*...
   FTimages(:,:,j,1))+((1-exp(-4i*pi/3))*FTimages(:,:,j,2))+...
55     ((exp(-2i*pi/3)-1)*FTimages(:,:,j,3))),[1 1 n]);%Right shifted domain
   %----Pattern spatial frequency retrieval---
   m=randi([1 n],1);
   [K,Pixelshift,Ktrans]=correlations(A(:,:,m),B,C(:,:,m),j,Rad);
   %----Q-factor calculation----
60 OTF=mat2gray(abs(fftshift(fft2(PSF))));Signal=OTF>0.05;Noise=OTF<=0.05;
   S1=Signal.*abs(A(:,:,m));S2=Signal.*abs(B);S3=Signal.*abs(C(:,:,m));
   N=Noise.*(abs(B));
   S1(S1==0)=[];S2(S2==0)=[];S3(S3==0)=[];N(N==0)=[];
   N1=Noise.*abs(A(:,:,m));N3=Noise.*abs(C(:,:,m));
65 N1(N1==0)=[];N3(N3==0)=[];
   SNR(j)=(mean(S2)/mean(N));
   SNR_SIM(j)=mean(S2)/mean2([N1(:) N3(:)]);
```

RL-SIM in MATLAB

```
       Qmat(:,j)=[mean(S1)-mean(N1);mean(S3)-mean(N3)]./...
                 [mean(S2)+mean(N1);mean(S2)+mean(N3)];
70   clear S1 S2 S3
       Ktrans_all(:,:,j)=Ktrans;K_all(:,:,j)=K;
       Pixelshift_all(:,:,j)=Pixelshift;K_all(j)=K;
       %----Pattern phase and extended domains retrieval---
       ImA=((ifft2(A))).*(repmat(exp(1i*((X-(round((Sx+1)/2)))*(Ktrans(2,1))+...
75     (Y-(round((Sy+1)/2)))*(Ktrans(1,1)))),[1 1 n]));
       ImB=repmat((ifft2(B)),[1 1 n]);figure(120);
       ImC=((ifft2(C))).*(repmat(exp(1i*((X-(round((Sx+1)/2)))*(Ktrans(2,2))+...
       (Y-(round((Sy+1)/2)))*(Ktrans(1,2)))),[1 1 n]));
       [CC]=norm_corr(mat2gray(abs(ImA+ImB+ImC)),mat2gray(abs(ImB)));
80   [PHI,ind]=max(CC);clear PHI
       phi_all(j)=angle(ind);
       HRcomponents(:,:,j)=(ImA(:,:,ind)+ImC(:,:,ind));
       Standardcomp(:,:,j)=ImB(:,:,ind);
       %----Plot window----
85   figure(1);subplot(3,3,3*j);plot(linspace(0,2*pi,n),CC);
       axis([0 2*pi min(CC)-0.001 max(CC)+0.001])
       figure(2);subplot(4,4,j);
       imagesc(log2(abs((fft2(Standardcomp(:,:,j)+HRcomponents(:,:,j))))+1));
       axis image;axis off
90   end
       %----Super-resolution image assembly-----
       WF=abs(sum(Standardcomp,3)/3);
       WF=uint16(mat2gray(abs(WF))*65535);
       SIM=sum(HRcomponents,3)+(sum(Standardcomp,3)/3);
95   SIM=uint16(mat2gray(abs(SIM))*65535);
       [ExtPSF]=PostDec(Sx,Sy,Ktrans_all,PSF);
       DeconSIM=deconvlucy(padarray(double(SIM),[10 10],'symmetric'),ExtPSF,5);
       DeconSIM=DeconSIM(11:10+Sy,11:10+Sx);
       DeconSIM=uint16(mat2gray(abs(DeconSIM))*65535);
100  figure(2);subplot(4,4,4);
       centerx=round((Sx+1)/2);centery=round((Sy+1)/2);
       imagesc(imresize(ExtPSF(centery-5:centery+5,centerx-5:centerx+5),2));
       axis image;
        %----Assesment factors of SIM images----
105  Qfactor=mean2(Qmat);
       avgSNR_SIM=mean(SNR_SIM);
       avgSNR=mean(SNR);
       Acq=[NA,ps,lambda,rg];
       figure(2);subplot(4,4,[5 6 9 10 13 14]);
110  imagesc(mat2gray(log2(abs(fftshift(fft2(DeconSIM)))+1)));
       axis image;axis off
       figure(2);subplot(4,4,[7 8 11 12 15 16]);
       imagesc(mat2gray(log2(abs(fftshift(fft2(WF)))+1)));
       axis image;axis off;
115  %----Saving reconstruction data and reconstructions----
       %WF and SIM images are saved in a folder called Reconstructions
       %contained in the directory given by path.The name of the images bear
       %a label with the applied operations,i.e. the pre- or post-deconvolution
       mkdir(path,'Reconstructions');
120  if strcmp(state,'on')
       prefix='PreDec_';
```

```
    elseif strcmp(state,'off')
    prefix='';
    end
125 imwrite(WF,strcat(path,'\Reconstructions','\',prefix,'WF','.tif'),'tif');
    imwrite(SIM,strcat(path,'\Reconstructions','\',prefix,'SIM','.tif'),'tif');
    imwrite(DeconSIM,strcat(path,'\Reconstructions','\',prefix,...
        'PostDec_SIM','.tif'),'tif');
    imwrite(uint16(mat2gray(abs(imresize(SIM,2)))*65535),strcat(path,...
130     '\Reconstructions','\',prefix,'SIM_2X','.tif'),'tif');
    imwrite(uint16(mat2gray(abs(imresize(DeconSIM,2)))*65535),strcat(path,...
        '\Reconstructions','\',prefix,'PostDec_SIM_2X','.tif'),'tif');
    %----Data transfer----
    %Acquisition and reconstruction data is transferred to a .txt file
135 reconstruction_data(path,Ktrans_all,Pixelshift_all,K_all,phi_all,...
        Acq,SNR,avgSNR,avgSNR_SIM,Qmat,Qfactor,prefix);
    toc
    end
```

PointSF.m

```
    function [PSFxy]=PointSF(NA,lambda,Sx,Sy)
    %----Documentation----
    %This functions calculates the point spread function given the imaging
    %acquisition conditions
  5 %----Inputs-----------
    %NA=Numerical aperture of detection objective
    %M=Objective magnification
    %lambda=emission wavelength in pixels
    %Sx=image dimensions along x in pixels
 10 %Sy=image dimensions along y in pixels
    %----Outputs----------
    %PSFxy=2-variable function representing the intensity profile of the
    %detection objective point spread function
    %----START------------
 15 lambda=lambda;
    x=1:1:Sx;y=1:1:Sy;
    X=repmat(x,Sy,1);Y=repmat(y',1,Sx);
    R=(NA/(lambda))*(sqrt((X-((Sx/2)+1)).^2+(Y-((Sy/2)+1)).^2));
    PSFxy=(abs(2*besselj(1,2*pi*R)./(2*pi*R))).^2;
 20 PSFxy(isnan(PSFxy))=1;
    norm=trapz(trapz(PSFxy,1));
    PSFxy=PSFxy/norm;
    end
```

PreDecon.m

```
    function [FTimages]=preDecon(path,Sx,Sy,format,PSF,state)
    %----Documentation----
    %This function  applies the pre-deconvolution (if activated)
    %to the SIM image data set.It also Fourier transforms the data set so it
```

140

```
  5 %can be used in the reconstruction process.
    %----Inputs-----------
    %The inputs are taken from the main code (twoSIMrec.m)
    %format(string)=tif
    %----Outputs----------
 10 %FTimages=A matrix containing the Fourier transform of the 9 2D-SIM images.
    %the images are/aren't pre-deconvolved if state='on/off'.
    %----START-----------
    FTimages=zeros(Sy,Sx,3,3);
    fa=zeros(1,3);fb=zeros(1,3);fc=zeros(1,3);
 15 mkdir(path,'DeconvWF_series')
    %----Intensity normalization----
    for i=1:3
    A=imread(strcat(path,'\000',num2str(i)),format);fa(i)=mean2(A);
    B=imread(strcat(path,'\026',num2str(i)),format);fb(i)=mean2(B);
 20 C=imread(strcat(path,'\154',num2str(i)),format);fc(i)=mean2(C);
    end
    FACTOR=mean([fa fb fc]);
    for i=1:3
    clear A B C
 25 A=imread(strcat(path,'\000',num2str(i)),format);A=(FACTOR/fa(i))*A;
    B=imread(strcat(path,'\026',num2str(i)),format);B=(FACTOR/fb(i))*B;
    C=imread(strcat(path,'\154',num2str(i)),format);C=(FACTOR/fc(i))*C;
    %----Pre-deconvolution(state='on')----
    if strcmp(state,'on')
 30 A=padarray(A,[10 10],'symmetric');B=padarray(B,[10 10],'symmetric');
    C=padarray(C,[10 10],'symmetric');
    Adec=deconvlucy(A,PSF,10,uint16(mean2(A)/2)*(0.01));
    Bdec=deconvlucy(B,PSF,10,uint16(mean2(B)/2)*(0.01));
    Cdec=deconvlucy(C,PSF,10,uint16(mean2(C)/2)*(0.01));
 35 Adec=Adec(11:Sy+10,11:Sx+10);Bdec=Bdec(11:Sy+10,11:Sx+10);
    Cdec=Cdec(11:Sy+10,11:Sx+10);
    FTimages(:,:,1,i)=fftshift(fft2(imresize(Adec,1)));
    FTimages(:,:,2,i)=fftshift(fft2(imresize(Bdec,1)));
    FTimages(:,:,3,i)=fftshift(fft2(imresize(Cdec,1)));
 40 imwrite(uint16(65535*mat2gray(Adec)),strcat(path,'\DeconvWF_series',...
        '\DeconWF_','000',num2str(i),'.tif'),'tif')
    imwrite(uint16(65535*mat2gray(Bdec)),strcat(path,'\DeconvWF_series',...
        '\DeconWF_','026',num2str(i),'.tif'),'tif')
    imwrite(uint16(65535*mat2gray(Cdec)),strcat(path,'\DeconvWF_series',...
 45     '\DeconWF_','154',num2str(i),'.tif'),'tif')
     elseif strcmp(state,'off')
    FTimages(:,:,1,i)=fftshift(fft2(imresize(A,1)));
    FTimages(:,:,2,i)=fftshift(fft2(imresize(B,1)));
    FTimages(:,:,3,i)=fftshift(fft2(imresize(C,1)));
 50 end
    end
    end
```

correlations.m

```
function [K,Pixelshift,Ktrans]=correlations(A,B,C,counter,Rad)
```

```
   %----Documentation----
   %This code estimates the pattern frequency required to reconstruct the
   %super-resolution image.  The estimation is carried out through the
 5 %correlations of domains A and C with the central domain B
   %----Inputs-----------
   %A/B/C=Left/Central/Right domain
   %counter=index j, i.e. pattern direction
   %Rad=Exclusion radius (pixels)to estimate the pattern frequency
10 %----Outputs----------
   %Pixelshift=Position of the correlation peaks (Pixels)
   %Ktrans=Pixelshift but respect to the center of the image
   %K=Norm of Ktrans, i.e. estimate of the pattern frequency
   %----START------------
15 Sx=size(A,2);Sy=size(A,1);
   [est,pos]=max([Sx Sy]);
   ImA=(ifft2(A));ImB=(ifft2(B));ImC=(ifft2(C));
   x=1:1:Sx;y=1:1:Sy;X=repmat(x,[Sy 1]);Y=repmat(y',[1 Sx]);
   Xcent=round((Sx+1)/2);Ycent=round((Sy+1)/2);
20 %----Correction of image size anisotropy----
   if pos==1
   rx=1:1:Sx;ry=1:1:Sx;
   Rx=repmat(rx,[Sx 1]);Ry=repmat(ry',[1 Sx]);
   RXcent=round((Sx+1)/2);RYcent=round((Sx+1)/2);
25 elseif pos==2
   rx=1:1:Sy;ry=1:1:Sy;
   Rx=repmat(rx,[Sy 1]);Ry=repmat(ry',[1 Sy]);
   RXcent=round((Sy+1)/2);RYcent=round((Sy+1)/2);
   end
30 %----Correlation A*B----
   R=sqrt((Rx-RXcent).^2+(Ry-RYcent).^2);
   ROI= R>=0.9*Rad & R<=1.1*Rad;
   ROI=imresize(ROI,[Sy Sx]);
   factor=2;%Interpolation factor to increase the resolution of the estimation
35 Left=imresize(ROI,factor).*fftshift(fft2(ImB.*ImA,Sy*factor,Sx*factor));
   a=max(max(abs(Left)));Left1=abs(Left);Left=abs(Left);
   figure(1);subplot(3,3,(3*counter)-2);imagesc(mat2gray(abs(Left)));
   axis image;
   Left1(Left1<a)=0;[rl,cl]=find(Left1);
40 %----Correlation C*B----
   Right=imresize(ROI,factor).*fftshift(fft2(ImB.*ImC,Sy*factor,Sx*factor));
   b=max(max(abs(Right)));Right1=abs(Right);Right=abs(Right);
   figure(1);subplot(3,3,(3*counter)-1);imagesc(mat2gray((abs(Right))));
   axis image;
45 Right1(Right1<b)=0;[rr,cr]=find(Right1);
   %----Pixelshift contains the coordinates of the correlation peaks----
   Pixelshift=[rl rr;cl cr];
   Sxalt=Sx*factor;Syalt=Sy*factor;
   centx=round((Sxalt+1)/2);centy=round((Syalt+1)/2);
50 Centalt=[centy centy;centx centx];
   Lpix=repmat([Syalt;Sxalt],[1 2]);
   %----Ktrans calculation----
   Ktrans=(-2*pi)*((Pixelshift-Centalt)./Lpix);
   %----K calculation----
55 K=sqrt(sum((Ktrans(:,1).^2)));
```

RL-SIM in MATLAB

```
      end
```

PostDec.m

```
   function [ExtPSF] =PostDec(Sx,Sy,Ktrans_all,PSF)
   %----Documentation----
   %This function calculates the extended PSF of a SIM acquisition
   %----Inputs-----------
 5 %The inputs are taken from the main code (twoSIMrec.m).
   %----Outputs----------
   %ExtPSF=2D Intensity profile of the extended point spread function
   %----START------------
   x=1:1:Sx;y=1:1:Sy;[X,Y]=meshgrid(x,y);X=repmat(x,[Sy 1]);Y=repmat(y',[1
10 Sx]);
   PSFB=imresize(PSF,1);
   for j=1:3
   PSFA=PSFB.*(exp(1i*((X-(round((Sx+1)/2)))*(Ktrans_all(2,1,j))+...
       (Y-(round((Sy+1)/2)))*(Ktrans_all(1,1,j)))));
15 PSFC=PSFB.*(exp(1i*((X-(round((Sx+1)/2)))*(Ktrans_all(2,2,j))+...
       (Y-(round((Sy+1)/2)))*(Ktrans_all(1,2,j)))));
   SIM_PSF(:,:,j)=PSFA+(PSFB/3)+PSFC;
   end
   ExtPSF=mat2gray(abs(sum(SIM_PSF,3)));
20 end
```

reconstruction_data.m

```
   function [] =reconstruction_data(path,Ktrans_all,Pixelshift_all,K_all,...
       phi_all,Acq,SNR,avgSNR,avgSNR_SIM,Qmat,Qfactor,prefix)
   %----Documentation----
   %This code opens a file called reconstruction_data.txt in which the
 5 %reconstruction and acquisition information is written and formatted
   %column wise.
   %----Inputs-----------
   %All the inputs for this function are taken from the main code
   %(twoSIMrec.m).Thus no manual input is required.
10 %----Outputs----------
   %A text file saved in the directory given by path.The file displays
   %for each pattern orientation, its orientation angle in degrees,
   %the Pixelshift,Ktrans_all as well as its norm K, the pattern phase phi in
   %radians and the pattern period in nm.
15 %----START------------
   fileID=fopen(strcat(path,'\',prefix,'reconstruction_data.txt'),'w');
   for j=1:3
   fprintf(fileID,'%29s \r\n',strcat('---',num2str(j),...
       '. pattern orientation---'));fprintf(fileID,'%15s\r\n','');
20 fprintf(fileID,'%18s','Orientation angle=');fprintf(fileID,...
       '%7.4f deg\r\n',atand(Ktrans_all(1,1,j)/Ktrans_all(2,1,j)));
   fprintf(fileID,'%15s\r\n','');fprintf(fileID,'%17s\r\n',...
```

```
       '**Peak Position**');fprintf(fileID,'|%7i
    %7i|\r\n',Pixelshift_all(:,:,j)');
 25 fprintf(fileID,'%15s\r\n','');fprintf(fileID,'%17s\r\n',...
       '*****K shift*****');fprintf(fileID,'|%7.4f
    %7.4f|\r\n',Ktrans_all(:,:,j)');
    fprintf(fileID,'%15s\r\n','');fprintf(fileID,'%30s\r\n',...
       '***K norm and initial phase***');
 30 fprintf(fileID,'%2s','K=');fprintf(fileID,'%7.4f\r\n',K_all(j));
    fprintf(fileID,'%2s','phi=');fprintf(fileID,'%7.4f rad\r\n',phi_all(j));
    fprintf(fileID,'%15s\r\n','');fprintf(fileID,'%15s\r\n',...
       '*****Period******');
    fprintf(fileID,'%7.4f nm\r\n',(2*pi*(Acq(2))/K_all(j)));...
 35    fprintf(fileID,'%15s\r\n','');
    fprintf(fileID,'%30s\r\n','----------------------------');
    end
    fprintf(fileID,'%15s\r\n','');fprintf(fileID,'%15s\r\n',...
       '*****Quality factors******');
 40 fprintf(fileID,'%15s\r\n','');fprintf(fileID,'%15s\r\n',...
       '*****Q-factor Matrix (Q)******');
    fprintf(fileID,'|%7.4f %7.4f|\r\n',Qmat);
    %%%%%%%%%%%%%%%%%%%%%%%%%%%%
    %%%%%---WARNINGS---%%%%%%%%%%
 45 %%%%%%%%%%%%%%%%%%%%%%%%%%%%
    if Qratio<0
    fprintf(fileID,'%21s\r\n','!!!Noise is higher than modulated signal!!!');
    end
    if avgSNR<=4
 50 fprintf(fileID,'%25s\r\n','!!!SNR too low!!!');
    end
    %%%%%%%%%%%%%%%%%%%%%%%%%%%%
    %%%%%---END WARNINGS---%%%%%%
    %%%%%%%%%%%%%%%%%%%%%%%%%%%%
 55 fprintf(fileID,'%4s','<Q>=');fprintf(fileID,'%7.4f\r\n',Qfactor);
    fprintf(fileID,'%4s','SNR=');fprintf(fileID,'|%7.4f %7.4 %7.4f|\r\n',SNR);
    fprintf(fileID,'%6s','<SNR>=');fprintf(fileID,'%7.4f\r\n',avgSNR);
    fprintf(fileID,'%10s','<SNR_SIM>=');fprintf(fileID,'%7.4f\r\n',avgSNR_SIM);
    fprintf(fileID,'%15s\r\n','');fprintf(fileID,'%15s\r\n',...
 60    '*****Acquisition Parameters******');
    fprintf(fileID,'%6s','NA=');fprintf(fileID,'%7.4f \r\n',Acq(1));
    fprintf(fileID,'%6s','Emission=');fprintf(fileID,'%8.4f nm\r\n',Acq(3));
    fprintf(fileID,'%6s','Pixelsize=');fprintf(fileID,'%8.4f nm\r\n',Acq(2));
    fprintf(fileID,'%26s','Estimated resolution gain=');
 65 fprintf(fileID,'%8.4f \r\n',Acq(4));
    fclose(fileID);
    end
```

Bibliography

1. Gerlach, Joseph von. *Mikroskopische Studien aus dem Gebeite der menschlichen Morphologie*. (Erlangen :, 1858).

2. Baeyer, A. Ueber eine neue Klasse von Farbstoffen. *Berichte der Dtsch. Chem. Gesellschaft* **4,** 555–558 (1871).

3. Abbe, E. Beiträge zur Theorie des Mikroskops und der mikroskopischen Wahrnehmung. *Arch. für Mikroskopische Anat.* **9,** 413–418 (1873).

4. Rayleigh, Lord. On the Theory of Optical Images, with special reference to the Microscope. *J. R. Microsc. Soc.* **23,** 474–482 (1903).

5. Ellinger, P. & Hirt, A. Mikroskopische Beobachtungen an lebenden Organen mit Demonstrationen (Intravitalmikroskopie). *Arch. für Exp. Pathol. und Pharmakologie* **147,** 63–63 (1929).

6. Coons, A. H., Creech, H. J. & Jones, R. N. Immunological Properties of an Antibody Containing a Fluorescent Group. *Exp. Biol. Med.* **47,** 200–202 (1941).

7. Bennett, A. H. The Development of the Microscope Objective. *J. Opt. Soc. Am.* **33,** 123 (1943).

8. Coons, A. H., Creech, H. J., Jones, R. N. & Berliner, E. *The journal of immunology : official journal of the American Association of Immunologists.* (Williams & Wilkins, 1950).

9. Maiman, T. H. Stimulated Optical Radiation in Ruby. *Nature* **187,** 493–494 (1960).

10. Ploem, J. S. The use of a vertical illuminator with interchangeable dichroic mirrors for fluorescence microscopy with incidental light. *Z. Wiss. Mikrosk.* **68,** 129–42 (1967).

11. Boyle, W. S. & Smith, G. E. Charge Coupled Semiconductor Devices. *Bell Syst. Tech. J.* **49,** 587–593 (1970).

12. Chalfie, M., Tu, Y., Euskirchen, G., Ward, W. W. & Prasher, D. C. Green fluorescent protein as a marker for gene expression. *Science* **263,** 802–5 (1994).

13. Lubsandorzhiev, B. K. On the history of photomultiplier tube invention. *Nucl. Instruments Methods Phys. Res. Sect. A Accel. Spectrometers, Detect. Assoc. Equip.* **567,** 236–238 (2006).

14. Van Leeuwenhoek, A. *The Selected Works of Antony van Leeuwenhoek Containing His Microscopical Discoveries in Many of the Works of Nature*. (Arno Press, 1977).

15. Hooke, R. Micrographia. *Collection items* (2017). Available at: https://www.bl.uk/collection-items/micrographia-by-robert-hooke-1665.

16. Lichtman, J. W. & Conchello, J.-A. Fluorescence microscopy. *Nat. Methods* **2,**

910–919 (2005).

17. Campagnola, P. J. & Loew, L. M. Second-harmonic imaging microscopy for visualizing biomolecular arrays in cells, tissues and organisms. *Nat. Biotechnol.* **21,** 1356–1360 (2003).

18. Bueno, J. M., Ávila, F. J. & Artal, P. Second Harmonic Generation Microscopy: A Tool for Quantitative Analysis of Tissues. in *Microscopy and Analysis* (InTech, 2016). doi:10.5772/63493

19. Jares-Erijman, E. A. & Jovin, T. M. FRET imaging. *Nat. Biotechnol.* **21,** 1387–1395 (2003).

20. Suhling, K. *et al.* Fluorescence lifetime imaging (FLIM): Basic concepts and some recent developments. *Med. Photonics* **27,** 3–40 (2015).

21. Schneckenburger, H. Total internal reflection fluorescence microscopy: technical innovations and novel applications. *Curr. Opin. Biotechnol.* **16,** 13–18 (2005).

22. Webb, R. H. Confocal optical microscopy. *Reports Prog. Phys.* **59,** 427–471 (1996).

23. Huisken, J., Swoger, J., Del Bene, F., Wittbrodt, J. & Stelzer, E. H. K. Optical sectioning deep inside live embryos by selective plane illumination microscopy. *Science* **305,** 1007–9 (2004).

24. Greger, K., Swoger, J. & Stelzer, E. H. K. Basic building units and properties of a fluorescence single plane illumination microscope. *Rev. Sci. Instrum.* **78,** 23705 (2007).

25. Stelzer, E. H. K. Light-sheet fluorescence microscopy for quantitative biology. *Nat. Methods* **12,** 23–26 (2014).

26. Hell, S. W. & Wichmann, J. Breaking the diffraction resolution limit by stimulated emission: stimulated-emission-depletion fluorescence microscopy. *Opt. Lett.* **19,** 780 (1994).

27. Klar, T. A., Jakobs, S., Dyba, M., Egner, A. & Hell, S. W. Fluorescence microscopy with diffraction resolution barrier broken by stimulated emission. *Proc. Natl. Acad. Sci. U. S. A.* **97,** 8206–10 (2000).

28. Gustafsson, M. G. L., Agard, D. A. & Sedat, J. W. Doubling the lateral resolution of wide-field fluorescence microscopy using structured illumination. in (eds. Conchello, J.-A., Cogswell, C. J., Tescher, A. G. & Wilson, T.) **3919,** 141–150 (International Society for Optics and Photonics, 2000).

29. Gustafsson, M. G. L. *et al.* Three-dimensional resolution doubling in wide-field fluorescence microscopy by structured illumination. *Biophys. J.* **94,** 4957–70 (2008).

30. Betzig, E. *et al.* Imaging intracellular fluorescent proteins at nanometer resolution. *Science* **313,** 1642–5 (2006).

31. Hess, S. T., Girirajan, T. P. K. & Mason, M. D. Ultra-high resolution imaging by fluorescence photoactivation localization microscopy. *Biophys. J.* **91,**

4258–72 (2006).

32. Rust, M. J., Bates, M. & Zhuang, X. Sub-diffraction limit imaging by stochastic optical reconstruction microscopy (STORM). *Nat. Methods* **3,** 793–796 (2006).

33. Van De Linde, S. *et al.* Direct stochastic optical reconstruction microscopy with standard fluorescent probes. *Nat. Protoc.* **6,** 991–1009 (2011).

34. Endesfelder, U. & Heilemann, M. Direct stochastic optical reconstruction microscopy (Dstorm). *Methods Mol. Biol.* **1251,** 263–276 (2014).

35. Gustafsson, M. G. L. Surpassing the lateral resolution limit by a factor of two using structured illumination microscopy. *J. Microsc.* **198,** 82–87 (2000).

36. Chang, B.-J., Perez Meza, V. D. & Stelzer, E. H. K. csiLSFM combines light-sheet fluorescence microscopy and coherent structured illumination for a lateral resolution below 100 nm. *Proc. Natl. Acad. Sci. U. S. A.* **114,** 4869–4874 (2017).

37. Perez, V., Chang, B.-J. & Stelzer, E. H. K. Optimal 2D-SIM reconstruction by two filtering steps with Richardson-Lucy deconvolution. *Sci. Rep.* **6,** 37149 (2016).

38. Wicker, K., Mandula, O., Best, G., Fiolka, R. & Heintzmann, R. Phase optimisation for structured illumination microscopy. *Opt. Express* **21,** 2032–2049 (2013).

39. Demmerle, J. *et al.* Strategic and practical guidelines for successful structured illumination microscopy. *Nat. Protoc.* **12,** 988–1010 (2017).

40. Ryan, D. P. *et al.* Automatic and adaptive heterogeneous refractive index compensation for light-sheet microscopy. *Nat. Commun.* **8,** 612 (2017).

41. Silvestri, L., Sacconi, L. & Pavone, F. S. Light sheet microscopy of cleared mouse brains: aberrations effects caused by refractive index mismatch. *Neurophotonics* **8804,** 880405 (2013).

42. Born, M. & Wolf, E. *Principles of optics : electromagnetic theory of propagation, interference and diffraction of light*. (Pergamon Press, 1980).

43. Novotny, L. & Hecht, B. *Principles of nano-optics*. (Cambridge University Press, 2012).

44. Zhang, B., Zerubia, J. & Olivo-Marin, J.-C. Gaussian approximations of fluorescence microscope point-spread function models. *Appl. Opt.* **46,** 1819 (2007).

45. Beck, M., Aschwanden, M. & Stemmer, a. Sub-100-nanometre resolution in total internal reflection fluorescence microscopy. *Nanotechnology* **232,** 99–105 (2008).

46. Chen, B.-C. *et al.* Lattice light-sheet microscopy: imaging molecules to embryos at high spatiotemporal resolution. *Science* **346,** 1257998 (2014).

47. Stelzer, E. H. K. Light sheet fluorescence microscopy for quantitative biology. *Nat. Methods* **12,** 23–26 (2015).

48. Martin-Fernandez, M. L., Tynan, C. J. & Webb, S. E. D. A 'pocket guide' to total internal reflection fluorescence. *J. Microsc.* **252,** 16–22 (2013).

49. Yaroslavsky, L. P. & Caulfield, H. J. Deconvolution of multiple images of the same object. *Appl. Opt.* **33,** 2157 (1994).

50. Müller, M., Mönkemöller, V., Hennig, S., Hübner, W. & Huser, T. Open-source image reconstruction of super-resolution structured illumination microscopy data in ImageJ. *Nat. Commun.* **7,** 10980 (2016).

51. Brakenhoff, G. J., Blom, P. & Barends, P. Confocal scanning light microscopy with high aperture immersion lenses. *J. Microsc.* **117,** 219–232 (1979).

52. ThermoFisher. Table 1 Properties of Alexa Fluor Dyes. *https://www.thermofisher.com/de/de/home/brands/molecular-probes/key-molecular-probes-products/alexa-fluor/alexa-fluor-dyes-across-the-spectrum.html*

53. Ball, G. *et al.* SIMcheck: a Toolbox for Successful Super-resolution Structured Illumination Microscopy. *Sci. Rep.* **5,** 15915 (2015).

54. Matthews, C. & Cordeliéres, F. P. MetroloJ: an ImageJ plugin to help monitor microscopes' health. *Image J User Dev. Conf. 2010 Proc.* (2010).

55. Fiolka, R., Beck, M. & Stemmer, A. Structured illumination in total internal reflection fluorescence microscopy using a spatial light modulator. *Opt. Lett.* **33,** 1629–31 (2008).

56. Chung, E., Kim, D. & So, P. T. C. Extended resolution wide-field optical imaging: objective-launched standing-wave total internal reflection fluorescence microscopy. *Opt. Lett.* **31,** 945–947 (2006).

57. Planchon, T. A. *et al.* Rapid three-dimensional isotropic imaging of living cells using Bessel beam plane illumination. *Nat. Methods* **8,** 417–423 (2011).

58. Gao, L., Shao, L., Chen, B.-C. & Betzig, E. 3D live fluorescence imaging of cellular dynamics using Bessel beam plane illumination microscopy. *Nat. Protoc.* **9,** 1083–1101 (2014).

59. Manton, J. D. & Rees, E. J. triSPIM: light sheet microscopy with isotropic super-resolution. *Opt. Lett.* **41,** 4170 (2016).

60. http://fairsim.github.io/.

61. Richardson, W. H. Bayesian-Based Iterative Method of Image Restoration. *J. Opt. Soc. Am.* **62,** 55 (1972).

62. Lucy, L. B. An iterative technique for the rectification of observed distributions. *Astron. J.* **79,** 745 (1974).

63. Sage, D. *et al.* DeconvolutionLab2: An open-source software for deconvolution microscopy. *Methods* **115,** 28–41 (2017).

64. Preibisch, S. *et al.* Efficient Bayesian-based multiview deconvolution. *Nat. Methods* **11,** 645–648 (2014).

65. Mudry, E. *et al.* Structured illumination microscopy using unknown speckle patterns. *Nat. Photonics* **6,** 312–315 (2012).

Bibliography

66.   Ayuk, R. *et al.* Structured illumination fluorescence microscopy with distorted excitations using a filtered blind-SIM algorithm. *Opt. Lett.* **38,** 4723–6 (2013).

67.   Jost, A. *et al.* Optical Sectioning and High Resolution in Single-Slice Structured Illumination Microscopy by Thick Slice Blind-SIM Reconstruction. *PLoS One* **10,** e0132174 (2015).

68.   Komis, G. *et al.* Superresolution live imaging of plant cells using structured illumination microscopy. *Nat. Protoc.* **10,** 1248–1263 (2015).

69.   O'Holleran, K. & Shaw, M. Optimized approaches for optical sectioning and resolution enhancement in 2D structured illumination microscopy. *Biomed. Opt. Express* **5,** 2580 (2014).

70.   Shaw, M., Zajiczek, L. & O'Holleran, K. High speed structured illumination microscopy in optically thick samples. *Methods* **88,** 11–19 (2015).

71.   Van Kempen, G. M. P., Van Vliet, L. J., Verveer, P. J. & Van der voort, H. T. M. A quantitative comparison of image restoration methods for confocal microscopy. *J. Microsc.* **185,** 354–365 (1997).

72.   Chakrova, N., Rieger, B. & Stallinga, S. Deconvolution methods for structured illumination microscopy. *J. Opt. Soc. Am. A* **33,** B12 (2016).

73.   Stelzer. Contrast, resolution, pixelation, dynamic range and signal-to-noise ratio: fundamental limits to resolution in fluorescence light microscopy. *J. Microsc.* **189,** 15–24 (1998).

74.   Papoulis, A. Probability, Random Variables And Stochastic Processes. *Book* 678 (1991). doi:10.2307/1266379

75.   Mandula, O. *et al.* Line scan - structured illumination microscopy super-resolution imaging in thick fluorescent samples. *Opt. Express* **20,** 24167–24174 (2012).

76.   Li, D. *et al.* Extended-resolution structured illumination imaging of endocytic and cytoskeletal dynamics. *Science (80-.).* **349,** (2015).

77.   Somekh, M. G., Hsu, K. & Pitter, M. C. Resolution in structured illumination microscopy: a probabilistic approach. *J. Opt. Soc. Am. A. Opt. Image Sci. Vis.* **25,** 1319–1329 (2008).

78.   Mendlovic, D., Shabtay, G., Zalevsky, Z. & Lipson, S. G. The optimal system for sub-wavelength point source localization. *Opt. Commun.* **198,** 311–315 (2001).

79.   Lipson, S. G. Why is super-resolution so inefficient? in *Micron* **34,** 309–312 (2003).

80.   Young, L. J., Ströhl, F. & Kaminski, C. F. A Guide to Structured Illumination TIRF Microscopy at High Speed with Multiple Colors. *J. Vis. Exp.* (2016). doi:10.3791/53988

81.   Kraus, F. *et al.* Quantitative 3D structured illumination microscopy of nuclear structures. *Nat. Protoc.* **12,** 1011–1028 (2017).

82.   Demmerle, J., Wegel, E., Schermelleh, L. & Dobbie, I. M. Assessing

resolution in super-resolution imaging. *Methods* **88,** 3–10 (2015).

83.   Keller, P. J. & Stelzer, E. H. K. Digital scanned laser light sheet fluorescence microscopy. *Cold Spring Harb. Protoc.* **2010,** pdb.top78 (2010).

84.   Staudt, T., Lang, M. C., Medda, R., Engelhardt, J. & Hell, S. W. 2,2′-Thiodiethanol: A new water soluble mounting medium for high resolution optical microscopy. *Microsc. Res. Tech.* **70,** 1–9 (2007).

85.   Dodt, H.-U. *et al.* Ultramicroscopy: three-dimensional visualization of neuronal networks in the whole mouse brain. *Nat. Methods* **4,** 331–336 (2007).

86.   Azaripour, A. *et al.* A survey of clearing techniques for 3D imaging of tissues with special reference to connective tissue. *Prog. Histochem. Cytochem.* **51,** 9–23 (2016).

Curriculum Vitae

█████ PERSONAL INFORMATION

Name:	Victor Didier, Perez Meza
Address:	Niedwiesenstraße 54
	Frankfurt am Main 60431
	Germany
Mobile:	(+49)17643227082
E-mail:	vdpm85@hotmail.com
Nationality:	Mexican

█████ EDUCATION

2014-2018 **Ph.D.** Goethe-Universität, Frankfurt am Main, Germany
(Supervisor: Prof. Dr. Ernst H.-K. Stelzer)

Thesis: *Enhancement of resolution gain and optimization of reconstruction process in structured illumination microscopy*

2010-2012 **M.Sc. (Nanobiophysics)**, Technische Universität Dresden, Dresden, Germany

Thesis: *Simulations of backward and forward second harmonic generation emission of collagen fibers to estimate their packing density*

2005-2010 **B.Sc. (Physics)**, National Autonomous University of Mexico, Mexico city

Thesis: *Photophysical characterization of hybrid compounds (Eu2O3:Polyphenyacetylene) with different spectroscopy methods*

█████ WORK EXPERIENCE

2014-2018 **Research assistant** (Doctorate), Buchmann Institute for Molecular Life sciences, Frankfurt am Main, Germany

2012-2014 **Research assistant,** Center for Regenerative Therapies, Dresden, Germany

2011-2012 **Student assistant**, Leibnitz Institut for Solid State and Materials Research, Dresden, Germany

TEACHING EXPERIENCE

2018   **Light Microscopy (Lecture)**, Physical biology of cells and interactions Masters course Goethe-Universität, Frankfurt am Main, Germany

2014-2017   **Supervision of Master's students in practical courses,** Buchmann Institute for Molecular Life sciences, Frankfurt am Main, Germany

PUBLICATIONS AND CONFERENCES

- csiLSFM combines light-sheet fluorescence microscopy and coherent structured illumination for a lateral resolution below 100 nm. *PNAS* 114 (2017), 4869-4874. Bo-Jui Chang, <u>Victor Didier Perez Meza</u> and Ernst H. K. Stelzer.

- Optimal 2D-SIM reconstruction by two filtering steps with Richardson-Lucy deconvolution.. *Sci Rep.* 6 (2016), 37149. <u>Victor Didier Perez Meza</u>, Bo-Jui Chang, and Ernst H. K. Stelzer.

- A Service-Oriented Architecture for Body Area NanoNetworks with Neuron-based Molecular Communication. *Mobile Networks and Applications* 19 (2014), 707–717. Junichi Suzuki, Sasitharan Balasubramaniam, Sophie Pautot, <u>Victor Didier Perez Meza</u> and Yevgeni Koucheryavy.

- **Oral presentation** 2nd Light Sheet Fluorescence Microscopy International Conference 2015, Genoa, Italy. csiLSFM-coherent structured illumination LightSheet-based Fluorescence Microscopy

- **Poster presentation** in Focus on Microscopy 2015, Göttingen, Germany. Automated optimization for 2D-SIM image reconstruction.

Erklärung

Ich erkläre hiermit, dass ich mich bisher keiner Doktorprüfung im Mathematisch-Natur-wissenschaftlichen Bereich unterzogen habe.

Frankfurt am Main, den _____   _____

(Unterschrift)

Eidesstattliche Versicherung

Ich erkläre hiermit an Eides Statt, dass ich die vorgelegte Dissertation über "Structured illumination microscopy: enhancement of resolution gain, reconstruction process and quantitative assessment of images" selbständig angefertigt und mich anderer Hilfsmittel als der in ihr angegebenen nicht bedient habe, insbesondere, dass alle Entlehnungen aus anderen Schriften mit Angabe der betreffenden Schrift gekennzeichnet sind. Ich versichere, die Grundsätze der guten wissenschaftlichen Praxis beachtet, und nicht die Hilfe einer kommerziellen Promotionsvermittlung in Anspruch genommen zu haben.

Frankfurt am Main, den _____   _____

(Unterschrift)